Modeling and Applications of Highly-Scaled Gravure Printing

Rungrot Kitsomboonloha

Electrical Engineering and Computer Sciences
University of California at Berkeley

Technical Report No. UCB/EECS-2015-213
http://www.eecs.berkeley.edu/Pubs/TechRpts/2015/EECS-2015-213.html

December 1, 2015

Modeling and Applications of Highly-Scaled Gravure Printing

by

Rungrot Kitsomboonloha

A dissertation submitted in partial satisfaction of the

requirements for the degree of

Doctor of Philosophy

in

Engineering – Electrical Engineering and Computer Sciences

in the

Graduate Division

of the

University of California, Berkeley

Committee in charge:

Professor Vivek Subramanian, Chair
Associate Professor Ana Claudia Arias
Professor S.J.S. Morris

Fall 2014

Abstract

Modeling and Applications of Highly-Scaled Gravure Printing

by

Rungrot Kitsomboonloha

Doctor of Philosophy in Engineering – Electrical Engineering and Computer Sciences

University of California, Berkeley

Professor Vivek Subramanian, Chair

Pattern printing techniques have advanced rapidly in the last decade, driven by their potential applications in printed electronics. Several printing techniques have realized printed features ≤10 μm, but unfortunately they suffer from disadvantages that prevent their deployment in real applications; in particular, process throughput is a significant concern. Direct gravure printing delivers high throughput and has a proven history of being manufacturing worthy. Unfortunately, it suffers from scalability challenges due to limitations in roll manufacturing and lack of understanding of the relevant printing mechanisms. Gravure printing relies on individual processes namely filling, wiping, transferring and spreading to achieve high quality printing. As gravure printed features are scaled, the associated complexities are increased, and a detailed study of the various processes involved is needed.

In this thesis, the various gravure-related fluidic mechanisms are studied using a novel inverse direct gravure printer. The underlying mechanisms of gravure printing are presented. A simple model of gravure printing is proposed. This model demonstrates that individual fluidic processes can be studied separately and a comprehensive understanding of the wiping process in gravure printing is analyzed carefully due to the importance of this process in producing high-fidelity patterns. We report two critical wiping mechanisms that generate drag-out and lubrication residues, which are fundamental scaling limitations for highly-scaled gravure printing. Third, the filling process is investigated, leaded to explanations of air entrapment in gravure cells. In addition, we provide designs and operation conditions for the ultimate reduction of the residues, leading significant scaling of printed features. Printed lines as small as 2 μm are realized at printing speeds as high as ~1 m/s, attesting to the potential of highly-scaled gravure printing.

In addition to comprehensive printing mechanism studies, we demonstrate a fabrication process for a high-resolution roll based on advanced microfabrication techniques. The fabrication process incorporates the design guidelines developed previously to deliver the optimized cell geometry and pattern arrangement. Furthermore, electrically functional high-resolution lines are integrated in a fabrication process for fully printed high performance thin film transistors (TFTs). Highly-scaled TFTs demonstrated with channel lengths as small as 3 μm, leading to devices with transition frequency above 1 MHz; this represents a significant advancement over the state of the art.

Table of Contents

Acknowledgements

I would like to express my immense gratitude to Professor Vivek Subramanian who inspired me to work on printed electronics, a multidisciplinary field that enabled me to broaden my technical skills and become a competent researcher and engineer. He not only improved my research vision, but also mentored me through hard times in both my academic and personal life. Therefore, I thank him very much and am glad that I have had the opportunity to work closely with him.

I deeply thank Professor S.J.S Morris who guided me through the complicated field of micro-fluidics and interfacial phenomena and showed me how convoluted mathematical equations could be understood intuitively most of the time. His advice has greatly benefited my research. I also really appreciate Professor Xiaoying Rong who provided me with invaluable experimental data and enjoyable discussions regarding drag-out effects.

I would like to acknowledge Alejandro De la Fuente Vornbrock, who worked intensely on direct-gravure printing and printed thin film transistors. He mentored me and directed my interest toward gravure printing since the early years of my PhD program. He and Huai-Yuan Tseng also made my life very cheerful and helped me quickly adjust to the fast-paced research environment at Berkeley.

My special thanks are also extended to Hongki Kang, who worked with me in developing high-performance thin film transistors, which enabled me to rapidly establish a successful process. I would also like to offer my special thanks to Gerd Grau, who helped me realize a fabrication process for high-resolution rolls and gave me thoughtful discussions throughout projects. In addition, I am particularly grateful for the knowledge contributed by Jialiang (Artos) Cen in studying the filling process. He not only carefully executed the study, but also helped me polish my mentoring skills. I also wish to acknowledge Umut Ceyhan and William Scheideler for many useful discussions during a study of lubrication films in gravure printing. Likewise, I appreciate the assistance provided by Geoffroy Mouret in an investigation of the effects of cell geometry. Therefore, once again, I would like to thank our gravure printing team. Without them, this dissertation would have taken much longer to complete. The many discussions we had refined my thoughts and helped me understand problems more clearly. In addition, they give me the courage and creativity required to tackle these research challenges.

I would like to thank all the members of the Organic electronics group. We have shared many good times over summer football games and BBQ parties. It was a pleasure to be a part of this group. The dynamic of this group is always encouraging and makes hard problems more pleasant. I would like to specially thank Nishita Deka for proofreading this manuscript.

I would like to express my gratitude to the Lam Research Fellowship. The fellowship is an essential part of my research accomplishments. Finally, I appreciate the help of Daetwyler Corporation for supplying doctor blades and Dupont Teijin for supplying substrates used in this work.

I would like to acknowledge my parents for giving me a wonderful life and supporting me. They always give me strength and wisdom throughout my journey. And I would like to extend my special thanks to my wife and son, who rejuvenate my mental and physical. Because of her, I am able to fully devote my time to research and overcoming its challenges.

Chapter 1 Introduction

Recently, researchers and scientists have become interested in using printing technologies as manufacturing methods using solution processable materials. This promises a significant cost reduction due to simpler fabrication processes and lower capital costs. In addition to the process advantages, printing technologies allow a unique way to fabricate certain applications that are not economically feasible by conventional microfabrication techniques, such as wall-size sensor arrays. The Organic and Printed Electronics Association (OE-A) proposed a roadmap for organic and printed electronics as shown in Figure 1.1. The roadmap promises various applications that can improve our daily life in all aspects. According to the roadmap, researchers have demonstrated such applications as e-skin or smart bandages that can monitor body temperature, pressure, and movement on ultra-thin substrates [1], [2], which can be used for both health or robotics applications; flexible displays for mobile devices and large area applications [3] that allow users to fold the displays into a smaller form, which is more convenient for transportation and storage; and ultra-low-cost RFID that is inexpensive to be attached on all consumer products [4]. All these demonstrations are possible due to rapid materials development in recent years. Nowadays, high performance electronic inks such as metal nanoparticle, high-k dielectric suspension, and organic semiconductor inks are widely available.

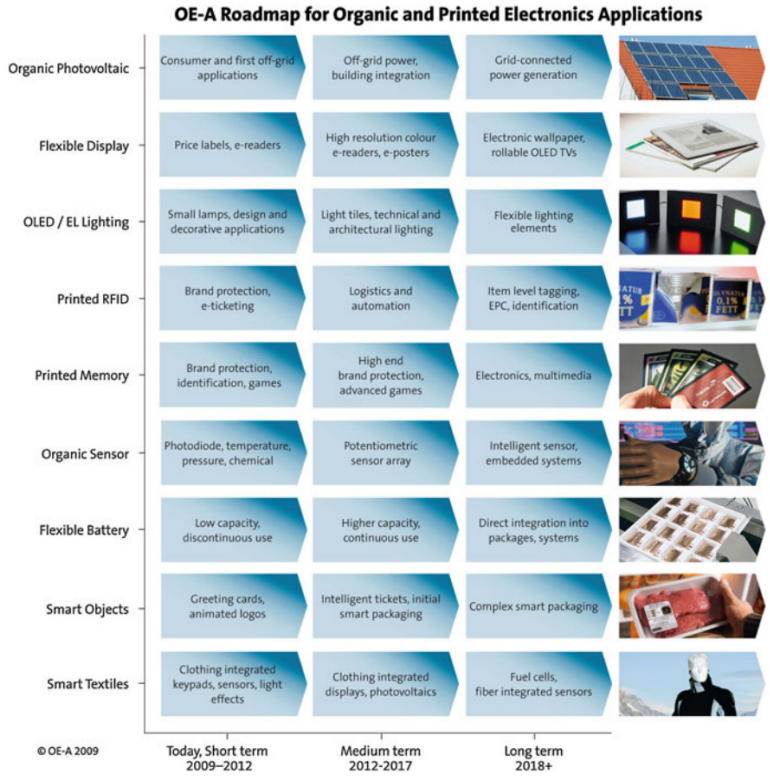

Figure 1.1 OE-A Roadmap for organic and printed electronics applications [5]

However, manufacturing methods are still under development compared to application demonstration and material developments. Researchers are confined to low-throughput methods due to the lack of availability and knowledge of advanced printing technologies for printed electronics. Furthermore, since electronic devices require precise geometry, patterning techniques are one of key technological areas for fabricating high performance electronics systems. Therefore, this thesis is devoted to advancing a patterning technique for printed electronics by using a high-speed roll-to-roll printing technique.

1.1 High-speed roll-to-roll printing

Thank to high-speed roll-to-roll printing, our daily lives have been improved substantially for several centuries. There are many products used in our lives that are printed by these printing techniques, such as magazines, catalogs, newspapers, packages, etc. Because of extremely high throughput, low material usage, and low capital cost, these techniques are the best choice for mass production. There are multiple high-speed roll-to-roll printing techniques used today. Each one has its own advantages due to its configuration and the way by which it forms patterns. Figure 1.2 shows four main high speed printing techniques that are used in industry. Flexography, shown in Figure 1.2a, consists of a fountain, anilox, pattern and impression roll. Ink is picked up by a fountain roll and metered by an anilox roll. Then the pattern roll selectively picks up ink only on relief patterns and transfers them onto substrates supported by an impression roll. The relief patterns are typically made of rubber defined by lithography and wet etching. Because of the elasticity of rubber and the finite size of anilox cells, flexography is limited in terms of scaling of feature sizes. However, the elasticity makes flexography compatible with rigid substrates, like metal, glass and silicon wafers. Another printing technique that is similar to flexography is letterpress, which uses a metal relief instead of rubber. The letterpress is normally configured as a roll-to-roll printer by using curved metal plates. Details on modern letterpress can be found in [6]. Offset lithography printing shown in Figure 1.2b uses *wettability* (see section 1.4.3) to form liquid patterns, instead of relief patterns as in flexography. A lithographic plate contains hydrophobic and hydrophilic regions. By inking the patterns with water and immiscible ink, liquids separate and form patterns during the printing. Then the liquid pattern is transferred to a blanket roll and substrate, respectively. The advantage of offset lithography is that patterns are fabricated on a planar surface to form hydrophobic and hydrophilic regions. This makes offset lithography patterning much cheaper than flexography and gravure printing. Therefore, offset lithography is normally used for applications in which patterns are frequently changed, like printing newspapers. However, the printer is more complicated and ink optimization is more challenging, involving two phase flows of water and immiscible ink. The usage of water also potentially contaminates some electronic inks and degrades material performance. Direct gravure shown in Figure 1.2c is much simpler. It consists of an engraved roll, doctor blade, impression roll and ink dispensing unit. The pattern is formed by using recessed cells below a roll surface, called engraved cells. The cells are filled as they pass an ink stream. Then excess ink is removed by a doctor blade and ink contained in the cells is transferred to substrates as it makes a contact under roll pressure between a pattern roll and impression roll. Offset direct gravure adds an offset roll as shown in Figure 1.2d to relax a

mechanical constraint when printing on rigid substrates. However, this reduces the pattern fidelity due to a deformation of offset roll. The offset process also reduces materials transferred to substrates because of the non-ideal transfer processes. The "offset" term refers to the presence of an intermediate roll between a pattern roll and substrate (Figure 1.2b and d). In this work, we will focus on direct gravure printing, because of its high pattern fidelity and simplicity. Direct gravure is also known as rotogravure and gravure, and it will be referred to as gravure in this thesis.

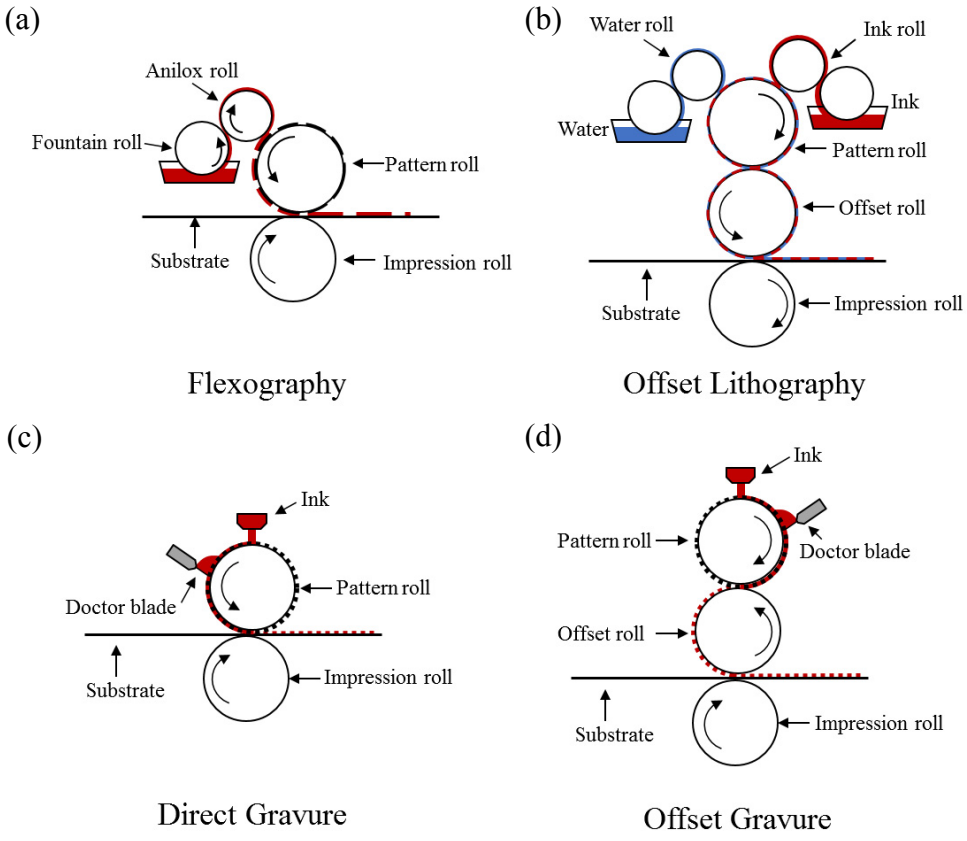

Figure 1.2 high-speed roll-to-roll printing techniques used in printing industrials: (a) flexography, (b) offset lithography, (c) direct gravure, and (d) offset direct gravure

1.2 History of gravure printing

At the same time as Gutenberg's letterpress was invented, gravure printing was also invented as a better way to produce pictorial media. The first gravure printing was done in 1446 [7] using an intaglio printing plate. The word *intaglio* is Italian, meaning "engraved" or "cut in." Intaglio plates use grooves on copper plates to form images and typically must be engraved manually. Because this technique can produce both printed patterns and embossed relief features on paper, it is still used today in security printing like bank notes and stamps. While letterpress became the preferred method for printing text, gravure is the preferred method for printing artwork due to its

superior quality. Even though gravure printing using intaglio was very popular at that time, it was very time consuming and expensive to make intaglio plates and was unable to produce gray-scale coloring. In the early 1500's, the invention of chemical etching and development of photoresists advanced the way gravure patterns are made. This roll fabrication method then became a major method of gravure print roll fabrication due to its reliability and throughput. In the 17th century, Ludwid von Siegen invented the half tone technique, which made it possible to reproduce shades in gravure from a copper plate engraving by using small dots, instead of grooves. This allowed gravure to reproduce painting and fine drawings. In 1968, electromechanical cylinder engraving became available, followed by digital electronic engraving in 1983, which is widely used today. Modern day digital engravings are formed using electrochemical, indirect laser, and direct laser engraving. These engraving technologies can produce gravure cells in range of 10 to 100 μm.

1.3 Motivation of this study

In printed electronics, high-fidelity fine features are essential, because the performance and variability of devices depends on their geometries. Pattern printing techniques have advanced rapidly in the last decade to deliver smaller critical dimensions. Several printing techniques have been used to produce printed features ≤ 10μm for printed electronics. For example, Sekitani used electrohydrodynamic (EHD) printing of source/drain electrodes for organic transistors with a line width of 2 μm and channel length of 1 μm [8]. Although the printing resolution is outstanding, it requires up to 10 passes to print conductive lines and it is difficult to increase printing throughput by using multiple EHD nozzles and high printing speeds due to electrostatic interference and limits on drop placement accuracy. These challenges lead to extremely low printing throughput. Tseng proposed a hybrid printing (print-and-drag) technique that combines ink-jet and micro-dip-pen printing [9]. This technique increases the resolution of inkjet printing from 20 μm to 5 μm by mechanically dragging ink from a small ink reservoir printed by inkjet printing on a substrate. Due to the limited mass loading of inkjet inks, it is challenging to obtain conductive lines below 5 μm. Additionally, integration of multiple mechanical tips is painstaking. Soft lithography, a technique that use elastic stamps, molds, and conformable photomasks for patterning into the nanometer regime, has also been used to demonstrated fine features [10]. This technique relies on conventional subtractive microfabrication and is difficult to integrate with roll-to-roll printing. Anh demonstrated high speed roll-to-roll nanoimprint lithography on plastic substrates [11]. The maximum printing speed was ~0.02 m/s, limited by the curing time of the resist material. This technique can achieve line widths as small as 0.07 μm. However, it is a subtractive process and can typically only produce lines for a roll-to-roll process, among other limited patterns. Jain demonstrated roll-to-roll projection lithography that achieved a resolution of 10 μm, but it is also a subtractive process and can only print at a maximum speed of 0.03 m/s due to the limitations of substrate deformation and of the projection system [12]. In contrast to focusing on realizing small line widths, researchers also demonstrated electronic devices by high speed printing techniques. Deganelle reported printed conductive grids using roll-to-roll flexography. The smallest line width was 75 μm at speed of 0.083 m/s [13]. The line width was limited by the squeezing of ink between a relief and substrate and relief deformation. Erika

demonstrated gravure printing of conductive inks on glass substrates at the speed of 1.27 m/s, even though the smallest line width was 75 μm [14]. Pudas used offset gravure to print conductive lines using polymer ink. The smallest line width was 75 μm at the speed of ~0.01 m/s (wiping, pick-up and lay-down speeds were optimized separately) [15]. Frederik used cylinder screen printing at 0.02 m/s to create millimeter scale features for fabrication of solar cell modules [16]. In short, these printing techniques suffer from several disadvantages, impeding their widespread adoption; 1) to achieve high placement accuracy, the printing speed and/or throughput is typically reduced; 2) it is difficult to operate with adequate control and uniformity over large area substrates; 3) due to the need for low viscosity inks, the pattern fidelity is reduced by spreading and dewetting after printing; 4) material loading is limited by the maximum ink viscosity, reducing process throughput, particularly for thicker structures. Reviews on printing techniques for printed electronics can be found on [17]–[21].

According to the literature, a technology barrier can be located as shown in Figure 1.3. This barrier shows that high resolution features must be printed at very low printing speeds or throughput and high speed roll-to-roll printing (section 1.1) can only print large features. This barrier indicates that current technologies and researches cannot satisfy the requirements of high performance printed electronics. It is important to overcome this barrier in order to commercialize printed electronics. In the high-speed printing group, which includes flexography, offset lithography, gravure and gravure offset, gravure printing stands out as the best candidate for high-resolution, high-speed printing. Recently, gravure printing has been used to fabricate various types of electronic devices [14], [22]–[24]. While the high throughput of gravure is well established, the feature scalability of gravure printing is still in question. Several groups have demonstrated gravure printed features larger than 10μm[25]–[27], but to-date, there are no reports of scaling below this regime, down to the 1μm range. In order to push the frontier of patterning technologies for printed electronics, it is worthy to investigate the potential of gravure printing in depth.

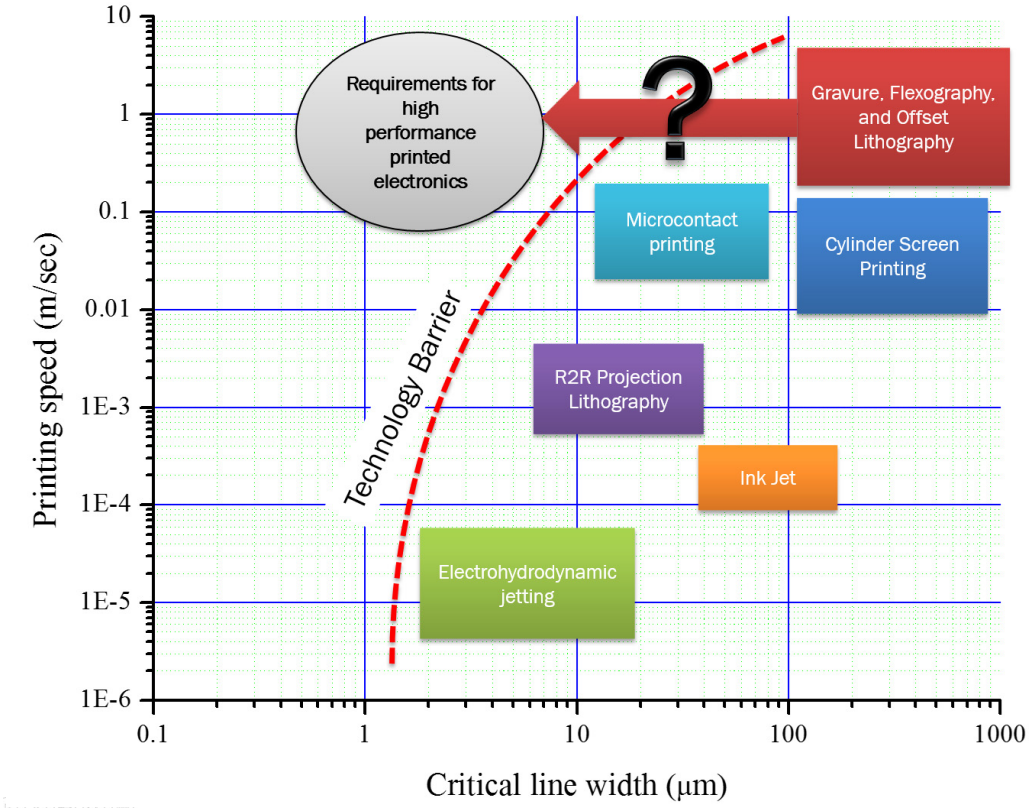

Figure 1.3 A technology barrier of pattern printing technologies and requirements for high-performance printed electronics.

1.4 Basic fluid mechanics for printing

Before discussing the physics of gravure printing later in this thesis, it is important to review basic fluid mechanics that relates to the printing process. In this section, basic concepts of viscosity, surface tension and wettability will be reviewed, since they are key to understanding most printing processes.

1.4.1 Viscosity

The concept of viscosity was first introduced by Newton in the "*Principia"* published in 1687. The basic concept of viscosity can be understood easily by considering a simple model of liquid layers as shown in Figure 1.4. The top plate is movable and bottom plate is stationary with area A. The top movable plate is separated from the bottom stationary plate by a distance x. When the top plate is subjected to a force F acting in a direction tangential to the plate, the top movable plate will move at velocity v relative to the bottom stationary plate. The intermediate plates move with intermediate velocity. Therefore, there will be a gradient of velocity from top to bottom. This velocity gradient is referred as shear rate $\dot{\gamma}$ and has a unit of s^{-1}. And shear stress σ is defined as F/A, i.e. a force per unit area acting on liquid. Shear stress has a unit of N/m^2 or Pa. The viscosity is defined as the relationship of the shear stress σ to the velocity gradient, or shear rate $\dot{\gamma}$, through the equation [28]:

Equation 1.1 $$\sigma = \eta\dot{\gamma}$$

Where η is the viscosity. The physical meaning of viscosity is the resistance of liquid to flow. This is analogous to Ohm's law, which states that voltage is related to current and resistance is defined as a proportionality constant between current (shear rate) and voltage (shear stress). Any fluid that behaves according to this equation, in which η is a constant, is called a Newtonian fluid. Newtonian fluids are water, glycerol, pure organic solvents, etc. However, once viscometers became available, scientists and engineers noticed that most fluids behave differently from Equation 1.1. Characterizations of viscosity then become much more complicated and are typically referred to the field of rheology, which means the study of the deformation and flow of matter. These outlier fluids are called non-Newtonian.

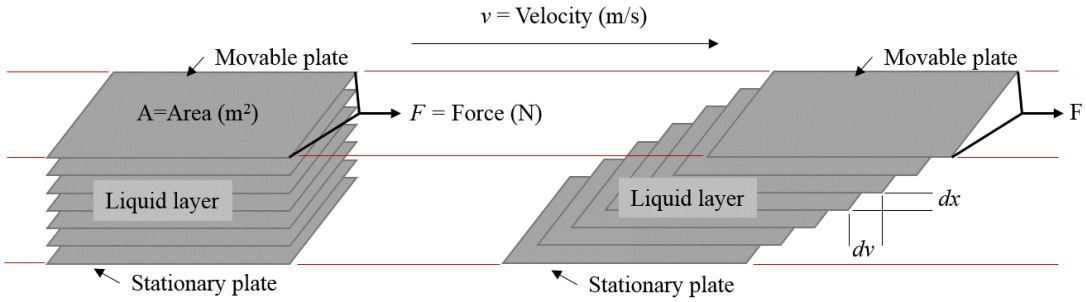

Figure 1.4 A simple model of liquid layers for introducing the concept of viscosity, after [29]

Most inks in high speed printing are non-Newtonian, in which η is a function of the shear rate. In the literature the function $\eta(\dot{\gamma})$ is called shear viscosity, apparent viscosity, the shear-dependent viscosity or simply viscosity. There are several types of behaviors that are classified as non-Newtonian as shown in Figure 1.5a. The associated viscosity of each type is available in Figure 1.5b. First, the *shear thinning* effect is where the required shear stress decreases as the shear rate increases. This means that the viscosity reduces as shear rate increases. This behavior is widely observed in dispersions, emulations and polymer solutions. The shear thinning effect results from breaking a network of polymer entanglement, agglomeration of particles, or hydroxyl bonding in sol-gel solution. Second is the *shear thickening* effect, in which the viscosity rises with the shear rates. This effect is rare compared to shear thinning effect. A popular example of shear thickening is cornstarch and water mixtures. Both shear thinning and thickening originate from the change in microstructures of mixtures. In the case of *Bingham plastics*, the fluid behaves like a solid under low shear stress and will not flow until a critical yield stress is exceeded. But if the shear stress is above the yield stress, the fluid behaves as Newtonian.

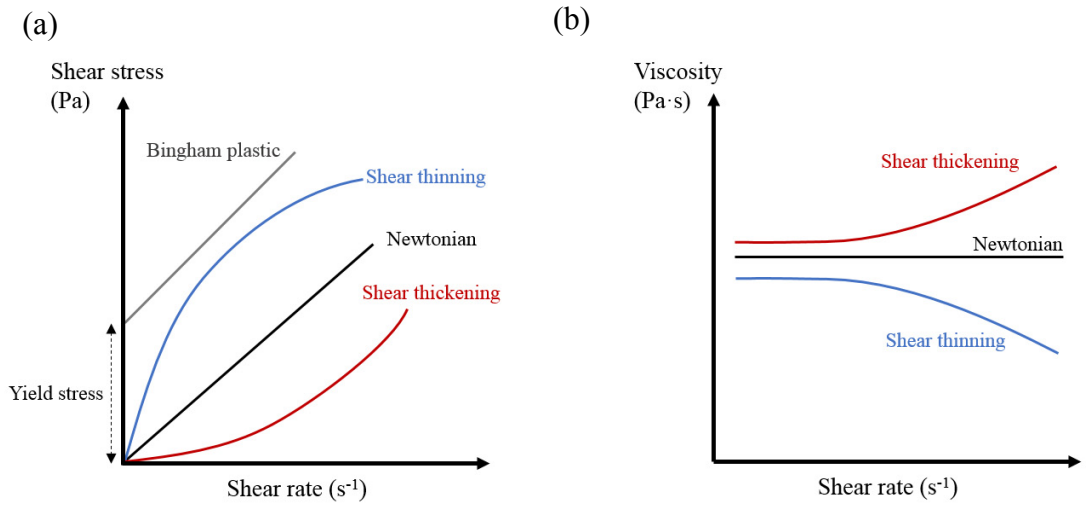

Figure 1.5 (a) Relationships of shear stress and shear rate and (b) viscosity as a function of shear rate of different fluid types.

Beside the dependence on the shear rates, the viscosity can be time dependent as well. For example, the apparent viscosity can reduce under constant shear stress or shear rate and slowly recover after the shear stress or shear rate is removed. This effect is called *thixotropy*. Because flows in printing processes depend on the apparent viscosity, understanding rheological properties of inks is very important for controlling printing processes. Since viscosity can greatly vary with shear rate, it is worthy to know the approximate range of shear rates for typical printing processes as shown in Table 1.1. In high speed printing, typical shear rates are higher than 10^4 s^{-1}. However, the leveling and spreading after printing involve much lower shear rates. Therefore, a complete understanding of the printing process requires a wide range of viscosity characterization.

In addition to the shear rates and time, the viscosity also depends on the temperature and pressure. Most of the Newtonian fluids show an Arrhenius relationship with temperature, i.e. the viscosity exponentially decreases as temperature increases. Under high pressure, like 1GPa, the viscosity exponentially increases with pressure. This pressure-viscosity effect is normally observed in lubrication films of heavily loaded bearings [30].

Table 1.1 Typical shear rates of processes in printing, after [28], [29]

	Shear rate (s^{-1})									
Operation	10^{-2}	10^{-1}	10^{0}	10^{1}	10^{2}	10^{3}	10^{4}	10^{5}	10^{6}	10^{7}
Spreading	■	■								
Leveling	■	■								
Dipping				■						
Flow coating				■						
Mixing				■	■					
Dispersion						■	■	■		

Spraying										
Roller coating										
Brushing										
High speed coating										
Lubrication										

The viscosity can be measured in two ways: 1) control rotating speed (shear rate) and measure the required torque (shear stress): 2) control torque (shear stress) and measure the shear rate. An instrument designed to measure viscosity is called a 'viscometer' and is a subset of a 'rheometer,' which can measure other parameters such as yield stress, and viscoelastic and time dependent behaviors. There are two main arrangements of rheometers: rotational and tube systems as shown in Figure 1.6 [31]. The tube types are capillary and pipe rheometer. The advantages of tube rheometers is that they can measure the viscosity at very high shear rates and they have simpler components. The rotational rheometers consist of one movable and one stationary piece. These include parallel plate, cone and plate, concentric cylinder and mixer rheometers. The rotational rheometers can measure viscosity at very wide ranges of shear rates. In this work, cone and plate rheometers were used to characterize inks. The principle of cone and plate rheometers is based on a simple shearing flow, called Couette flow. It is worth deriving the viscosity equation for cone and plate rheometers since it is the most popular instrument for rheological characterizations.

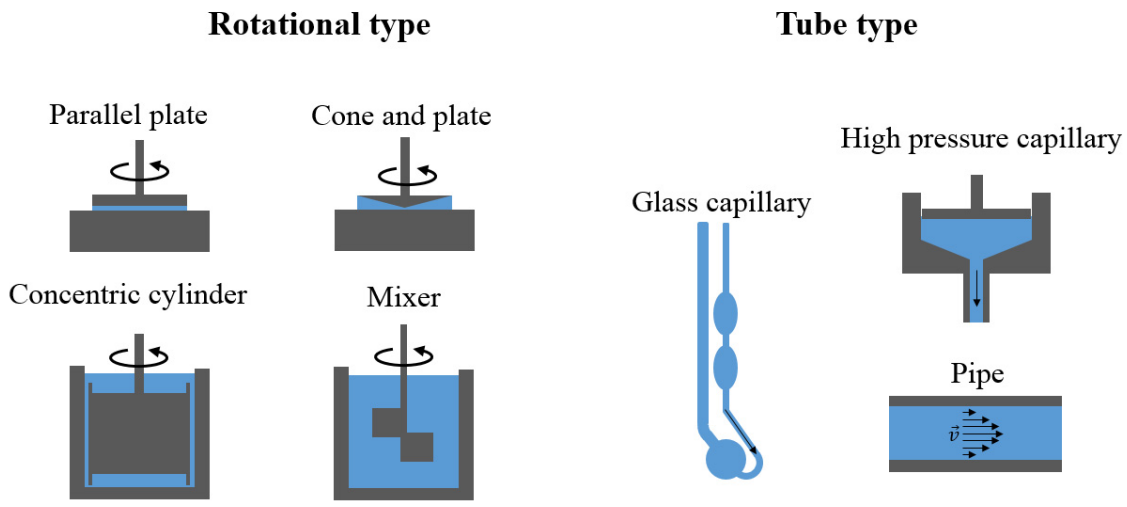

Figure 1.6 Typical rheometers are categorized into rotational and tube types, after [31].

First consider a geometry of a cone-plate rheometer as shown in Figure 1.7a. As the cone rotates, the fluid on the cone surface moves with a velocity of Ωr, where Ω is angular velocity and r is a radius. The gap between a cone and plate is $r\tan\theta$, where θ is the cone angle indicated in Figure 1.7a. The shearing flow produced by this geometry is a simple Couette flow. The shear rate can be expressed as:

Equation 1.2 $$\dot{\gamma} = \frac{velocity}{flow\ gap} = \frac{\Omega r}{r\tan\theta} = \frac{\Omega}{\tan\theta} \cong \frac{\Omega}{\theta}\ for\ small\ angle$$

Equation 1.2 shows that cone and plate rheometers create a constant shear rate on all the testing area. This is an important property of a cone-plate rheometer and makes it useful for characterizing the dependence of viscosity on shear rates. The typical cone angle is a small angle, below 3 degrees. So the shear rate is simply a ratio of angular velocity to cone angle. Next, the shear stress can also be derived easily as follows.

A force needed to maintain a certain shear rate over a small angular ring is

Equation 1.3 $$\Delta F = \tau_{z\theta} \cdot 2\pi r \cdot dr$$

And torque acting on this area is

Equation 1.4 $$\Delta M = \tau_{z\theta} \cdot 2\pi r^2 \cdot dr$$

The total torque, M, on the entire plate can be found by integrating over the whole radius *R*.

Equation 1.5 $$M = 2\pi\tau_{z\theta}\int_0^R r^2 dr = \frac{2\pi R^3}{3}\tau_{z\theta}$$

So by measuring the total torque acting on the cone, one can define the shear stress as

Equation 1.6 $$\tau_{z\theta} = \frac{3M}{2\pi R^3}$$

And by using the viscosity definition from Equation 1.1, the measured viscosity is defined as

Equation 1.7 $$\eta(\dot{\gamma}) = \frac{\tau_{z\theta}}{\dot{\gamma}} = \frac{3M}{2\pi R^3}\frac{\theta}{\Omega}$$

Because shear rate is a constant, by varying the angular velocity or acting torque the viscosity can be measured as a function of shear rate and, of course, time. Typically, to increase the sensitivity of torque measurements, the cone radius is made as large as possible. However, the larger cone needs more fluids, which in some cases is not practical. All cone-plate rheometers allow the cone to move away from the plate and disassemble from the instrument. It is crucial that the cone is installed with a precise gap between cone and plate such that Equation 1.2 holds. For the ideal cone and plate, the tip of cone touches the plate. This is a problem because solid contact and friction at the contact point prevents an accurate reading of *M*. To avoid this direct contact, the cone is normally truncated by a small amount. It is important to set an accurate virtual tip in order to precisely control the flow gaps and the shear rates as shown in Figure 1.7a. A small error in gap can cause significant error on the viscosity measurement. Modern rheometers use a micrometer or precise linear stage for this purpose. Moreover, it is important to load an accurate volume into a cone-plate rheometer. Too much volume creates a liquid bead on the edges, complicating the flow and adding extra torque, leading to an overestimate of the viscosity. Too little volume reduces an effective area of measurement and will lead to an underestimation of the viscosity. The cleanliness of the cone and plates is critical for making a

reliable measurement. Since the cone angle is very small, the gap is on the order of a few microns. Modern rheometers also precisely control the temperature of the cone and plate to get an accurate viscosity reading. An example of an advanced rheometer is shown in Figure 1.7b. This rheometer is capable of measuring a torque as small as 0.01 μNm and rotates as fast as 4500 rpm, which corresponds to a shear rate of ~10^4 s^{-1}. It can vary the temperature in range of -150 to 600 °C. Therefore, it can perform various testing methods for non-Newtonian fluids such as flow curve, creep test, and oscillation.

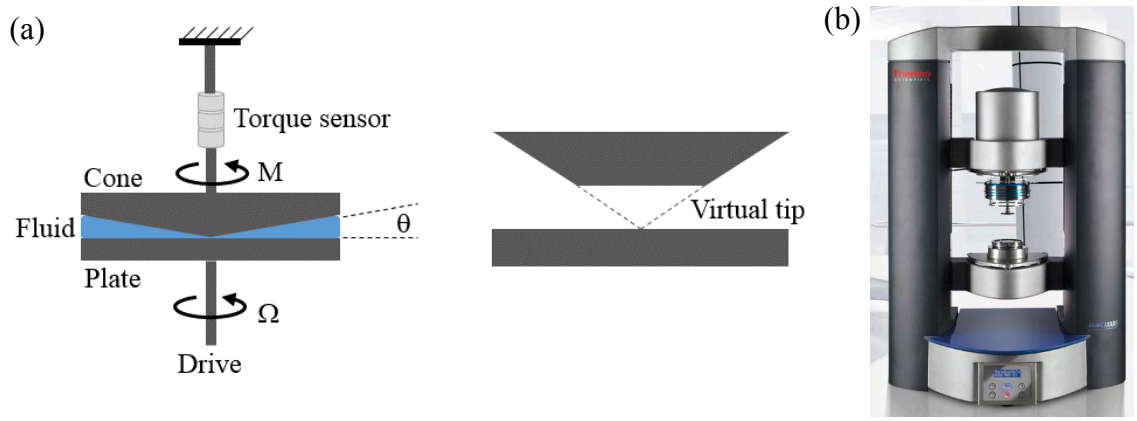

Figure 1.7 (a) A principal of cone-plate rheometer, after [28], and (b) a modern rheometer, HAAKE™ MARS III rotation rheometer. (image courtesy of Thermo scientific Inc.)

1.4.2 Surface tension

In addition to the viscosity, surface tension is another important fluid property, particularly for printed electronics. In printed electronics, surface tension plays an important role in pattern formation on non-absorbing substrates, like plastic, glass, and silicon wafers. The origin of surface tension can be explained easily by considering the differences between a molecule inside a bulk liquid and at the surfaces, as shown in Figure 1.8. In liquid, molecules attract each other with a force that is larger than that of thermal agitation. A molecule in a bulk liquid is in a happy state, because it benefits from all surrounding molecule. However, a molecule at the gas-liquid interface misses half of its attractive interactions. This is a fundamental reason that a liquid always adjusts its shape to minimize the gas-liquid interface area. Let us assume that the cohesion energy per molecule is U inside the liquid. The molecule at the interface will lack this energy by half due to missing interactions. The surface tension is a direct measure of this energy and can be defined as $\gamma \cong \frac{U}{2a^2}$, where a is a surface area per molecule. Therefore, surface tension has a unit of energy/area or mJ/m^2. Or one can state the surface tension is an energy required to create the surface area by one unit. Hence, the surface tension is also referred to as *surface energy*. The term surface energy is typically used to describe solid surfaces.

Although the surface tension originates at the molecular level, it is also a macroscopic property and can be mechanically measured through *Capillary forces*. The capillary force is a phenomena that gives another physical concept of the surface tension as a force per unit length. To understand this concept, let us consider a simple experiment where the surface tension manifests itself as a force, as shown in Figure 1.8b. This experiment is a surface tension measurement, called the ring detachment method. The experiment begins by immersing a metal ring, typically platinum, into a pool of liquid, followed by slowly lifting the ring upward until it detaches from hanging liquid surfaces. As the ring moves away from the liquid surface, the surface area increases as the interface deforms. Because a liquid always wants to minimize its surface area, the surface tension manifests itself as a force pulling the ring toward the original flat surface. Therefore, the surface tension force (capillary force) counteracts the external pulling force. When the liquid is deformed such that the liquid surface is vertically hanged from the ring, the pulling force reaches its maximum. Because the surfaces form on both the inner and outer rings, the total surface length is ~ $4\pi R$, assuming the ring diameter r is much smaller than R and the total capillary force is $4\pi R\gamma$. Therefore, one can find the surface tension by

Equation 1.8 $$F \cong 4\pi R\gamma \;\Rightarrow\; \gamma \cong \frac{F}{4\pi R}$$

In this case, the surface tension exhibits itself as a force per unit length and has a unit of mN/m. However, this simple schematic is quite erroneous due to a finite container and ring sizes that create surface curvatures, which prohibit the surface tension from acting vertically. A correction must be introduced to obtain an accurate measurement. Both molecular and mechanical concepts of surface tension are useful in practical applications. Each concept becomes more intuitive, depending on applications or problems. This will be clearer in the next section.

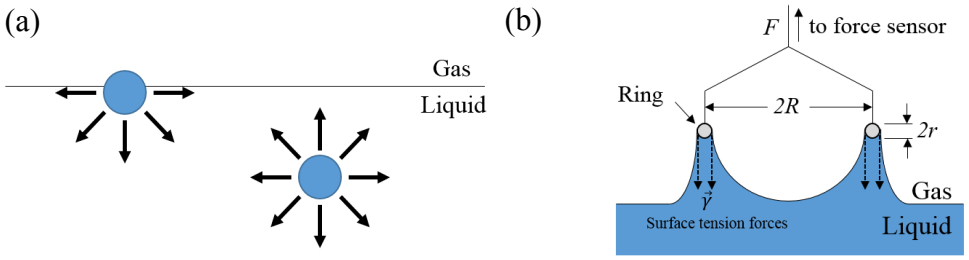

Figure 1.8 Physical concepts of surface tension through (a) molecular level and (b) capillary forces. The molecular concept gives a contrast between molecule inside bulk fluid and at the interface, in which it is missing half of its attractive interactions, after [32] (b) Experiment on the capillary force by detaching a ring from liquid surface, after [29]

There are several methods for measuring surface tension using the capillary forces such as plate detachment (Wihelmy plate), drop weight, capillary tube, and pendant drop. An instrument for measuring surface tension is called a tensiometer. Modern tensiometers can measure a wide range of surface tension (1 to 2000 mN/m) with a good resolution of 0.001 mN/m. Typically, it can control measurement temperature precisely as well. Temperature normally reduces the

surface tension, because as liquid is heated, the attractive interaction between molecules is reduced.

There are several surface flow phenomena that are important in printed electronics. For example, *Marangoni effect* is a surface flow that is induced by the surface-tension gradient of a mixture of two fluids. This effect is used to counteract a well-known *coffee ring effect* to achieve a dome-like profile [33]. A surface-tension gradient also promotes the formation of a uniform thin film in a liquid coating [34]. Dome-like and uniform structures are critical for thin-film electronic devices, because the electronic properties are controlled by local film thickness. In addition to the surface-tension gradient, curvatures of surfaces can produce flows as well. When an interface is curved, the pressure drop across the fluid surface is not zero due to asymmetry of the surface tension force. This effect is called *Laplace pressure*. The Laplace pressure is defined as an increment in hydrostatic pressure equal to the product of the surface tension and the curvature of the surface. Figure 1.9a demonstrates how to calculate the Laplace pressure at a particular point on the surface. First define a normal vector $\vec{n}$ pointing from liquid to gas phase. Then find two curvature radii that are normal to each other, with centers on $\vec{n}$. If the center is in the gas phase, the sign of the radius is negative. For example, a saddle surface shown in Figure 1.9a will have one negative and one positive radius. The pressure jump across the interface is defined as:

Equation 1.9
$$P_L - P_G = \gamma_{LG}\left(\frac{1}{R} + \frac{1}{R'}\right)$$

The Laplace pressure strongly affects the morphology of microstructure patterns, because the small radii and volume makes the capillary force dominate other forces, such as gravity and inertial. For example, Darhuber simulated a T-Shape pattern at equilibrium. The contact angles inside and outside the pattern are 10° and 135°. The small contact angle on the pattern area is required to prevent liquid from receding from the line to the pad. Figure 1.9b and c show top and side views at equilibrium. Notice a large height difference between large and narrow features. This can be viewed as an effect of the Laplace pressure. If the height is a constant, the Laplace pressure in a narrow line is higher than that in a pad. Therefore, liquid will flow from line to pad. As a result of this capillary flow, the line height decreases and the pad height increases. Eventually, the pressure is balanced and the flow stops. This causes uneven height as shown in Figure 1.9c and it is a concern in printed electronics where uniform thin films are desired.

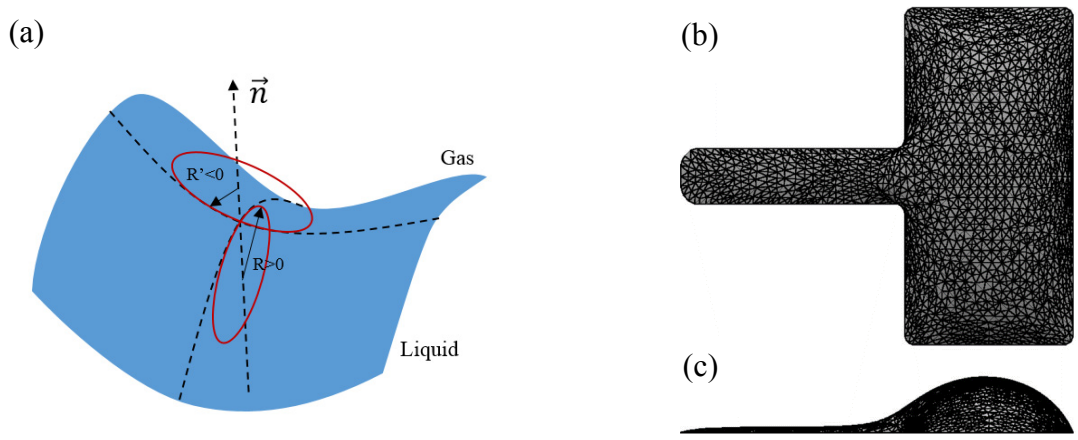

Figure 1.9 (a) Measuring the curvature of gas-liquid interface at a particular point. (b) and (c) effects of Laplace pressure on T-shape liquid pattern, reproduced from [35].

1.4.3 Wettability

Wettability is defined as a study of how a liquid deposited on a solid substrate spreads out. Precise printing for printed electronics requires great control and quantification of wettability. For example, printing a liquid line on plastic substrates requires control of liquid volume per unit length to minimize bulging and discontinuity of lines [36]. The wettability is roughly quantified by using *spreading parameters S*, defined as a difference of surface energy between wet and dry states [32]. The surface energy of the dry state is the surface energy of solid-gas interface γ_{SG}. And the surface energy of the wet state is a sum of solid-liquid γ_{SL} and liquid-gas γ_{LG} surface energy. Therefore, *S* can be expressed as:

Equation 1.10 $$S = \gamma_{SG} - (\gamma_{SL} + \gamma_{LG})$$

γ_{LG} is the surface tension as explained in 1.4.2. By using the spreading parameter, three-phase contacts of gas, liquid, and solid can be classified into two types, *total wetting* and *partial wetting*, depending on surface energies of each phase. If $S>0$, liquid spreads completely in order to lower the total energy of the system. This is called *total wetting*. On the other hand, if $S<0$, the liquid forms a spherical cap on a substrate with a contact angle θ_E. This contact angle is determined by Young's equation:

Equation 1.11 $$\gamma_{LG} \cos\theta_E = \gamma_{SG} - \gamma_{SL}$$

Young's equation can be derived by using a force balance at a contact line, since surface tension is a force per unit length. The sum of these three forces is equal to zero, because the contact line is stationary at equilibrium as shown in Figure 1.10a. Young's equation is an important equation in printed electronics, especially for pattern formation after printing where the liquid flows to its equilibrium. However, measuring θ_E can be challenging due to surface roughness and chemically heterogeneity of the surfaces. This can cause inconsistent readings of contact angles between advancing and receding contact angles. This is called contact angle hysteresis. The contact angle

also changes with the contact line speed. When the contact line moves, the contact angle can be larger and smaller than θ_E. As the contact line moves faster to cover a dry surface, the apparent contact angle increases. And as the contact line withdraws from a wet surface, the apparent contact angle decreases from the equilibrium angle. These are called dynamic contact angles. The change in contact angles can be interpreted in two ways based on: hydrodynamic theory and molecular-kinetic theory. The hydrodynamic theory describes the dynamic contact angle as a result of the viscous bending of the gas-liquid interface with a mesoscopic region at a scale below that of observation but greater than the molecular scale. The molecular-kinetic theory explains the phenomena by the molecular processes (attachment or detachment of fluid particles to or from the solid surface) near the contact line. Figure 1.10b summarizes a relationship of dynamic contact angle, hysteresis, advancing and receding contact angles as a function of contact line speed [37].

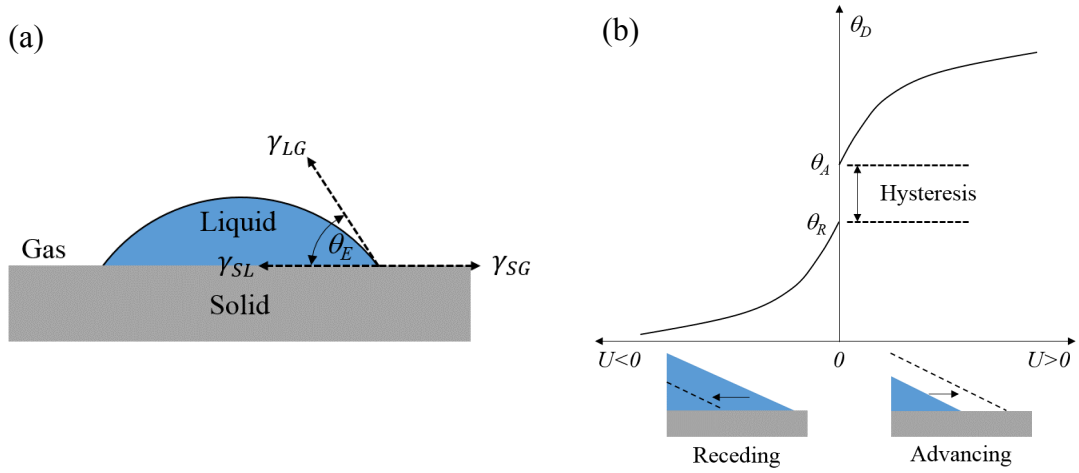

Figure 1.10 (a) Derivation of Young's equation using force balance at the contact line. (b) dynamic contact angles as a function of contact line speeds, including contact angle hysteresis.

1.4.4 Outline of the thesis

In this work, various aspects of gravure printing will be addressed. The main foci are to understand the physics of gravure printing, demonstrate the ultimate patterning resolution of gravure, implement/develop gravure technology toward a manufacturing scale, and demonstrate electronic devices using gravure printing. In the second chapter, a simple model of gravure printing will be proposed. This chapter explains and simplifies complicated printing mechanisms into simpler steps that are more understandable in term of experiments and theoretical analysis. The proposed model shows that individual steps can be linked by using a single non-dimensionless number, the Capillary number, due to the small length scale. In the third chapter, lubrication-related residue film will be analyzed in-depth. This lubrication-related residue film is a fundamental limit for pattern scaling in gravure printing. The lubrication regime during wiping is proposed based on experimental results. According to the indicated lubrication regime, a new doctor blade geometry is proposed to overcome the limitation and achieve extraordinary printing resolution at high speed. In the fourth chapter, the filling process will be discussed intensely. The

limitation of this process puts an upper limit on the speed of gravure printing. The failure mechanism is examined carefully and a potential solution is proposed. The fifth chapter demonstrates a roll fabrication process for high-resolution gravure roll. This fabrication process incorporates knowledge from prior chapters to implement the highest resolution gravure roll to-date. Then, fully printed thin film transistors are demonstrated in the sixth chapter. This illustrates the ultimate potential of gravure printing as a high-resolution, high-speed printing technique for mass production of printed electronics. Finally, the last chapter will discuss future challenges that require pushing gravure to the next level, such as sub-μm features, multiple film thicknesses, multiple layers, and etc., in order to be addressed.

1.5 References

[1] M. Kaltenbrunner, T. Sekitani, J. Reeder, T. Yokota, K. Kuribara, T. Tokuhara, M. Drack, R. Schwödiauer, I. Graz, S. Bauer-Gogonea, S. Bauer, and T. Someya, "An ultra-lightweight design for imperceptible plastic electronics.," *Nature*, vol. 499, no. 7459, pp. 458–63, Jul. 2013.

[2] D.-H. Kim, N. Lu, R. Ma, Y.-S. Kim, R.-H. Kim, S. Wang, J. Wu, S. M. Won, H. Tao, A. Islam, K. J. Yu, T. Kim, R. Chowdhury, M. Ying, L. Xu, M. Li, H.-J. Chung, H. Keum, M. McCormick, P. Liu, Y.-W. Zhang, F. G. Omenetto, Y. Huang, T. Coleman, and J. a Rogers, "Epidermal electronics.," *Science*, vol. 333, no. 6044, pp. 838–43, Aug. 2011.

[3] J. A. Rogers, Z. Bao, K. Baldwin, A. Dodabalapur, B. Crone, V. R. Raju, V. Kuck, H. Katz, K. Amundson, J. Ewing, and P. Drzaic, "Paper-like electronic displays: large-area rubber-stamped plastic sheets of electronics and microencapsulated electrophoretic inks.," *Proc. Natl. Acad. Sci. U. S. A.*, vol. 98, no. 9, pp. 4835–40, Apr. 2001.

[4] M. Jung, J. J. Kim, J. Noh, N. Lim, C. Lim, G. Lee, H. Kang, K. Jung, A. D. Leonard, J. M. Tour, and G. Cho, "All-Printed and Roll-to-Roll-Printable 13.56-MHz-Operated 1-bit RF Tag on Plastic Foils," *IEEE Trans. Electron Devices*, vol. 57, no. 3, pp. 571–580, Mar. 2010.

[5] E. Cantatore, *Applications of Organic and Printed Electronics: A technology-Enabled Revolution*. .

[6] G. L. Riddell, "The structure of the printing industry.," *Ann. Occup. Hyg.*, vol. 16, no. 2, pp. 141–9, Aug. 1973.

[7] K. Gillett, "Gravure—Process and Technology," *GAA GEF, Rochester, 2nd Ed. New York*, 2003.

[8] T. Sekitani, Y. Noguchi, U. Zschieschang, H. Klauk, and T. Someya, "Organic transistors manufactured using inkjet technology with subfemtoliter accuracy.," *Proc. Natl. Acad. Sci. U. S. A.*, vol. 105, no. 13, pp. 4976–80, Apr. 2008.

[9] H.-Y. Tseng, B. Purushothaman, J. Anthony, and V. Subramanian, “High-speed organic transistors fabricated using a novel hybrid-printing technique,” *Org. Electron.*, vol. 12, no. 7, pp. 1120–1125, Jul. 2011.

[10] J. Rogers and R. Nuzzo, “Recent progress in soft lithography,” *Mater. today*, no. February, pp. 50–56, 2005.

[11] S. H. S. H. Ahn and L. J. Guo, “High-Speed Roll-to-Roll Nanoimprint Lithography on Flexible Plastic Substrates,” *Adv. Mater.*, vol. 20, no. 11, pp. 2044–2049, Jun. 2008.

[12] K. Jain, M. Klosner, M. Zemel, and S. Raghunandan, “Flexible Electronics and Displays: High-Resolution, Roll-to-Roll, Projection Lithography and Photoablation Processing Technologies for High-Throughput Production,” *Proc. IEEE*, vol. 93, no. 8, pp. 1500–1510, Aug. 2005.

[13] D. Deganello, J. a. Cherry, D. T. Gethin, and T. C. Claypole, “Patterning of micro-scale conductive networks using reel-to-reel flexographic printing,” *Thin Solid Films*, vol. 518, no. 21, pp. 6113–6116, Aug. 2010.

[14] E. Hrehorova, M. Rebros, A. Pekarovicova, B. Bazuin, A. Ranganathan, and S. Garner, “Gravure Printing of Conductive Inks on Glass Substrates for Applications in Printed Electronics,” *J. Disp. Technol.*, vol. 7, no. 6, pp. 318–324, 2011.

[15] M. Pudas, J. Hagberg, and S. Leppävuori, “Gravure offset printing of polymer inks for conductors,” *Prog. Org. Coatings*, vol. 49, no. 4, pp. 324–335, May 2004.

[16] F. C. Krebs, J. Fyenbo, and M. Jørgensen, “Product integration of compact roll-to-roll processed polymer solar cell modules: methods and manufacture using flexographic printing, slot-die coating and rotary screen printing,” *J. Mater. Chem.*, vol. 20, no. 41, p. 8994, 2010.

[17] R. Parashkov, E. Becker, T. Riedl, H.-H. Johannes, and W. Kowalsky, “Large Area Electronics Using Printing Methods,” *Proc. IEEE*, vol. 93, no. 7, pp. 1321–1329, Jul. 2005.

[18] V. Subramanian, A. de la F. Vornbrock, S. Molesa, D. Soltman, and H.-Y. Tseng, “Printing Techniques for Thin Film Electronics,” in *Electronics II*, 1st ed., Wiley Online Library, 2012.

[19] Y. Galagan, I. G. de Vries, A. P. Langen, R. Andriessen, W. J. H. Verhees, S. C. Veenstra, and J. M. Kroon, “Technology development for roll-to-roll production of organic photovoltaics,” *Chem. Eng. Process. Process Intensif.*, vol. 50, no. 5–6, pp. 454–461, May 2011.

[20] a. Huebler, U. Hahn, W. Beier, N. Lasch, and T. Fischer, "High volume printing technologies for the production of polymer electronic structures," *2nd Int. IEEE Conf. Polym. Adhes. Microelectron. Photonics. POLYTRONIC 2002. Conf. Proc. (Cat. No.02EX599)*, pp. 172–176, 2002.

[21] F. C. Krebs, "Fabrication and processing of polymer solar cells: A review of printing and coating techniques," *Sol. Energy Mater. Sol. Cells*, vol. 93, no. 4, pp. 394–412, Apr. 2009.

[22] M. Jung, J. Kim, J. Noh, N. Lim, C. Lim, G. Lee, J. Kim, H. Kang, K. Jung, A. D. Leonard, J. M. Tour, and G. Cho, "All-Printed and Roll-to-Roll-Printable 13.56-MHz-Operated 1-bit RF Tag on Plastic Foils," *IEEE Trans. Electron Devices*, vol. 57, no. 3, pp. 571–580, Mar. 2010.

[23] A. de la Fuente Vornbrock, D. Sung, H. Kang, R. Kitsomboonloha, and V. Subramanian, "Fully gravure and ink-jet printed high speed pBTTT organic thin film transistors," *Org. Electron.*, vol. 11, no. 12, pp. 2037–2044, Dec. 2010.

[24] J. Puetz and M. a. Aegerter, "Direct gravure printing of indium tin oxide nanoparticle patterns on polymer foils," *Thin Solid Films*, vol. 516, no. 14, pp. 4495–4501, May 2008.

[25] D. Sung, A. de la Fuente Vornbrock, and V. Subramanian, "Scaling and Optimization of Gravure-Printed Silver Nanoparticle Lines for Printed Electronics," *Components Packag. Technol. IEEE Trans.*, vol. 33, no. 1, pp. 105–114, 2010.

[26] J. Noh, D. Yeom, C. Lim, H. Cha, J. Han, J. Kim, Y. Park, V. Subramanian, and G. Cho, "Scalability of Roll-to-Roll Gravure-Printed Electrodes on Plastic Foils," *IEEE Trans. Electron. Packag. Manuf.*, vol. 33, no. 4, pp. 275–283, Oct. 2010.

[27] G. Henning, K.-H. H. Selbmann, S. Mattheus, R. Kecke, Stephen Bruning, G. Hennig, and S. Brüning, "Laser Precision Micro Fabrication in the Printing Industry," *J. Laser Micro/Nanoengineering*, vol. 1, no. 2, pp. 89–98, Jul. 2006.

[28] H. Barnes and J. F. Hutton, *An introduction to rheology*, vol. 1. Elsevier Science B.V., 1989.

[29] T. C. Patton, *Paint flow and pigment dispersion*. Wiley-Interscience, 1964.

[30] D. Dowson, "Elastohydrodynamic and micro-elastohydrodynamic lubrication," *Wear*, vol. 190, pp. 125–138, 1995.

[31] J. F. Steffe, *Rheological methods in food process engineering*. Freeman press, 1996.

[32] P. De Gennes, F. Brochard-Wyart, and D. Quere, *Capillarity and wetting phenomena: drops, bubbles, pearls, waves*. Springer, 2004.

[33] H. Hu and R. G. Larson, “Marangoni Effect Reverses Coffee-Ring Depositions,” *J. Phys. Chem. B*, vol. 110, no. 14, pp. 7090–7094, Apr. 2006.

[34] M. H. Eres, D. E. Weidner, and L. W. Schwartz, “Three-Dimensional Direct Numerical Simulation of Surface-Tension-Gradient Effects on the Leveling of an Evaporating Multicomponent Fluid,” vol. 35, no. 24, pp. 1859–1871, 1999.

[35] A. Darhuber, S. Troian, and S. Miller, “Morphology of liquid microstructures on chemically patterned surfaces,” *J. Appl.*, vol. 87, no. 11, p. 7768, 2000.

[36] D. Soltman and V. Subramanian, “Inkjet-printed line morphologies and temperature control of the coffee ring effect.,” *Langmuir*, vol. 24, no. 5, pp. 2224–31, Mar. 2008.

[37] T. D. Blake, “The physics of moving wetting lines.,” *J. Colloid Interface Sci.*, vol. 299, no. 1, pp. 1–13, Jul. 2006.

Chapter 2 A Simple Model of Highly Scaled Gravure Printing

Direct gravure printing is promising in that it delivers high throughput and has a proven history of being manufacturing worthy. Unfortunately, it suffers from scalability challenges due to limitations in roll manufacturing and limited understanding of the relevant printing mechanisms. Gravure printing involves interactions between the ink, the patterned cylinder master, the doctor blade that wipes excess ink, and the substrate to which the pattern is transferred. As gravure printed features are scaled, the associated complexities are increased, and a detailed study of the various processes involved is lacking. In this chapter, the various gravure-related fluidic mechanisms using a novel highly scaled inverse direct gravure printer will be discussed. The printer allows us to study the overall pattern formation process in detail by separating the entire printing process into three sequential steps: filling, wiping, and transferring. The results suggests that pattern formation via highly scaled gravure printing is governed by the wettability of the ink to the printing plate, doctor blade and substrate. These individual functions are linked by the apparent Capillary number (Ca); the printed volume fraction (φ_p) of a feature can be constructed by incorporating these basis functions. By relating Ca and φ_p, an optimized operation point can be specified and the associated limiting phenomena can be identified. This relationship was used to find the optimized ink viscosity and printing speed to achieve printed polymer lines and line spacing as small as 2 μm at printing speeds as high as ~1 m/s. This is virtually impossible to achieve using non-contact printing techniques due to fact that the placement accuracy and throughput decreases as the droplet size is reduced. Although residues on non-patterned areas are a major concern for contact printing processes, it will be shown that this problem can be mitigated by understanding and optimizing printing conditions. All results in this chapter are published in [1].

2.1 Introduction

Droplet formation during printing has been studied for many years. Bogy provided a basic understanding of droplet formation via droplet-on-demand inkjet printing in 1984 [2]. This work guided the later development of pieozoelectric inkjet printheads. In contrast to drop-on demand inkjet printing, a comprehensive explanation of highly scaled gravure printing does not exist. Literature reports normally treat only one part of the numerous process steps involved in gravure printing, namely, the transferring process [3]–[8]. Bery attempted to provide some qualitative insights into the printing mechanisms in conventional gravure printing based on experimental results, albeit at a much larger length scale [9]. This absence of detailed knowledge has impeded feature size scaling since sensitivity to the various surface-related phenomena become increasingly important as pattern sizes are scaled.

For the printing of fine features such as gate electrodes for thin film transistors and interconnects for displays and photovoltaic cells, typical engraved patterns consist of only a one-dimensional string of cells, instead of an array of cells. This indicates that a study of individual cells is a viable point to elucidate the printing mechanisms associated with gravure printing; this can subsequently be extended to a string of cells or an array of cells. Therefore, a simple mechanistic

model to describe pattern formation by gravure printing is proposed here. We define the relevant processes, perform experiments to reveal the mechanistic underpinnings of each process, and then use these results to propose a simple model for gravure printing including the same. We validate the model with experimental data, and demonstrate that the proposed model can indicate the correct ink viscosity and printing speed to obtain optimal pattern fidelity for printed features as small as 2 μm, which, to the best of our knowledge, is the smallest reported feature size for a high speed printing technique.

2.2 System definitions

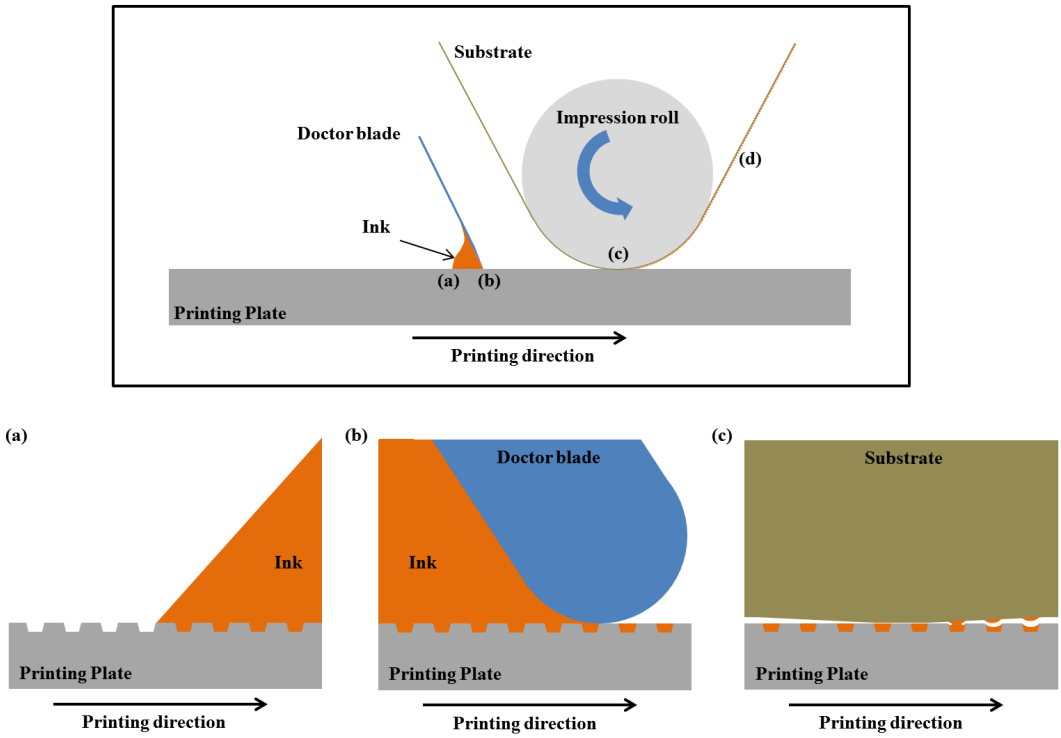

Figure 2.1 Inverse direct gravure printing process (top figure) and its internal process steps (bottom figures) defined as (a) filling, (b) wiping, (c) transferring, and (d) free surface formation process.

We introduce a printer that allows us to perform experimental analyses of the processes occurring during gravure printing. We call this "inverse direct gravure printing" since the printer uses a flat plate to transfer patterns to a substrate on a roll, rather than using a roll to transfer patterns to a sheet or roll of film substrate; this setup allows for direct imaging of the individual processes. All length scales, time scales, and interacting materials (substrates, inks, printing plates) are chosen so as to maintain quantitative applicability to a direct gravure system as well. Figure 2.1 shows the processes that occur when patterns are printed onto a substrate by gravure printing. (a) Filling: cells engraved on the printing plate are over-filled with ink as the plate moves under the stationary contact line. (b) Wiping: much of the excess ink is removed as the plate moves under the doctor blade. (c) Transfer: the moving substrate contacts the free surface of the ink in the well, and ink is pulled from the well onto the substrate. After printing, the

pattern shape may change to attain the state of lowest surface energy, but we do not treat this problem here, since we and others have addressed surface energy minimization during drying in previous work [10]–[14].

The goal of this chapter is to develop a mechanistic understanding of pattern formation by gravure printing and to find a relationship between printing quality, ink properties and printing conditions. This relationship can be used to understand and optimize the overall printing process to achieve high resolution features, as are needed for the realization of printed electronics. In particular, the printing quality is characterized by the contrast between the printed droplet volume and the residue volume. The printed droplet volume refers to the volume printed directly by an engraved cell and the residue volume refers to the volume of undesired ink printed on non-patterned areas surrounding the droplet. To obtain a dimensionless number for printing quality, the volume of interest is normalized by the relevant volume. The printed volume fraction φ_p is defined as the volume of a printed aliquot divided by the volume of the engraved cell. Because the aliquot is produced by a series of processes, namely, filling φ_f, wiping φ_w and transferring φ_t, φ_p can also be simply defined as a product of these processes, as in (1). For the residue volumes, there are two possible paths for the formation of undesired residues. The first is the drag-out of ink from the cells by the doctor blade, which we define as the drag-out volume $\varphi_d = {V_d}/{V_c}$. The second is a lubrication film that can develop between the doctor blade and the printing plate, which we define as φ_l. The residue volumes will be discussed further in the wiping section below.

Equation 2.1

$$\varphi_p = \varphi_f \varphi_w \varphi_t$$

And

$$\varphi_p = \frac{V_p}{V_c}, \varphi_f = \frac{V_f}{V_c}, \varphi_w = \frac{V_r}{V_f}, \varphi_t = \frac{V_p}{V_r}$$

Where V_c = cell volume

V_p = printed volume

V_f = filled volume

V_d = drag-out volume

$V_r = V_f - V_d$ = remaining volume

Next, another dimensionless number is calculated from the ink properties and printing conditions. In our case, the viscous and surface tension forces dominate inertial and gravity forces, because of the microscale dimension of the engraved cells. In additional, the flow mechanisms in the filling, wiping and transferring are driven by wettability of the ink to the printing plate, doctor blade, and substrate. Therefore, a suitable dimensionless number is the Capillary number, Ca, which represents the ratio of viscous to surface tension forces and is typically used to describe the wettability. To ensure that gravity and inertial forces are negligible

in highly scaled gravure printing, the Bond and Weber numbers are calculated and they are less than 10^{-8} and 10^{-5} with respect to cell width. This makes the highly scaled inverse direct gravure a good representative of direct gravure and the capillary number a governing parameter. The dimensionless numbers used in this work are defined as the follows.

Equation 2.2 $$Capillary\ number\ (Ca) = \frac{\eta U}{\gamma}$$

Equation 2.3 $$Bond\ number\ (Bo) = \frac{\rho g L^2}{\gamma}$$

Equation 2.4 $$Weber\ number\ (We) = \frac{\rho U^2 L}{\gamma}$$

Where: η = apparent viscosity

U = printing speed

γ = surface tension

ρ = fluid density

L = characteristic length

g = gravitational acceleration

Although our solutions are shear thinning at lower strain rate, the viscosity asymptotes to a constant value for strain rates exceeding values of 10^3 s^{-1}. We therefore can establish a Ca calculated from the high shear rate viscosity. We also ignore the elasticity of the solutions, because our solutions showed viscous behaviors under a creep test at high shear stress. This will be discussed further, along with the rheological behavior of test fluids in the ink rheology section. In the filling and wiping processes, the Ca can be calculated by using typical ink viscosities and printing speeds and the Capillary number in the printing direction Ca_x is in the range of 0.01 to 10. In the transferring process, a suitable velocity is the perpendicularly approaching/departing velocity of the substrate with respect to the printing plate, which can be calculated from the printing speed and the roll curvature, and the Capillary number Ca_y in the transferring process is one tenth of Ca_x. Thus, these three processes can be linked together by one parameter, which will be called simply Ca. Since the printed volume fraction is a product of filling φ_f, wiping φ_w and transferring φ_t, a diagram of φ_p vs. Ca can be constructed theoretically. This diagram provides fundamental insights into the limiting process steps and scalability of gravure printing. The printed volume fraction is considered an output signal of the system. A higher φ_p gives a higher film thickness per unit area and better utilization of the ink. On the same plot, the printed residue volume fractions, φ_d and φ_l , can be accommodated; these can be considered to be undesired noise of the system. By combining feature and residue volume fractions on the same axis, signal-to-noise ratio can be indicated as the ratio of these two functions. The optimized operation point is where the maximum contrast between feature and

residue volume fractions is located. The volume fractions are plotted versus Ca, which indicates the printing speed, ink viscosity and surface tension. This parameter thus captures printing conditions and ink properties.

2.3 Experimental section

Ink rheology is clearly of importance in understanding the mechanisms associated with gravure printing. In printed electronics, the most widely used inks are nanoparticle colloids and polymeric solutions. A polymer solution was selected for this study due to the availability, reproducibility, and usability of the same. The polymer selected is poly(4-vinylphenol) (PVP) [M_w ~11000, part number 436216 from Sigma-Aldrich] and the solvent used is propylene glycol monomethyl ether acetate (PGMEA) from the same company. PVP is widely used as a gate dielectric in printed transistors [15], and therefore, is an excellent candidate material for this study. The concentration was varied from 25 to 35 wt%, and was adjusted to achieve the desired viscosity. The rheological properties of the inks were measured using a cone-plate rheometer (HAAKE RheoScope1). We also used silicone oil to investigate the flow behavior in the filling and wiping processes. The silicone oil is a viscosity standard from Brookfield Engineering with a nominal viscosity of 29,040 mPa·s. Contact angles mentioned herein were measured using a sessile droplet method (DSA10-MK2 from Kruss).

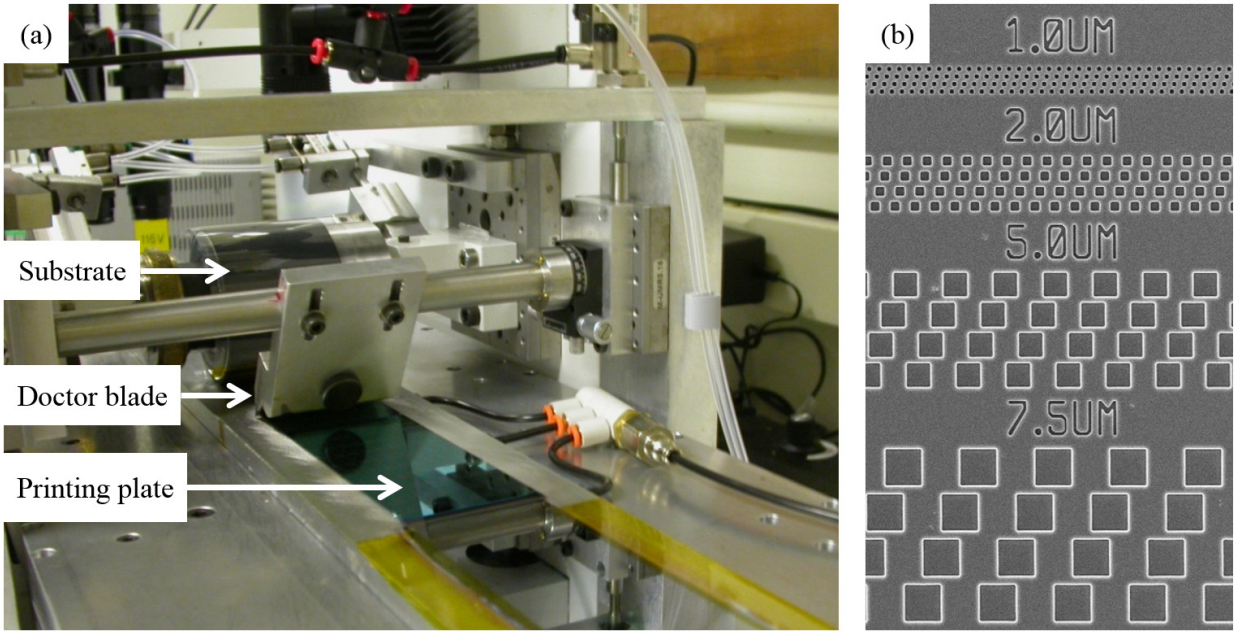

Figure 2.2 (a) Highly scaled inverse direct gravure printer (b) a micrograph of micro cells fabricated by lithography and dry etching processes. The cell width is varied from 1 to 7.5 μm.

Studying highly scaled direct gravure printing is a difficult task, because of its small features, high printing speed and roll curvature. An engraving method that can fabricate cell widths down to 1 μm with a cell spacing less than half of the cell width is still not available commercially. To

facilitate a study of gravure printing and to investigate the limits of feature scalability, a highly scaled inverse direct gravure printing system was developed. The printer shown in Figure 2.2a consists of three main components: a printing plate, doctor blade and impression roll. To limit the study to the limits of highly scaled gravure printing, the cell width of interest is 1 to 10 μm and the cell aspect ratio of height to width was kept constant at 0.5. The printer consists of three main components; printing plates, a doctor blade and an impression roll. The printing plate was mounted on a vacuum chuck, which can be advanced at a specified speed by a DC linear motor. The doctor blade was clamped on a mechanical housing and the angle between the printing plate and the doctor blade was fixed at 75°. Substrates were Q65FA polyethylene naphthalate (PEN) from DuPont Teijin, unless otherwise mentioned. The impression roll was a rubber roll for UV-inks from IGT (part number 402.090). Its hardness is 65 Shore A and diameter is 66 mm. During printing a substrate was wrapped on the impression roll and held by Kapton tape at the edges. The roll pressure was held constant for all experiments.

The printing plates were fabricated from 6" silicon wafers. First thermal oxide was growth by using wet oxidation and the target thickness was 1μm. Features were patterned by standard optical lithography using an ASML 5500/300 stepper. The patterns in the photoresist were transferred to the oxide layer by dry etching (Rainbow 4520) using a gas mixture of CHF_3 and CF_4. The patterned oxide layer was used as a hard mask for etching the silicon wafer to the desired depth. The silicon was etched using a transformer coupled plasma etcher (using a gas mixture of Cl_2 and CHF_3). By using these processes, we can produce cell width down to 1 μm with a minimum cell gap of 0.25 μm. The typical cell geometry is shown in Figure 2.2b.

The inverse direct gravure printing system allows for independent study of filling and wiping. The filling process, during which fluid enters an engraved cell, was simulated by dropping a large volume (500μl) of fluid on a printing plate and by allowing the fluid to spread out at controlled speed. Then, the filling process was recorded in real time via a microscope with a digital camera (Sony NEX-5n). The associated time scale of filling was slowed down by using high viscosity fluids where appropriate. The wiping process, in which excess fluid is removed by a doctor blade, was simulated by first inking the printing plate to ensure complete filling, and then moving the printing plate at a controlled speed under a doctor blade. Video was captured using long-working-distance high magnification lenses (12x Zoom Navitar with Mitutoyo 10x objective) with the same digital camera as above. Filling and wiping processes were studied for both silicone oil and PVP solutions.

It was not straightforward to study transferring, since imaging the three dimensional contact region between the plate and substrate over the entire length of the transfer zone is experimentally not possible. Therefore, literature-reported simulation results were used to provide the quantitative dependencies of the transfer process[6]. Finally, a complete gravure printing process was performed to verify the proposed model by measuring the printed volume as a function of ink viscosity and printing speed. The viscosity and printing speed were adjusted to cover a wide range of values for the Capillary number. The printed volume was measured by following steps. First, printed samples were dried on a hotplate at 100°C for 5 min and left at

room temperature for at least 3 hr to ensure complete solvent evaporation and solidification before measuring the printed volume. Then, samples were uniformly coated with thermally evaporated silver in order to increase the reflectivity and to homogenize the reflective index of the resulting samples. A dried film surface profile was measured using an interferometer in phase shift mode (Wyko NT3300). The total magnification was 20.5x and the resolution of measurement was 410 nm and 1 nm in lateral and vertical directions respectively. The silver film thickness was 50-100 nm. This surface profile was extracted from the resulting contours and the dried film volume was calculated by simply integrating over the printed area. The printed area was defined by a threshold level defined by the background noise. Then, the dried volume was converted to a corresponding wet volume using the known concentration of the polymer solution. Wet volumes reported here are a mean of 6 dots on 16 different locations across a substrate area of 40 mm by 40 mm. A chess board pattern was used as a sampling pattern. Drag-out and printed volume fractions were calculated using this wet volume. The important experimental parameters are summarized in Table 2.1. Finally, by using the proposed model, we were able to select the right viscosity and printing speed to realize printed lines and spacing as small as 2 μm, attesting to the importance of proper mechanistic understanding.

Table 2.1 Important experimental parameters

Physical parameters	
Printing speed	0.01 – 1.00 m/s
Apparent viscosity	50-500 mPa-s
Polymer concentration	25-35 wt%
Solvent surface tension	0.0269 N/m
Cell width	1-10μm
Cell aspect ratio (height to width)	0.5
Cell gap	0.25 μm
Blade tip radius	75 μm
Blade tip length	1200 μm
Blade body thickness	200 μm
Blade body length protruded from the blade holder	4000 μm
Blade advancing contact angle	78°
Impression roll diameter	60 mm
Printing width	50 mm

2.4 Results and discussions

2.4.5 Ink rheology

Because concentrated polymer solutions are known to be shear thinning fluids, the apparent viscosity during gravure printing depends on the shear rates of each associated step. We approximate the shear rate as the velocity divided by the relevant length scale. This is a good approximation for micro-scale flows where the velocity does not vigorously change.

Table 2.2 Estimated shear rates in highly scaled gravure printing.

Process	Velocity (m/sec)	Length scale (m)	Shear rate (s^{-1})
Filling	Printing speed ~1 m/s	Cell width <10 μm	$>10^5$
Wiping	Printing speed ~1 m/s	Doctor blade gap height ~10 nm	$\sim10^6$
		Cell height <5 μm	$>2x10^5$
Transferring	Departure speed ~0.1 m/s	Cell width <10 μm	$>10^4$

Table 2.2 shows that the estimated shear rates in highly scaled gravure printing, where the cell width is smaller than 10μm, are on order of 10^4 s^{-1} or higher. The length scale in the filling process is the width of the engraved cell because of the deformation of fluid during the filling process. The velocity is the printing speed; this indicates the maximum velocity needed to fill the engraved cell. In the wiping process, there are two length scales; one is the gap between the doctor blade and the printing plate and the other is the gap between the doctor blade and the bottom of the engraved cell, i.e. the cell height. The velocity is the printing speed, which is the speed at which the doctor blade is translated over the printing plate. The transferring length scale is also the width of the engraved cell, but the velocity is a departing velocity, which is calculated from the printing speed and the roll curvature.

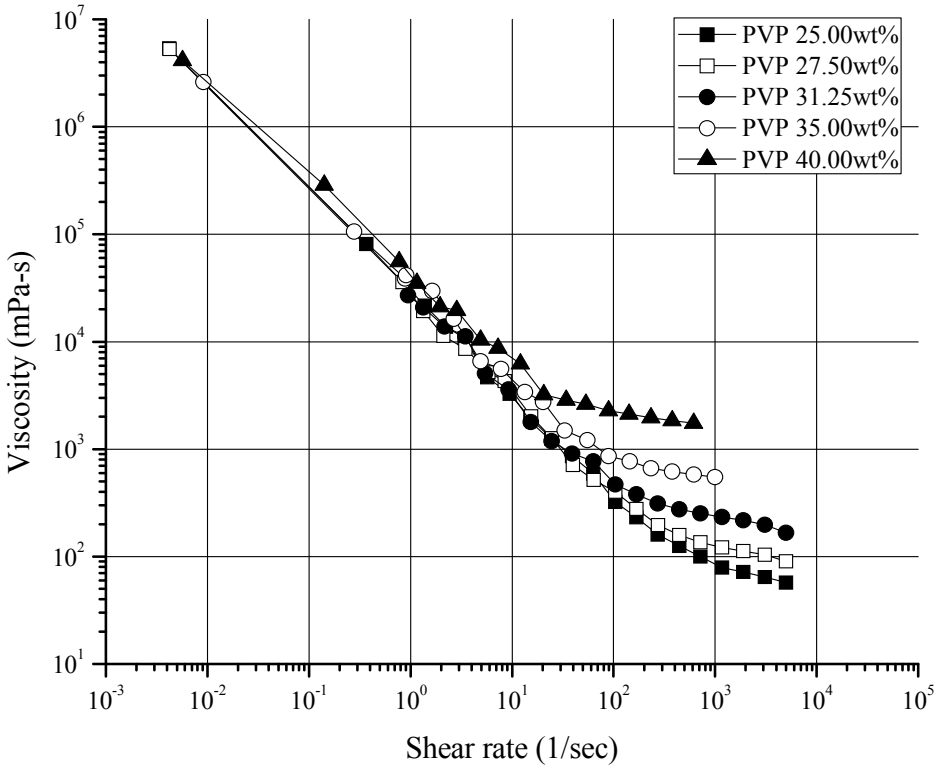

Figure 2.3 Viscosity of a solution of PVP in PGMEA as a function of shear rate with concentration as a parameter. The solutions are shear-thinning at shear rates of 10^{-2} to 10 s^{-1}. At high shear rates the viscosity approaches a finite constant value. The viscosity increases as the polymer concentration in the ink increases.

The viscosity of PVP in PGMEA as a function of shear rate, with polymer concentration as a parameter, is showed in Figure 2.3. The curves indicate that as the shear rate increases the dependence of viscosity on the shear rate reduces significantly. The maximum shear rate measured was limited by the capability of the rheometer. However, in the limit of very high shear rate as appropriate to this study, the apparent viscosity of polymer solutions approaches a constant viscosity η_∞; this region is known as the upper Newtonian region [16]. Figure 2.3 also specifies the onset of this region as 10^4 s^{-1}. Because the relevant shear rates are higher than the onset, it is reasonable to assume that viscosity is a constant throughout the printing process. By using a Sisko model [17] , η_∞ can be extracted from the flow curve shown in Figure 2.3 and in our experiment $\eta_\infty = 0.1382e^{0.23225*\text{PVP concentration in wt\%}}$ mPa-s. Because the η_∞ depends exponentially on the polymer concentration, the viscosity is effectively adjusted by varying concentrations without altering other ink properties significantly. To assure that the elasticity of PVP solutions has minimum effects on flow behaviors, we preformed creep tests at high shear stress corresponding to the shear rates present in gravure printing using a cone-plate rheometer (HAAKE RheoScope1). A constant shear stress of 100 Pa was applied between time 0 to 60 s and the shear strain was measured during this period. After time equaled to 60sec, the shear stress was set to 0Pa and the shear strain was recorded for further 60sec to observe the elasticity of PVP solution.

The results indicated that the PVP solutions show a viscous behavior for all concentrations used in this study. The shear strain was linearly proportional to time immediately after applying high shear stress and there was no significant elastic relaxation after removing the shear stress. Therefore, we concluded that the elasticity of our polymer solution has negligible effects in our experiments. The corresponding data is shown in Figure 2.4. In the next section, we will discuss the individual printing processes in detail.

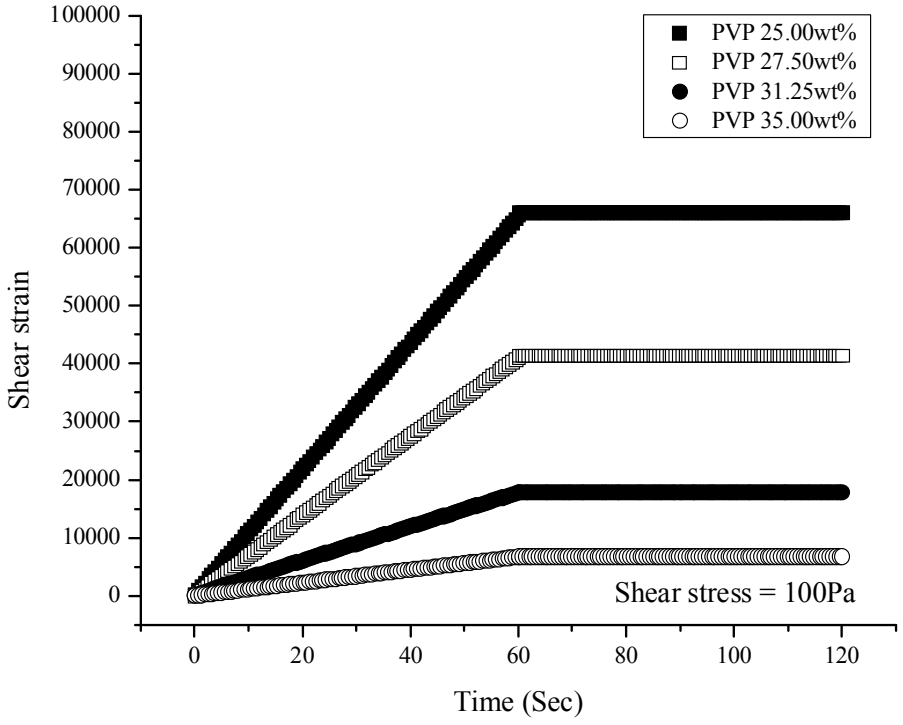

Figure 2.4 Creep test of PVP solutions at shear stress of 100 Pa

2.4.6 Filling process

Filling is a process that involves a moving contact line and deformation of fluid into an engraved cell. We begin by considering the dynamics of contact lines on a smooth surface. Hoffman reported the change of contact angle as a function of Ca [18]. The advancing contact angle approaches 180°, regardless of its static contact angle as Ca is increased. This is known as Hoffman's law. Recently, Carré developed a kinetic law of spreading for shear thinning fluids and partial wetting systems [19]. The theory predicts that the dynamic contact angle monotonically increases as a function of Ca; it reduces to Hoffman's law in the case of complete wetting. The change in contact angle can be explained by the fact that a large capillary number indicates that the viscous force dominates the surface tension force. Recall that the Ca of interest ranges from 0.01 to 10 and the static contact angle between the PVP solution and the printing plate was measured as <15°. Therefore, the dynamic contact angle of the liquid/solid interface

ranges from very small (<15°) to very large (~180°) depending on Ca. Hirt simulated the dynamics of advancing contact lines on smooth and featured surfaces [20]. On smooth surfaces the dynamic contact angle changes corresponding to the capillary number, supporting Hoffman's experiment [18]. In the case of roughened surfaces, the simulation indicates the existence of air entrapment. This condition could potentially exist during gravure printing at high Ca.

Next, we consider the filling of an engraved cell. The deformation of fluid in this case involves the effect of capillary force under constraints imposed by the three dimensional shapes of engraved cells. Our experimental photographs of silicone oil, shown in Figure 2.5, show a filling process at low capillary number. Figure 2.5a shows that the moving contact line moves from left to right uniformly, but when it reaches the edges of an engraved cell, it pins at the edge. As the contact line on the top surface advances to the right, the contact angle at the cell edges increases and eventually fluid advances into and fills the cell. After that, the moving contact line is released back to a straight line, i.e. the minimum surface energy. The fine granularity snapshots of the filling process shown in Figure 2.5b suggest that fluid enters the cell from the first edge of the cell where the moving contact line is pinned. After that, the capillary force rapidly moves the liquid interface along internal corners between the bottom and side walls, resulting in advancing tips of fluid on both side walls. Then, the tips touch the end of the cell and expel the air out of the cell.

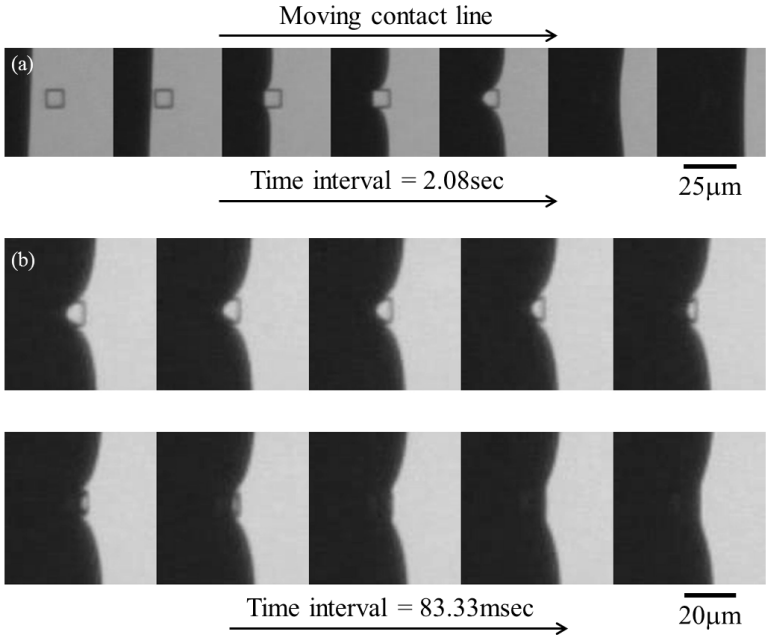

Figure 2.5 Filling process of silicone oil with viscosity of 29,040 mPa·s; (a) Time lapsed photographs showing a moving contact line passing a 7.5 μm cell. The contact line pins at the edge of the cell and eventually fluid fills the cell between frame 5 and 6; (b) Slow time lapsed photograph showing a filling process between frame 5 and frame 6 in (a).

Figure 2.6 shows the same filling process as in Figure 2.5, but for PVP solution. To establish the likelihood of occurrence of this filling process, we consider the relationship between a

characteristic velocity[21] $V^* = \gamma/\eta$ controlling the dynamics of wetting and the printing speed U. If V^* is much larger than U, then the fluid can advance and fill the engraved cell completely via the capillary behavior discussed. If V^* is much smaller than U, then the solid/liquid interface cannot move fast enough, predicting air entrapment. In the case where V^* is comparable to U, asymmetric filling should be observable. It is apparent, therefore, that it is convenient to describe the filling process as a function of the ratio of U to V^*, i.e. $\varphi_f \propto f\left(\frac{U}{V^*}\right)$. The ratio of U to V^*, in fact, turns out to be the Ca.

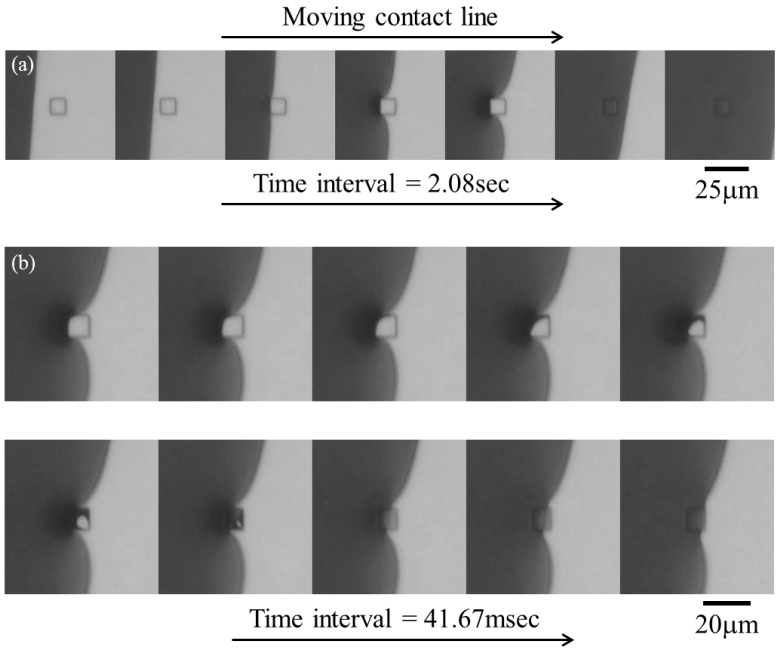

Figure 2.6 Filling process of 30 wt% PVP solution with η_∞~146 mPa·s; (a) Time lapsed photographs showing a moving contact line passing a 7.5 μm cell. The contact line pins at the edge of the cell and eventually fluid fills the cell between frame 5 and 6; (b) Slow time lapsed photograph showing a filling process between frame 5 and frame 6 in (a). Notice the time interval of filling process drops by half from Figure 2.5.

2.4.7 Wiping process

After filling, the excess ink needs to be removed by a doctor blade. When a doctor blade moves over an engraved cell, a new free surface is created. Ideally, this free surface is at the exact level of the printing plate surface, called the land area, and there is no fluid removed from the cell. However, experimentally, because the contact angle between the doctor blade and the ink is below 90° as shown in Table 2.1, a portion of the fluid is dragged out of the cell during wiping. Here we will discuss the origin of this drag-out volume.

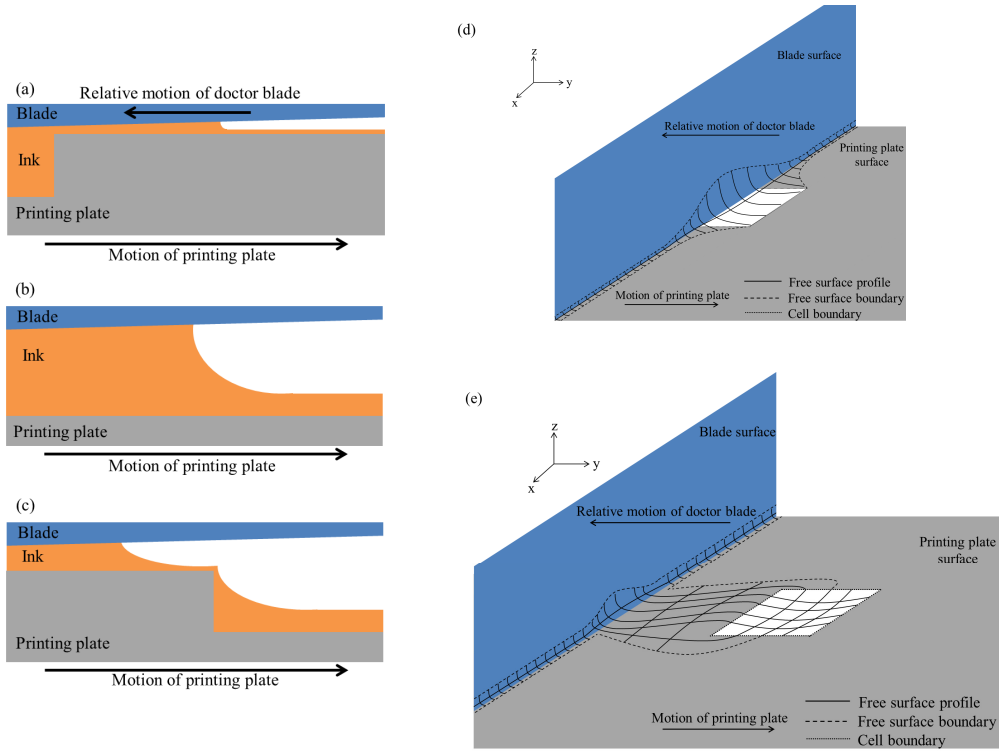

Figure 2.7 The geometry and meniscus of a cross section perpendicular to the contact line between the doctor blade and printing plate. The blade is stationary while the printing plate is moving from the left to the right in time lapsed drawing from (a) to (c) ; (a) the equilibrium meniscus on the non-patterned area and the contact line just reaches the cell opening, (b) the meniscus as the contact line moves over the middle of the cell opening. The curvature of meniscus is increased due to the increase in local gap between the doctor blade and printing plate, and (c) the meniscus as the end of cell opening passes the contact line. The curvature of meniscus reduces toward the equilibrium meniscus. (d) a three-dimensional schematic representation of the free surface as the doctor blade moves over the cell opening, and (e) as the doctor blade moves away from the cell opening. The free surface boundary is where the curvature is decreased to zero.

First, we consider the geometry during the wiping process as shown in Figure 2.1b. Since the tip radius of the doctor blade is much larger than the cell dimensions (this will necessarily be true for highly scaled gravure to ensure adequate doctor blade robustness while still allowing for fine feature patterning), the contact between the doctor blade and the printing plate can be approximated as a cylinder in contact with a flat surface having an engraved cell. The optical image and details of the doctor blades used in this study is in Chapter 3.

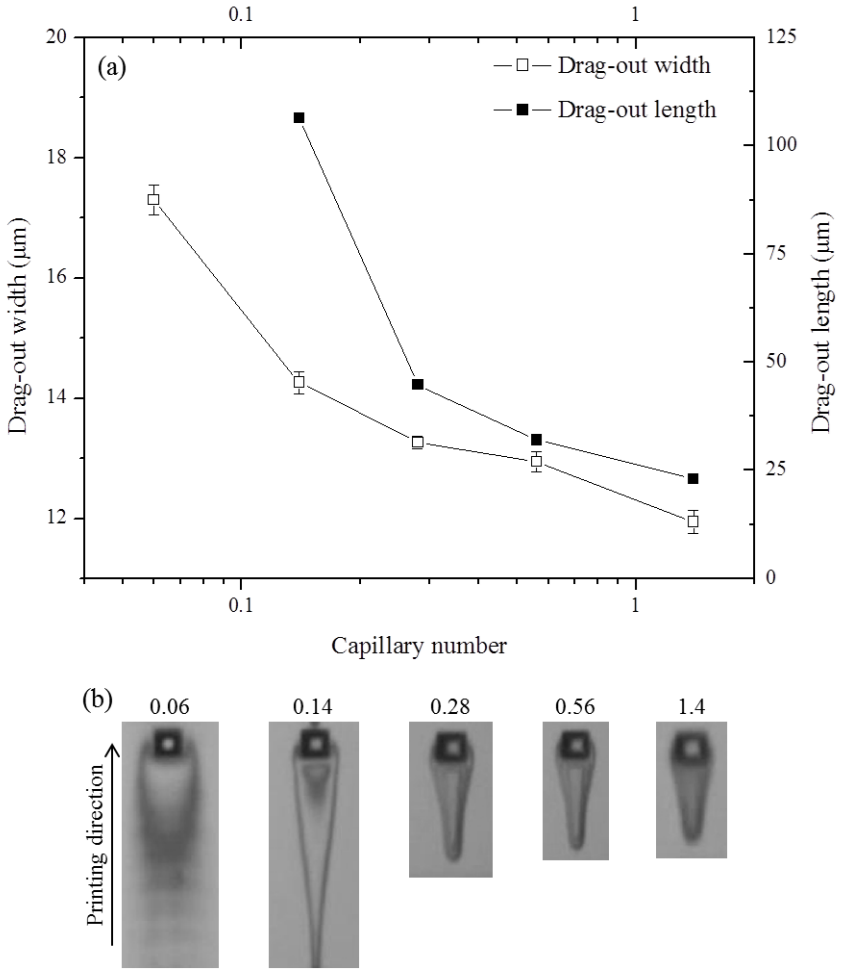

Figure 2.8 Wiping process of silicone oil with viscosity of 29,040 mPa·s; (a) dimension of drag-out tail as a function of Capillary number; (b) photographs of drag-out tail immediately after release from the doctor blade. The numbers on each image are associated capillary numbers. The cell width is 7.5 μm.

This geometry results in a narrow wedge along the contact line of the blade tip and the printing plate, as shown in Figure 2.7a. Based on the Landau-Levich equation, the curvature of the meniscus at the outlet of the channel between the doctor blade and printing plate in Figure 6a is determined by the gap between these two solid surfaces. The equilibrium curvature as the blade slides over the land area has a large negative curvature, because of the small gap. As the blade slides over the cell opening in Figure 2.7b, this curvature is reduced, because of the locally enlarged gap due to the cell depth. Finally, in Figure 2.7c at the end of the cell opening, the gap resumes its origin value and the meniscus is adjusted back toward the equilibrium curvature. Therefore there are two different meniscus curvatures while the blade moves over the cell opening. According to Laplace's theorem, where the hydrostatic pressure is equal to the product of the surface tension and the curvature of the free surface, the difference in the curvatures along the contact line of the blade tip and the printing plate generates a pressure gradient. The hydrostatic pressure on the cell opening is larger than the pressure on the land area. The pressure

gradient and wedge geometry generate a capillary flow of fluid from the engraved cell to the land area when the doctor blade contacts on the free surface of the cell opening. A schematic representation of the meniscus at this moment is showed in Figure 2.7d. As the doctor blade moves away from the cell opening as shown in Figure 2.7e, a fraction of the meniscus is deposited on the land area due to the no-slip boundary on the printing plate surface; this deposited ink forms a so-called "dragged tail" behind each cell opening. Because it is difficult for fluid to flow directly from the cell to the meniscus to compensate for the deposited volume, the meniscus shrinks, leading to a reduction in the size of the dragged tail as the doctor blade moves far away for the cell opening. Note that the thickness of the drag-out tail is on the order of 100 nm (shown in Figure 2.11, below), which indicates that there is a very small channel for fluid to flow directly from the cell. Eventually, a capillary break occurs and the dragged-out tail spreads out to minimize its surface energy.

The experimental results shown in Figure 2.8 capture this behavior. Figure 2.8a shows the dimensions of the drag-out tail immediately after releasing from the doctor blade. A blade angle of 55° was used for this experiment to meet the requirements of the optical working distance imposed by the optics. The Ca was calculated using the low shear rate viscosity of silicone oil, because the maximum wiping speed in this experiment was 1000 μm/sec, leading to a shear rate on the order of 200 s^{-1} using cell depth as a length scale. The viscosity of silicone oil at that shear rate is 29,040mPa·s as suggested by [22]. As Ca is reduced, i.e. the doctor blade moves more slowly over the cell opening, the drag-out tail grows considerably. The increase in width of the drag-out tail is consistent with it being created by the wetting of the wedge between the doctor blade and the land area. The increase in length can be explained by the enlarging of the meniscus, because the fluid has more time to flow from the cell to the tip and meniscus. This larger volume allows for the deposition of a longer tail on the land area. Figure 2.8b shows associated shapes of the drag-out tails from Figure 2.8a. The length of drag-out volume at Ca=0.06 was omitted because of an unclear boundary. Notice the drag-out tail boundary starts from the middle of the side walls of the engraved cell. When the doctor blade initially touches the free surface at the starting edge of the cell opening, the aforementioned meniscus does not exist yet. After a finite contacting time, the fluid flows along the wedge, creating the tips and meniscus. The boundary then expands in a perpendicular direction to the printing direction as depicted in Figure 2.8d. This boundary keeps extending until the end of the cell is reached and after that the tip and meniscus are shrunk due to the lost volume deposited as the tail, evidenced by the reducing width of the tail along the printing direction as illustrated in Figure 2.8e. Immediately after the drag-out tail disconnects from the doctor blade, the tail height is higher than the profile that equilibrium contact can support and the tail rapidly spreads out laterally to compensate for the extra height as shown in Figure 2.9. This is further evidence for the formation of a meniscus between the doctor blade and the engraved cell.

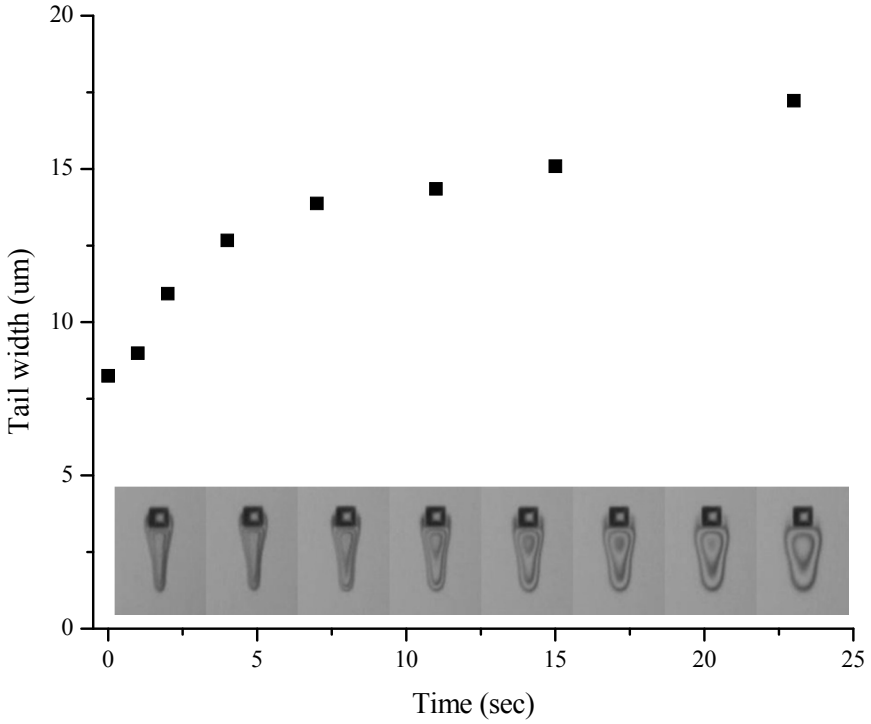

Figure 2.9 Spreading of drag-out volume as a function of time. Cell width was 7.5um and 30Pas silicone oil was used as ink.

To confirm that the drag-out mechanism is related to the wettability of doctor blade, drag-out tails produced by four different commercial doctor blades with different surface properties were characterized. The surface properties of doctor blades were characterized to determine advancing and receding contact angles. We found that the ratio of the drag-out tail to cell width reduced as the advancing and receding contact angles of the doctor blade increased, as shown in Figure 2.10. An increase in the advancing contact angle reduces the meniscus formed, and an increase in the receding contact angle accelerates the dewetting from the blade and reduces the drag-out tail. The effects of blade wettability on the drag-out tails supports the hypothesis that wiping is governed by the wettability between the doctor blade, printing plate and ink. Therefore, if a low surface energy blade is used, we postulate that the drag-out tails could be totally eliminated. We tested this hypothesis by wrapping Teflon tape on the doctor blade; the printing results showed that the drag-out tails were completely suppressed (see Figure 2.10). Unfortunately, low surface energy blades are not commercially available at this time, so this analysis therefore represents a motivation to drive future doctor blade development activities for printed electronics; currently, doctor blades used for printed electronics are simply those used in graphic arts applications.

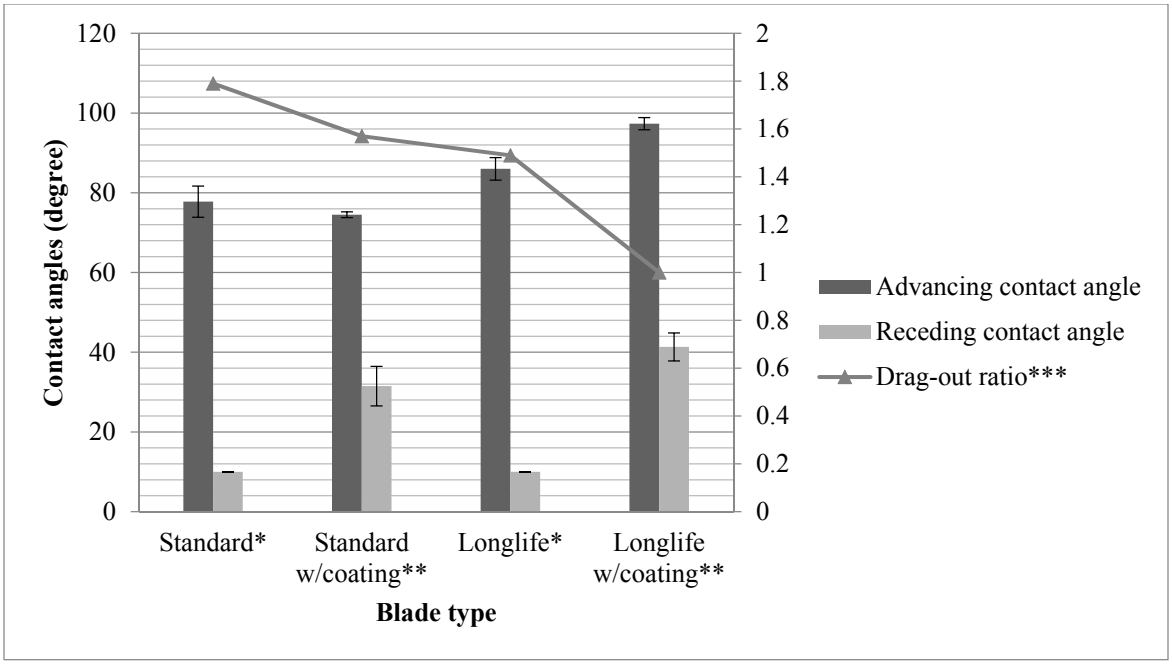

Figure 2.10 Effect of blade wettability of drag-out ratio. *The receding contact angle was too small to get an accurate measurement, but the fluid pinned on these two blades. Therefore we plotted the contact angle as 10 degrees to approximate the maximum receding contact angles of standard and longlife blades. **The hydrophobic coating was a self-assembly monolayer of 1H,1H,2H,2H-perfluorodecanethiol on evaporated gold layer. ***Drag-out ratio is defined as the ratio of the drag-out tail to cell width. The ratio was calculated from the pixels of images taken from a microscope.

Based on the experimental data and proposed wiping mechanism, the dependence of the dragged out volume on ink properties and printing conditions, i.e. the capillary number, can be established. Weislogel reported experimentally and numerically that the location of the tip of a fluid column under microgravity is a function of $(\gamma t/\eta)^{1/2}$ [23]. Therefore the length of the tips of the fluid and the meniscus volume can be expressed in terms of the characteristic velocity [21] V^* and the time available for the formation of the tips and meniscus. The length can be described as $\mathcal{L}_{max} \propto \left(\frac{\gamma t}{\mu}\right)^{\frac{1}{2}}$, where t is the total time that the doctor blade slides over the cell opening. The time parameter can be derived from the printing speed and cell length, because the meniscus grows only when the blade is over the cell opening. Therefore, the dragged out volume is a function of Ca and the cell length, since $\mathcal{L}_{max} \propto \left(\frac{\gamma l}{\mu U_p}\right)^{\frac{1}{2}} = \left(\frac{l}{Ca}\right)^{\frac{1}{2}}$, where l is the cell length along the printing direction. As we hold the cell geometry and wettability of the printing plate and doctor blade as constants, Ca is the main factor affecting $\mathcal{L}_{max}$. As the $\mathcal{L}_{max}$ defines the volume of the meniscus, the drag-out volume is a function of Ca.

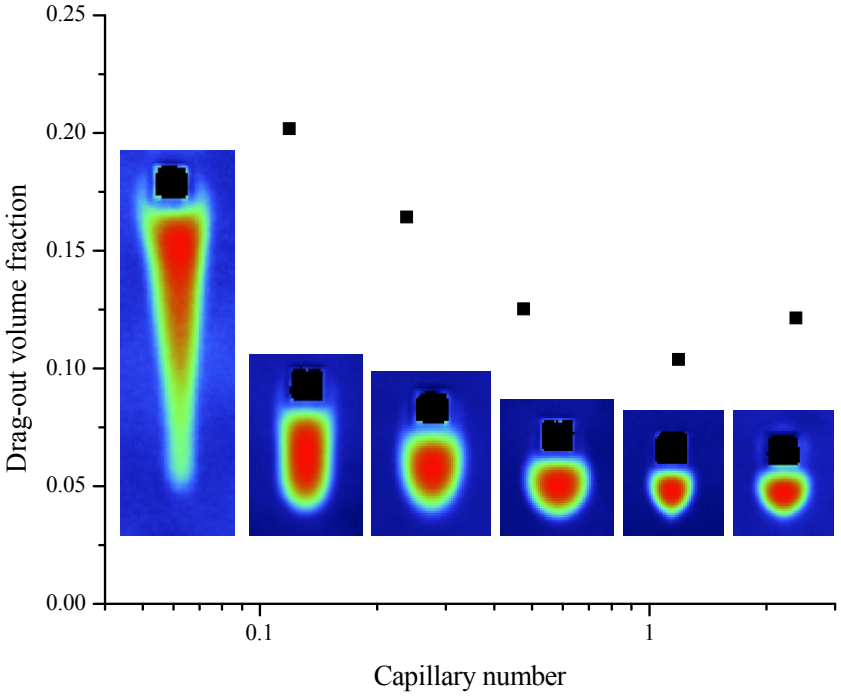

Figure 2.11 Drag-out volume as a function of Capillary number of non-Newtonian fluid (27.5 wt% PVP solution with η_∞~80 mPa·s). Inset pictures show the shape of the drag-out features at different capillary numbers. The pictures were taken by interferometry and the color is associated with the height of the dry film, varying from blue to red. The black squares in the pictures are engraved cells, where the data is not valid due to limitations of the interferometric measurement apparatus due to a rapid change in height. The cell width is 7.5 μm. The drag-out volume fraction at the lowest Ca is omitted, because of uncertainty in defining a boundary for extracting drag-out volume.

To verify this simple relationship between drag-out volume V_d and Ca, an independent wiping experiment was performed using 80mPa-s PVP solution, by varying the printing speed. As shown in Figure 2.11, the drag-out volume fraction φ_d depends strongly on Ca. The φ_d decreases almost linearly as Ca increases and then saturates at high Ca, as predicted by the expected relationship discussed above. The saturation at high Ca is due to elastohydrodynamic effects. The drag-out shapes are very similar to Figure 2.8 except for shorter tails at high Ca; the reasons for this deviation are not clear at this time. It is interesting to note that significant volume was dragged out from the engraved cell. The V_d approaches 25 percent of cell volumes at low Ca. This V_d not only deteriorates the pattern fidelity, but also potentially reduces the transferring fraction due to the increased capillary bridge length between the engraved cell and the substrate. To summarize, as the Ca rises, the dragged volume fraction φ_d reduces and the remaining volume fraction $\varphi_w = 1 - \varphi_d$ increases. Obviously, to minimize residue due to dragging out, it is highly desirable to minimize φ_d.

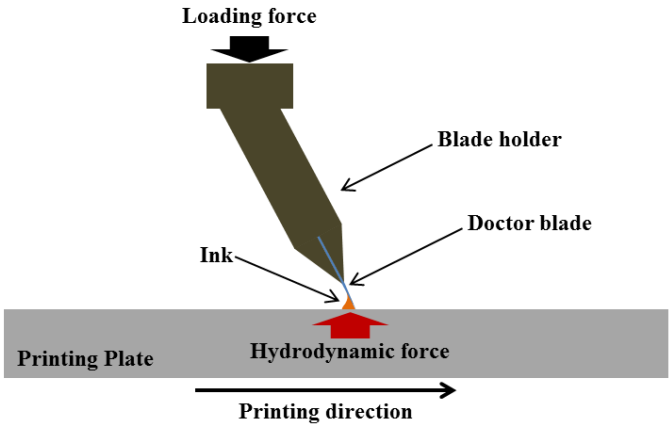

Figure 2.12 Schematic of doctor blade set up used in this work. The gap between the tip of the doctor blade and printing plate is defined by balancing the loading force and hydrodynamic force.

While the drag-out problem is mitigated at high Ca, i.e. fast printing speed and higher ink viscosity, as demonstrated in Figure 2.8 and Figure 2.11, the residue film volume fraction φ_l increases as a function of Ca and compromises the pattern fidelity by adding background noise. Recall that the residue film is defined as a lubrication film between the doctor blade and the printing plate. Doctor blades are elastic and can be deflected if sufficient pressure is applied. As the printing plate drags fluid toward the gap between the doctor blade and the printing plate, the doctor blade rejects excess fluid backwards by developing a high pressure region near the leading edge of the gap. The balancing forces between the applied pressure on the doctor blade and the fluid pressure define a gap between the doctor blade and the printing plate as shown in Figure 2.12. This fluid is called a lubrication film, because it reduces the friction between the doctor blade and the printing plate. As the printing speed and/or viscosity increase, the fluid pressure increases, causing the gap size to be larger at constant applied pressure on the doctor blade. The increase in gap size allows more fluid to flow under the doctor blade. As a result of the deflection of the doctor blade, the lubrication film uniformly coats the printing plate and deteriorates the pattern fidelity due to additional background noise. The relationship between gap size and film thickness can be explained by a lubrication approximation and/or numerical simulation [24], [25]. To incorporate the residual film thickness into the printed volume fraction considerations, it is normalized by cell depth. This represents the degree of over filling onto an engraved cell due to this lubrication film (effectively, the doctor blade is held up some distance over the top surface of the cell by the lubrication film, thus "over-filling" the cell). The lubrication film is important only when the fluid pressure is much larger than the applied pressure on the doctor blade, i.e. in high Ca regimes. This lubrication film will be discussed further in Chapter 3.

We also investigate the possibility that the pressure difference between the front and back sides of the doctor blade can generate a flow and produce drag-out tails as an alternative mechanism. By using lubrication scaling, the calculated pressure difference is on the order of 1 GPa. The volume flow rate is estimated by using the Poiseuille law and the length scale of the flow is the

cell depth. The total volume flow as the blade slides over the engraved cells is calculated from the flow rate and total time (printing speed and cell length). We calculate the total volume to be smaller than 10 percent of the minimum drag-out volume we observed, suggesting that the drag-out is likely not caused by the aforementioned flow. Because the pressure difference depends on the product of printing speed and viscosity, the drag-out volume should increase as Ca increases, if the pressure difference is a driving force, which again is in contradiction to the aforementioned experimental observations. These behaviors therefore support our proposed mechanism indicating that the fluid is drained from the engraved cells due to the wettability of the doctor blade. Therefore, we conclude that the wettability is responsible for the drag-out mechanism. This explanation also agrees with experimental observations in conventional gravure printing [9]. This creates a challenge for scaling gravure printing because the drag-out mechanism will be more pronounced as the cell size is reduced, since the drag out volume will become a larger fraction of the overall cell volume, all else being unchanged.

2.4.8 Transferring process

Transferring is the last process in gravure printing we will discuss here. Dodd's previously reported simulation results describe the transferred ink fraction of gravure cells as a function of the Capillary number [6]. Although he did not consider the contacting and meniscus formation between the substrate and the printing plate prior to the departing step, his simulation is a good starting point for integrating the transferring process with our model to fully describe the gravure printing.

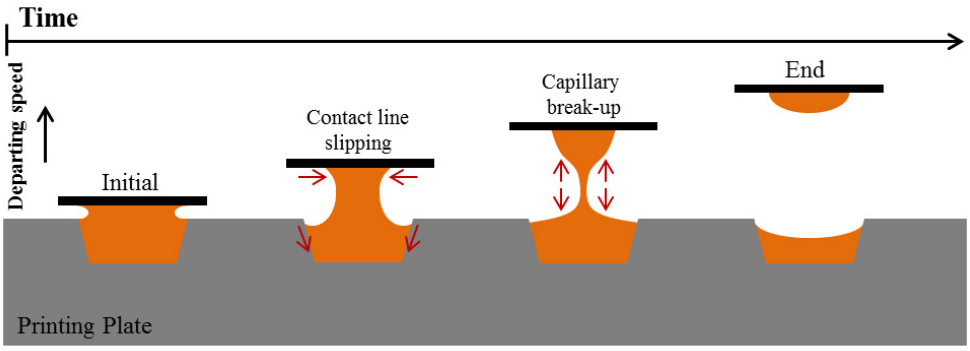

Figure 2.13 After Dodd [6], the transferring process is initialized as a capillary bridge between the substrate and the engraved cell. As the substrate departs, the contact lines slip toward the axisymmetric axis and the bridge breaks up due to a rising capillary pressure in the neck.

Figure 2.13 illustrates the sequence of steps described by Dodd. The simulations shows that as the substrate and engraved cell depart from each other, contact lines of the capillary bridge slip toward the axisymmetric axis and finally the bridge breaks up due to a rising capillary pressure in the neck. Thus, the transferring fraction is determined by two time scales; the slipping of contact lines and capillary break up. The velocities of contact lines slipping on the substrate and engraved cell surface are determined by the curvatures of the free surface near the solid surfaces. The curvature on the substrate is higher because the free surface deforms greatly to make a finite contact angle. In contrast, the curvature on the engraved cell has a smaller slope due to the slope

of the engraved cell. Because the curvature of the capillary bridge is not a constant, a capillary pressure gradient is developed and acts as a driving force on the contact lines toward the axisymmetric axis. The capillary pressure strongly depends on the surface tension force and dominates at low Ca. As a result of the higher curvature on the substrate, the contact line on the substrate slips faster than that on the engraved cell, causing a reduction in transferring fraction at low Ca. As Ca increases the viscous force dominates and the contact line slipping is suppressed, leading to increase in the transferring fraction. In short, the conclusion is that the transferring volume fraction improves as the Ca rises. This also agrees with other simulations [26] and experiments [27].

However, at high Ca the situation is more complicated than the stretching of a capillary bridge. As discuss earlier, at high Ca, the lubrication film thickness increases and this excess volume generates an over filled cell, which changes the initial filling level. The transferring fraction depends strongly on the initial filling level as discussed by Dodd [6]. The over-filled volume would increase transferring fraction effectively, but the contrast between printed features and background noise reduces. Therefore, this region should be avoided during operation.

2.4.9 Gravure printing characteristics

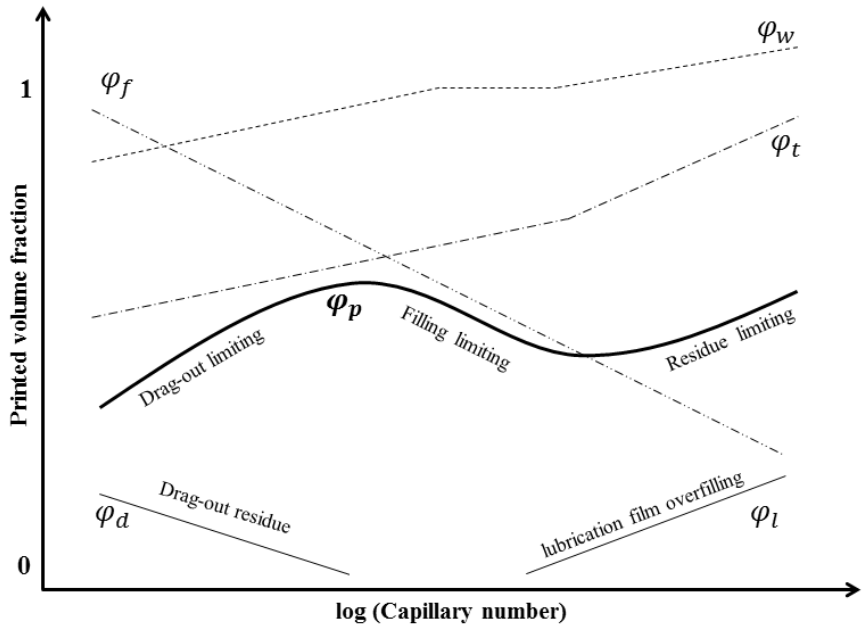

Figure 2.14 A diagram of printed volume fraction as a function of Capillary number on a semilog plot shows the characteristics of gravure printing and limiting mechanisms on three regions; drag-out limited at low Ca, filling limited at middle Ca and residue limited at high Ca.

After filling, wiping and transferring are defined as functions of Ca, the printed volume fraction can be constructed as a product of these functions. Figure 2.14 shows the simplest functions of filling φ_f, wiping φ_w, transferring φ_t, drag-out φ_d, and lubrication φ_l volume fraction. Note that the individual functions are expected to be nonlinear over a wide range of Ca. However, given the limited range of Ca relevant to gravure printing, we expect power law dependencies for the

individual terms, as discussed above, which will be roughly linear on a semilog plot. The printed volume fraction φ_p is shown over a relevant range of Ca for gravure printing. There are three limiting regions in this diagram. First, a drag-out-limited region exists at low Ca, where the drag-out volume is important. This drag-out volume deteriorates the pattern fidelity at the back of the cell and reduces the printed volume due to effective under-filling (recall that the drag out partially empties the cell). Second, a filling-limited region occurs at intermediate values of Ca, where air entrapment compromises the printed volume. Finally, a residue-limited region occurs at high Ca, where the lubrication film thickness overwhelms the printed features (recall that the lubrication film effectively over-fills the cell by adding additional ink over the top surface of the cell). The diagram indicates an optimized point of operation at the center, where the background noise from drag-out and the lubrication film are minimized.

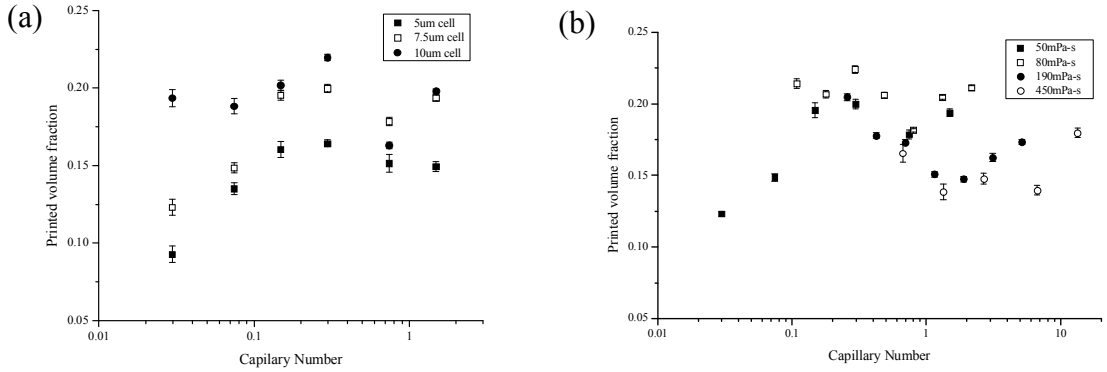

Figure 2.15 A diagram of experimentally measured printed volume fraction as a function of Capillary number for PVP inks; (a) the printed volume fraction at low-to-middle capillary number of three cell sizes, 10, 7.5 and 5 μm. The diagram shows a drag-out limited region; (b) the printed volume faction over a wide range of Capillary number. The diagram covers three regions; drag-out, filling, and residue limiting regions from low to high capillary number.

To verify the proposed model, printed volume fractions were experimentally recorded as a function of Ca and cell sizes. Figure 2.15a shows the printed volume fraction at low-to-intermediate capillary number for three cell sizes, 10, 7.5 and 5 μm using PVP solution. The concentration of polymer solution was 25 wt% to obtain a viscosity of 50 mPa·s. The viscosity was chosen so that Ca covered the range of interest. The maximum and minimum printing speeds are limited by the maximum speed of the driving motor and the evaporation of inks, respectively. The diagram shows that φ_p is increased as Ca increases. The fraction of printed dots (see Figure 2.16) that are fully formed also follows this trend, indicating that, as the drag-out volume increases, only a fraction of a droplet is printed. At most times, for defective patterns, the corners of a droplet are printed and a void is created at the center as shown in Figure 2.16. In this region, the drag-out volume creates a shadow tail and an incomplete printed dot, so it is called the drag-out-limited region. Figure 2.15b shows the printed volume fractions over a wide range of Ca. The viscosity was varied from 50, 80, 190, and 450 mPa·s with a limit set by the achievable printing speed. After the printed volume reaches the maximum value, it decreases as the Ca is

increases further; this is called the filling-limited region. At still higher Ca, the printed volume fraction increases again as a result of the lubrication film discussed above. There is a discrepancy in the onset of the residue-limiting region at high Ca. This might be caused by the elasticity of inks, which we have ignored, as discussed above. However, plotting φ_p against Ca allowed us to partially collapse the data and predict the optimized printing condition, where the contrast between the printed feature and residue was maximized. The raw data of φ_p plotted against the printing speed is shown in Figure 2.17.

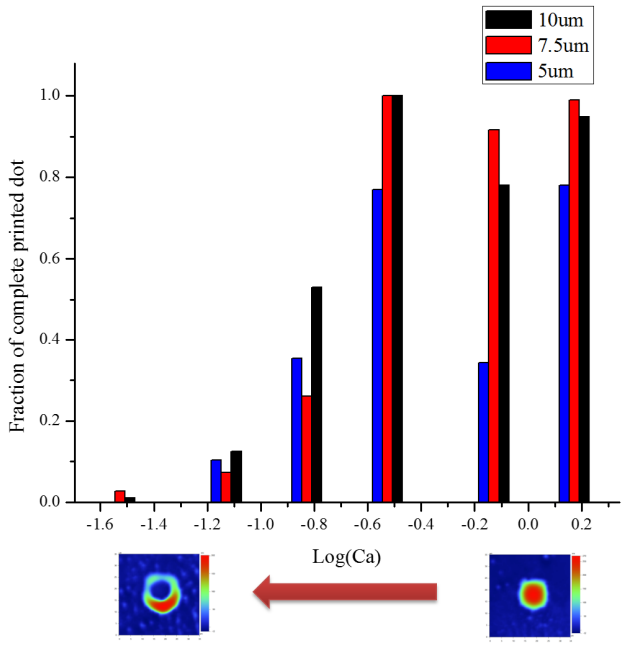

Figure 2.16 Fraction of printed dots that are complete as a function of Ca.

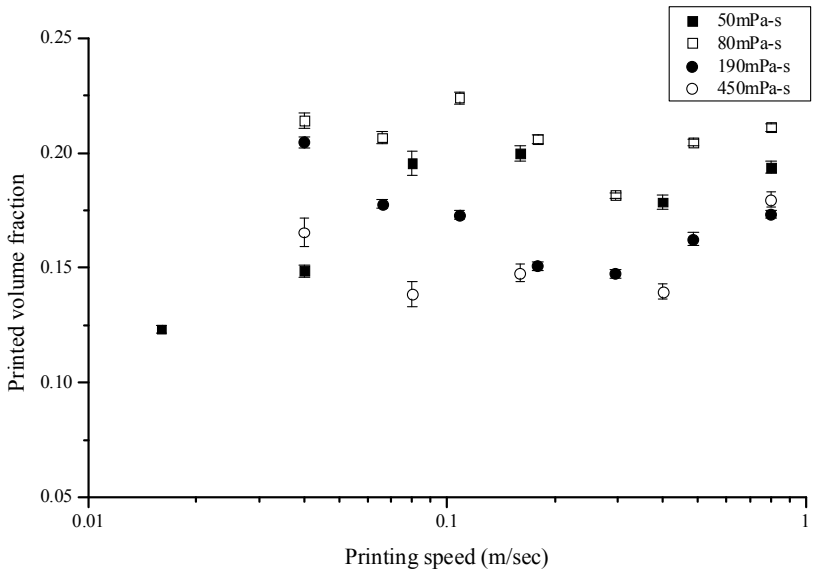

Figure 2.17 The raw data of printed volume fraction as a function of printing speed with ink viscosity as a parameter.

Finally, we printed high resolution lines at several printing speeds to demonstrate that the proposed model also describes the characteristics of gravure printing as the cell width is scaled to a record level of 2 μm. According to our model, the best operation point is between the drag-out and filling limiting regions. We locate this position by varying the printing speed and choosing a constant viscosity, covering the Ca of interest. The resulting printed lines are shown in Figure 2.18. The master pattern consists of an array of 4x4 dots and three groups of lines with decreasing line spacing. The dot array was located at the bottom left. The three groups of line patterns were positioned as perpendicular, 45° angle and parallel (from top left to bottom right) to printing direction in order to observe the effect of printing direction. The pattern morphology changes depending on the printing conditions. At low capillary number (Ca=0.22 and 0.47), the lines are intermittent and smudged due to drag-out. The effect of drag-out volume not only reduces the printed volume fraction, but also increases residues films behind the pattern, causing the smeared edges as indicated in the figure. As the capillary number increases, the printed lines are more uniform and well defined, but the minimum line spacing is limited by the drag-out features (which tend to bridge adjacent features). At the highest capillary number (Ca=4.46), the lubrication film was amplified, causing the minimum line spacing to be increased. By comparing Ca=1.00, 2.11 and 4.46, we can see that the minimum line spacing was achieved at Ca=2.11. At this condition, the residue films caused by the drag-out and lubrication mechanisms were minimized, leading to the best line spacing. Note that, at the finest resolutions, line edge imaging is limited by the resolution of the optical microscope used in this work. The optimized point (Ca=2.11) was shifted toward a higher capillary number. We postulate that this is caused by the fact that the drag-out mechanism is increasingly important as the cell is scaled down because the geometry of the doctor blade was held constant while the overall cell volume was

decreased. The optimized critical line width obtained at a capillary number of 2.11 was 2μm and the line spacing can be as small as 2 μm. These values are record values for gravure printing, to the best of our knowledge, and demonstrate that high-speed gravure scaling to single micron dimensions is indeed possible. The pattern is well preserved in both parallel and perpendicular directions. This confirms the ability of this technique to generate and deposit femtoliter patterns at high printing speed using high viscosity inks. Therefore, it is promising for high speed printing for future printed electronics applications.

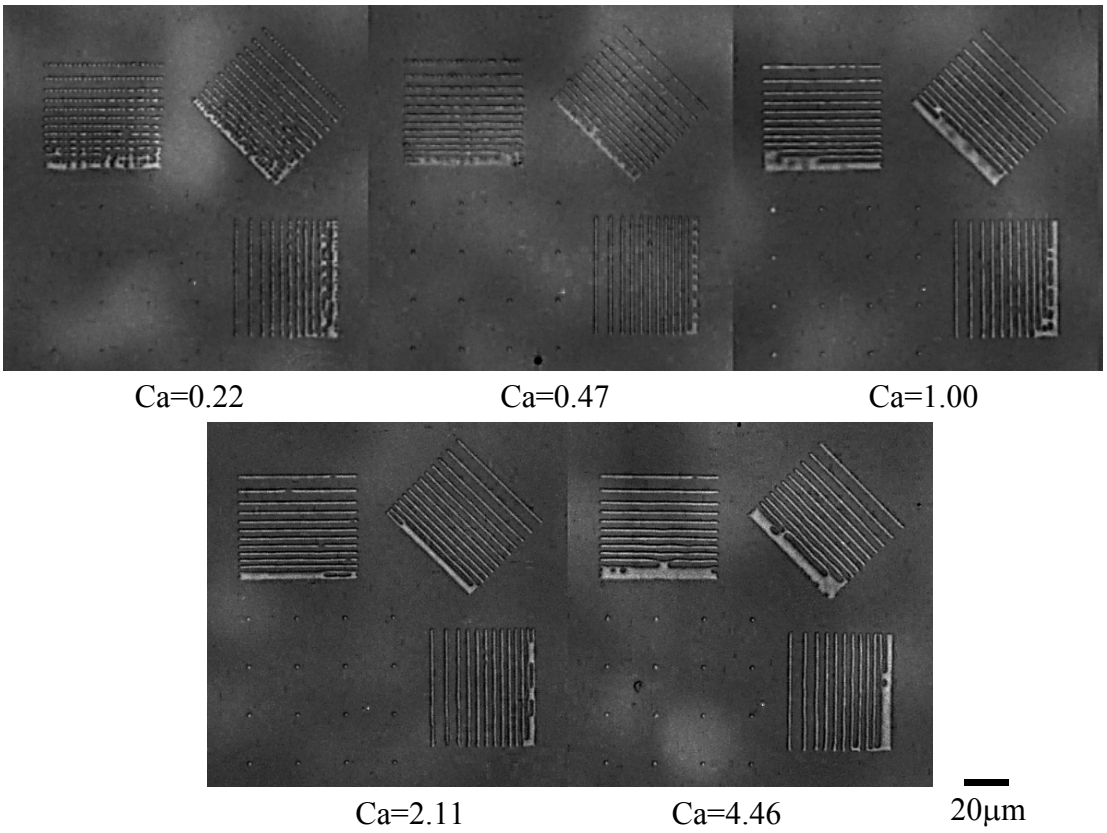

Figure 2.18 high resolution lines of 30 wt% PVP solutions with η_∞~146 mPa·s printed on PQA1 (a successor to Q65A from Dupont Teijin) by highly scaled inverse gravure printing with cell width and gap of 2 μm and 300 nm respectively. The printing direction is from the top to bottom. The optimized line width was ~2 μm obtained at Ca=2.11.

2.5 Conclusions

This chapter demonstrates the scalability of gravure printing by developing a highly scaled inverse direct gravure printer and using it to develop a detailed mechanistic understanding of the processes limiting gravure scaling. The printer produced printed features as small as 2 μm, and also enabled an investigation of the droplet formation mechanisms in highly scaled gravure printing. The fine printed features attest to the advantages of highly scaled gravure printing as followings; 1) compatibility with high viscosity inks, 2) high throughput, and 3) high resolution and pattern fidelity. Additionally, the observations of the printing mechanisms indicate the

various limiting processes associated with gravure printing. The major limiting mechanisms identified include residues from dragged-out ink and from a formed lubrication film. These residual films are concerns for electronics applications, since they deposit ink in undesired locations. By selecting a suitable capillary number, these residues can be suppressed, leading to optimized printing conditions. Under optimized operation, highly scaled gravure printing is an effective method for printing functional materials at high resolution and printing speed.

The simple mechanistic explanations proposed here represent a first step to understanding the complex mechanisms of gravure printing. This understanding allowed for realization of optimized line width and spacing as small as 2 μm. We find that the wettability of ink on the printer components and substrate, as well as the geometry of the engraved cells, is important to fully describe the flow behaviors. These individual processes will be studied in greater depth via further experiments and/or numerical simulations in subsequent chapters. And by using the capillary number as a linking parameter, individual studies can be related to for the realization of a comprehensive model of highly-scaled gravure printing, a critical necessity for printed electronics applications of the future.

2.6 References

[1] R. Kitsomboonloha, S. J. S. Morris, X. Rong, and V. Subramanian, "Femtoliter-scale patterning by high-speed, highly scaled inverse gravure printing.," *Langmuir*, vol. 28, no. 48, pp. 16711–23, Dec. 2012.

[2] D. B. Bogy and F. E. Talke, "Experimental and Theoretical Study of Wave Propagation Phenomena in Drop-on-Demand Ink Jet Devices," *IBM J. Res. Dev.*, vol. 28, no. 3, pp. 314–321, May 1984.

[3] L. W. Schwartz, "Numerical modeling of liquid withdrawal from gravure cavities in coating operations ; the effect of cell pattern," *J. Eng. Math.*, vol. 42, pp. 243–253, 2002.

[4] C. Powell, M. SAVAGE, and P. Gaskell, "Modelling the Meniscus Evacuation Problem in Direct Gravure Coating," *Chem. Eng. Res. Des.*, vol. 78, no. 1, pp. 61–67, Jan. 2000.

[5] K. Kim, T. Nam, and Y. Na, "A numerical study of the ink transfer process for roll-to-roll printing applications," *Proc. Inst. Mech. Eng. Part C J. Mech. Eng. Sci.*, vol. 226, no. 10, pp. 2496–2509, Jan. 2012.

[6] S. Dodds, M. D. S. Carvalho, and S. Kumar, "Stretching and slipping of liquid bridges near plates and cavities," *Phys. Fluids*, vol. 21, no. 9, p. 092103, 2009.

[7] S. Lee and Y. Na, "Analysis on the ink transfer mechanism in R2R application," *J. Mech. Sci. Technol.*, vol. 24, no. 1, pp. 293–296, Mar. 2010.

[8] X. Yin and S. KUMAR, "Flow visualization of the liquid emptying process in scaled-up gravure grooves and cells," *Chem. Eng. Sci.*, vol. 61, no. 4, pp. 1146–1156, Feb. 2006.

[9] Y. A. Bery, “Mechanism groverning gravure printing,” in *TAPPI Coating Conference*, 1985, pp. 149–159.

[10] D. Soltman and V. Subramanian, “Inkjet-printed line morphologies and temperature control of the coffee ring effect.,” *Langmuir*, vol. 24, no. 5, pp. 2224–31, Mar. 2008.

[11] H. Kang, D. Soltman, and V. Subramanian, “Hydrostatic optimization of inkjet-printed films.,” *Langmuir*, vol. 26, no. 13, pp. 11568–73, Jul. 2010.

[12] P. C. DUINEVELD, “The stability of ink-jet printed lines of liquid with zero receding contact angle on a homogeneous substrate,” *J. Fluid Mech.*, vol. 477, no. -1, pp. 175–200, Mar. 2003.

[13] J. Stringer and B. Derby, “Formation and stability of lines produced by inkjet printing.,” *Langmuir*, vol. 26, no. 12, pp. 10365–72, Jun. 2010.

[14] A. Darhuber, S. Troian, and S. Miller, “Morphology of liquid microstructures on chemically patterned surfaces,” *J. Appl.*, vol. 87, no. 11, p. 7768, 2000.

[15] V. Subramanian, P. C. Chang, J. B. Lee, S. E. Molesa, and S. K. Volkman, “Printed organic transistors for ultra-low-cost RFID applications,” *IEEE Trans. Components Packag. Technol.*, vol. 28, no. 4, pp. 742–747, 2005.

[16] H. Barnes and J. F. Hutton, *An introduction to rheology*, vol. 1. Elsevier Science B.V., 1989.

[17] A. W. Sisko, “The flow of lubricating greases,” *Ind. Eng. Chem.*, vol. 50, no. December, pp. 1789–1792, 1958.

[18] R. Hoffman, “A study of the advancing interface. I. Interface shape in liquid?gas systems,” *J. Colloid Interface Sci.*, vol. 50, no. 2, pp. 228–241, Feb. 1975.

[19] A. Carré and P. Woehl, “Spreading of silicone oils on glass in two geometries.,” *Langmuir*, vol. 22, no. 1, pp. 134–9, Jan. 2006.

[20] C. W. Hirt, J. M. Brethour, F. Science, S. Fe, I. C. Science, and T. Symposium, “Contact Lines on Rough Surfaces with Application to Air Entrainment,” in *11th International Coating Science and Technology Symposium*, 2002, vol. m, pp. 23–25.

[21] P. De Gennes, F. Brochard-Wyart, and D. Quere, *Capillarity and wetting phenomena: drops, bubbles, pearls, waves*. Springer, 2004.

[22] “Silicone viscosity vs. molecular weight and shear rate,” *Dow Corning*. .

[23] M. Weislogel, “Capillary flow in an interior corner,” *J. Fluid Mech.*, vol. 373, pp. 349–378, 1998.

[24] F. R. Pranckh and L. E. Scriven, “Elastohydrodynamics of blade coating,” *AIChE J.*, vol. 36, no. 4, pp. 587–597, Apr. 1990.

[25] I. Iliopoulos and L. E. Scriven, “A blade-coating study using a finite-element simulation,” *Phys. Fluids*, vol. 17, no. 12, p. 127101, 2005.

[26] J. M. Brethour and H. Benkreira, “Filling and Emptying of Gravure Cells – Experiment and CFD Comparison,” *11th Int. Coat. Sci. Technol. Symp.*, 2002.

[27] A. K. Sankaran and J. P. Rothstein, “Effect of viscoelasticity on liquid transfer during gravure printing,” *J. Nonnewton. Fluid Mech.*, vol. 175–176, no. March, pp. 64–75, May 2012.

Chapter 3 Lubrication-Related Residue as a Fundamental Process Scaling Limit

In gravure printing, excess ink is removed from a patterned plate or roll by wiping with a doctor blade, leaving a thin lubrication film in the non-patterned area. Reduction of this lubrication film is critical for gravure printing of electronics, since the resulting residue can lower device performance or even catastrophically impact circuit yield. This chapter will show experiments and quantitative analysis of lubrication films in a highly-scaled gravure printing process. The effects of ink viscosity, wiping speed, loading force, blade stiffness and blade angle on the lubrication film were investigated. According to the resulting data, the relevant lubrication regimes were examined to posit the lubrication regime associated with wiping during gravure printing, provide insight into the ultimate limits of residue reduction and furthermore, to provide process guidelines and design rules to achieve these limits. All results in this chapter are published in [1].

3.1 Introduction

The steps associated with highly-scaled gravure printing have been discussed in detail in the Chapter 1, but are summarized herein. Gravure printing makes use of hard (e.g., metallic) masters (typically cylinders, though plates may be used as well), with cells etched into them. Gravure printing starts with the filling of these engraved cells with ink; the excess ink is wiped off by a doctor blade, and the remaining ink is transferred onto the target substrate. For highly-scaled gravure printing, the wiping process is arguably the most important, since wiping affects both the quality of the resulting printed features and the cleanliness of the field regions. Generally, when printing fine features at the resolution limits of gravure, the master pattern for a line is a string of square cells, spaced evenly with interspersed small cell gaps. An illustration of cell gap and width definitions is provided in Figure 3.1a. As a result, the line resolution is at least partly defined by the minimum cell width. When the cell width is reduced to realize finer lines, the resulting printed line thickness also decreases as shown in Figure 3.1b, due to reduced overall volume of ink transferred. Figure 3.1b also shows that a reduction of the cell gaps to increase ink volume per unit length does not increase the line thickness. Fortunately, the fact that line thickness reduces as line width is reduced does not appear to be a fundamental limitation; we have shown that line thicknesses as thin as 50 nm can be conductive enough for many printed electronics applications [2]. An AFM image of a sintered silver nanoparticle printed line on a plastic substrate is shown in Figure 3.1b; in particular, it is important to observe the nanoparticle scum in the field regions on either side of the printed line. This residue occurs not only in printed nanoparticle films, but also in printed organic layers, and is of great concern for printed electronics applications [3]. For example, increased surface roughness is known to degrade semiconductor device performance through degradation in mobility [4]; increased roughness is also a likely source of increased defects in dielectric films, and furthermore, degrades visual quality of the substrate through generation of a haze, making it problematic for display applications. In order to enable the realization of high-performance, high-quality gravure-printed electronics, therefore, these residues must be reduced.

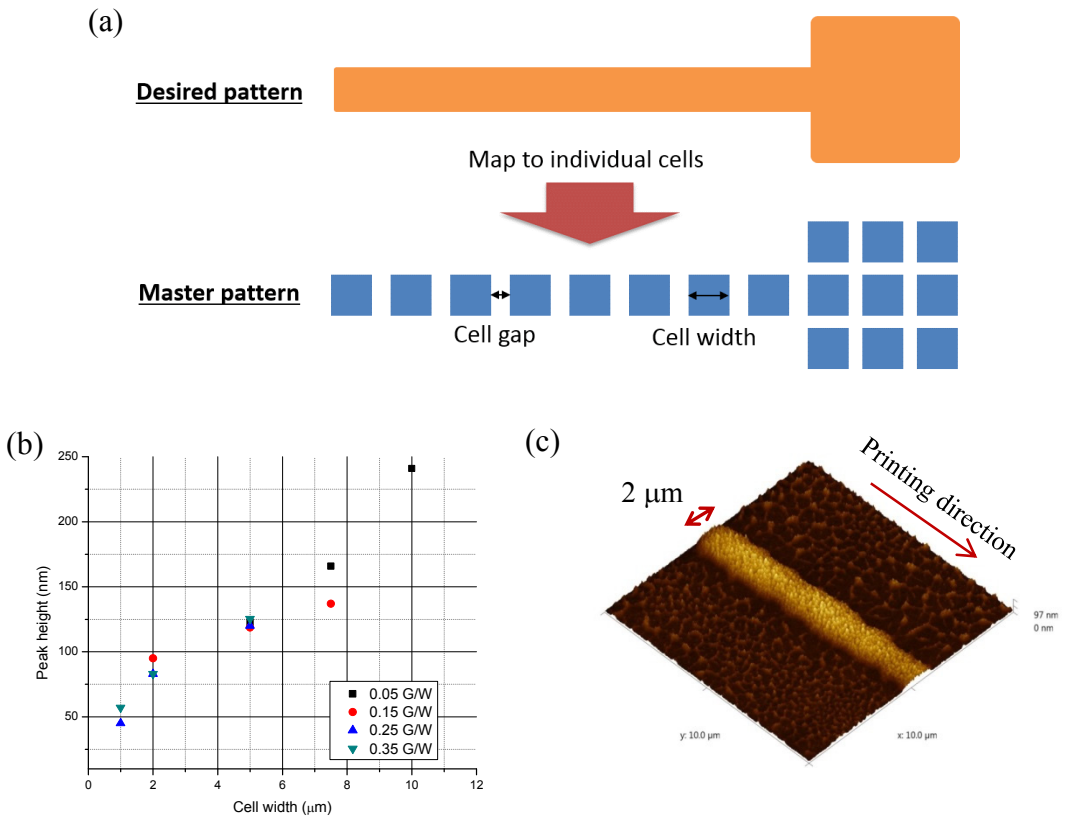

Figure 3.1 (a) an example of master pattern of high resolution gravure. Cell gap and width are defined as a spacing between cells and width of square cells, respectively. (b) printed silver nanoparticle line heights as a function of engraved cell widths. G/W is the ratio of cell gap to width. (c) An AFM image of a printed silver nanoparticle line after sintering. The line width is 2 μm; note the scum formed by residues on either side of the line in the non-patterned areas.

We have previously shown that there are two classes of residues produced in the wiping process [5]. The first is a cell-dependent residue, called dragged-out residue, and the second is a uniform residue film, called a lubrication film. The dragged-out residue is produced by capillary removal of ink from the cells by the passing doctor blade. As the blade passes a cell opening, capillary flows along narrow wedges, which forms along the contact line between the blade tip and the printing plate, drain ink out of the cell. Since the driving force is surface tension force, working at high Capillary number or by using doctor blades with reduced wetting can reduce dragged-out residue, as discussed in our previous work. The lubrication film, on the other hand, is created as the doctor blade slides over the plate/roll surface; the wet lubrication film is formed due to the interaction between the ink, the blade, and the plate/roll surface, and acts as a lubricant to reduce the friction between these two surfaces. The lubrication film is therefore critically important since it represents a fundamental process scalability limit for gravure printing; as feature sizes are reduced, the printed pattern thickness approaches that of the lubrication residue, degrading the overall pattern quality through formation of scum. Surprisingly, despite the importance of

residues in gravure printing, there are no reports on the details of this phenomenon; on the other hand, the other important processes in gravure have been studied, namely, the transferring process as described by Yin and Kumar [6], and by Sankaran and Rothstein [7], and the well filling and dragging out processes as described in our previous work [5]. Hanumanthu reported experimental results coupled with theoretical analysis using lubrication equations on the effect of blade geometry on coating thickness [8]. The results indicates that during early stages of doctor blade wear, the coating thickness varies significantly. Therefore, the geometry of the doctor blade is very important in controlling the lubrication residue film and printing quality. However, the actual residue film thicknesses and the reduction of residues were not studied in that work, since it is not very critical for coating films.

In this chapter, we describe detailed experimental studies on the lubrication residues in gravure printing, including extensive experimentally obtained statistics on residue films and the associated lubrication mechanisms. By comparing to lubrication-related models in the literature, we posit the lubrication regime in which wiping during gravure printing operates and provide insight into the associated underlying mechanisms. This comprehensive view of lubrication residues thus identifies a fundamental limit to scaling of gravure printing for printed electronics applications.

3.2 Measurement of residue films

Measurement of residue films is challenging since a large number of measurements are needed to ensure statistically meaningful data. Typical residue films are only several nanometer thick, complicating the choice of measurement technique.There are several methods to measure very thin films [9]. Optical interferometry is most attractive in terms of measurement accuracy and speed. In order to measure film thickness below a quarter wavelength using optical interferometry, a spacer layer is required [10]. The spacer acts as a preset thickness so that interference is ensured. Modern interferometers allow for measurements of films as thin as 1nm using this method [11]. However, installing a doctor blade into a conventional interferometric measurement system is challenging. Therefore, we adapted a very established optical thin film measurement technique commonly used in microfabrication, i.e. reflectometry. Reflectometry also depends on interference, so a spacer was used in this work; the thermal oxide provided this spacer. Since the oxide thickness is somewhat non-uniform across the plate, selected locations were pre-measured to ensure accuracy of residue film thickness measurement. The resulting values were compared to AFM measurements to verify accuracy and consistency. Figure 3.2 shows the thicknesses measured by AFM and spatially calibrated reflectometry. The thicknesses were very well correlated. The reflectometer used was a Nanometrics 210 XP from Nanometrics Inc. The measurement spot was 30 μm using a 5x objective.

A linear regression of AFM and optical thicknesses is also given Figure 3.2. The calibrated slope can be explained by the difference in reflective index. The reflective index of silicon dioxide used was 1.456 and the reflective index of PVP is 1.6, as reported by Sigma Alridch. The ratio of the different reflective indices is 0.91, which is very close to the calibrated slope of 0.9057. The

constant offset of this thickness can be explained by the fact that the step profile was created for the AFM measurement by mechanical scratching, possibly abrading the underlying oxide film.

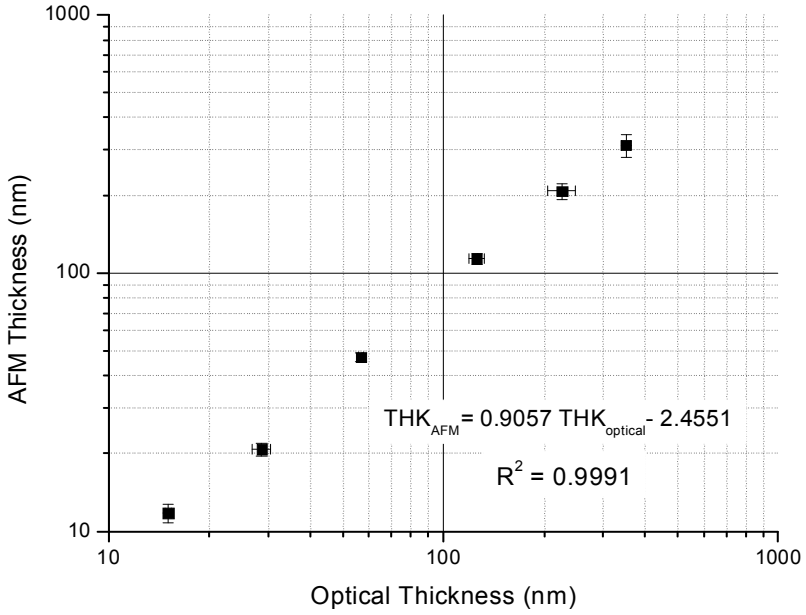

Figure 3.2 The relationship between AFM thicknesses to optical thickness

3.3 Experimental section

To enable detailed experimental study of the lubrication residues, we have developed a highly controlled experimental framework following our previously reported inverse direct gravure system. In this system, the gravure master is simulated using a patterned silicon wafer with plasma etched wells; this offers the advantage of providing excellent control of cell dimensions. A doctor blade is placed on the printing plate with a controlled loading force, and ink is dispensed at the contact point. The plate is then moved at a controlled speed to enable precise simulation of the wiping process. The lubrication residue on the master is then dried, and the dry film thickness is measured using optical reflectometry as described previously.

A computer-aided design (CAD) model of the printer used is illustrated in Figure 3.3a. The printer consists of a printing plate, motorized linear stage, doctor blade and pneumatic actuators. The printer can operate with a loading force up to 117 N, printing speed up to 1.5 m/s and blade angle of 50° to 80°. These parameters are based on values typical for standard lab-scale gravure printers. The loading force is a vertical force exerted on the blade holder as shown in Figure 3.3b and is controlled by pressurizing pneumatic actuators. These actuators push the doctor blade downward as guided by linear stages. Because the blade can slide down freely, this ensures that the blade makes a good physical contact to the printing plate at all times. The blade angle (defined as the installed angle between the doctor blade in the holder and the printing plate) is adjusted by a rotating stage at the blade holder axis; the default angle was 70°. The doctor blade

was carefully installed so that the total length of the doctor blade body and tip protruding from the blade holder was 4 mm.

The printing plates were silicon wafers with a 1.6 μm thick thermal oxide layer. The printing plates were patterned by optical lithography using a stepper (ASML 5500/300) and dry etching (Rainbow 4520). All measurements of lubrication film thickness were made in regions far enough away from patterned cells to ensure no contribution from drag-out residues.

The doctor blade is a core component in the wiping process. It strongly impacts the wiping residue and the overall printing quality. In this study, lamella blades, also known as standard blades supplied by Max Daetwyler Corp, were used because of their widely usage in industrial gravure applications. The doctor blades used in this work had a tip diameter of 50 μm and a body thickness of 150 μm as shown in Figure 3.3c, unless otherwise stated. The thicker part of the doctor blade is called the body and the thinner part is called the tip. Figure 3.3d shows detailed cross sections of the tips; these appear to be smooth in Figure 3.3d, but interferometry showed the RMS roughness at the tip to be 0.6 μm with a wavelength ranging from 1 to 10 μm. The doctor blades used here are made of carbon steel to provide durability and strength.

The effects of ink viscosity and wiping speed on the lubrication film were characterized. In this study, Poly (4-vinylphenol) (PVP) [M_w ~11000 g/mol, part number 436216 from Sigma-Aldrich] in a propylene glycol monomethyl ether acetate (PGMEA) was used as the model ink, since this is an extremely popular dielectric ink in printed electronics [12] . The ink viscosity was adjusted by varying the concentration of PVP in PGMEA. The viscosity as a function of PVP concentration and shear rate is available in [5]. This model ink shows shear thinning behavior, but does not exhibit a yield stress. At a shear rate higher than 1E4 1/s, the viscosities becomes approximately constant, depending on polymer concentration. The wiping speed was varied from 0.01 to 1 m/s.

The effects of the loading force, blade stiffness and blade angle on the lubrication film were also investigated. Before conducting the wiping experiments, each printing plate was cleaned in piranha solution for at least 10 min, followed by rinsing with DI water and drying. Then, the reference oxide thickness was measured in known locations distributed across the plate using optical reflectometry. After performing a wiping experiment, the total thickness of the dried lubrication film and thermal oxide was measured in these same locations using the same technique. The dried film thickness was calculated by subtracting the thickness of the oxide reference at a given location from the total thickness at the same location and then the wet film thickness was calculated based on the known polymer concentration. The total wiping distance is 150 mm, and only regions under uniform substrate motion were used in this analysis; regions associated with stage acceleration at the beginning of a print were avoided herein.

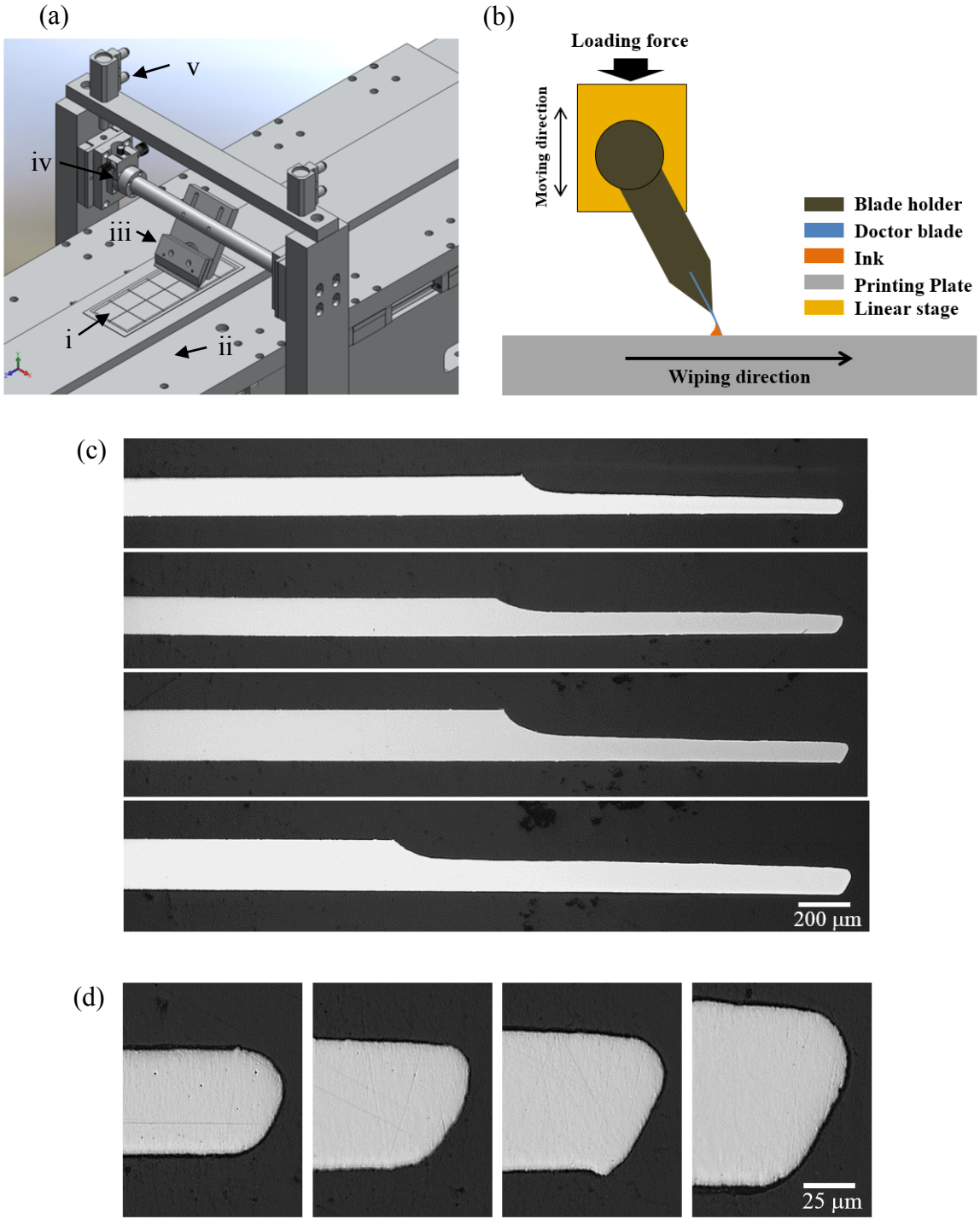

Figure 3.3 (a) CAD model of the printer (i) printing plate, (ii) motorized linear stage, (iii) doctor blade, (iv) rotating stage, and (v) pneumatic actuators, (b) a schematic of the wiping experiment. (c) optical micrograph of doctor blades in cross section; from top to bottom, the tip/body

thicknesses are 50/150, 75/150, 75/200 and 95/200 μm, (d) zoom-in at the tip of the doctor blades to show the detailed tip curvature.

To account for the effects of residue film non-uniformity, we measured 28 locations over a 40×40 mm^2 area on the printing plates and used the median as the representative thickness of the lubrication film. We also studied the distribution of film thickness using Weibull plots. The cumulative distribution function is calculated using the median rank as suggested by Dodson [13].

Table 3.1 Default experimental parameters

Physical parameters	
Printing speed	0.01 – 1.00 m/s
Viscosity	14-1497 mPa·s
Polymer concentration	20-40 wt%
Blade tip radius	25 μm
Blade body thickness	150 μm
Blade tip length	1300 μm
Blade length protruded from the blade holder	4000 μm
Blade width	50 mm
Blade angle	70°
RMS roughness	0.614 μm
Printing plate length	150 mm
Printing plate width	40 mm

3.4 Notations

Table 3.2 Notation of parameters

A	Hamaker constant [J]
E_r	Reduced elastic modulus [GPa] $\frac{\pi}{E_r} = \frac{1-v_1^2}{E_1} + \frac{1-v_2^2}{E_2}$
E'	$\frac{1}{E'} = \frac{1}{2}[\frac{1-v_1^2}{E_2} + \frac{1-v_2^2}{E_2}]$
F	Loading force [N]
G^*	Material parameter $G^* = \alpha E'$
g_1	Viscosity parameter
g_3	Elasticity parameter

$\bar{h}$	Film parameter
h	Lubrication film thickness [m]
h_{exp}	Measured lubrication film thickness [m]
h_c	Center lubricant film thickness [m]
h_m	Minimum lubricant film thickness [m]
H	Dimensionless film thickness $H = \frac{h_m}{R}$
L	Contact width [m]
R	Tip radius [m]
U	Speed [m/s]
U^*[14]	Speed parameter $U^* = \frac{\eta_0 U}{E'R}$
w_L	Normal load intensity [N/m] $w_L = \frac{F}{L}$
W_L^*	Loading parameter $W_L{}^* = \frac{F}{LE'R}$
α	Pressure-viscosity coefficient [1/GPa]
η_0	Entry viscosity [Pa·s]
ν	Poisson ratio
Π	Disjoining pressure [Pa]
CDF	Cumulative distribution function

3.5 Experimental observations

We note that a great deal of spatial variation in residue film thickness was observed in the direction perpendicular to the wiping motion; on the other hand, there is little variation parallel to the doctor blade motion, since we maintain well-controlled doctor blade pressure and speed. The cross-substrate variation is expected, given the microstructure of the doctor blade. Figure 3.4a shows a pristine doctor blade. The doctor blade has significant transverse roughness and there are defects along the length. The defects are both valleys and peaks. Figure 3.4b shows the detailed microstructure of one of the defects; these defects are formed during doctor blade manufacturing. The defect in this picture has a lateral size of ~20 μm. The defects can change the contact distance between the doctor blade and the printing plate, leading to a variation in film thickness. It is worth mentioning that the lateral width of lubrication films caused by these defects is much wider that the width of the defects, because of the lateral capillary flows, similar to the drag-out effect in [5]. Figure 3.4c shows a used doctor blade. There are slight signs of wearing in the wiping direction.

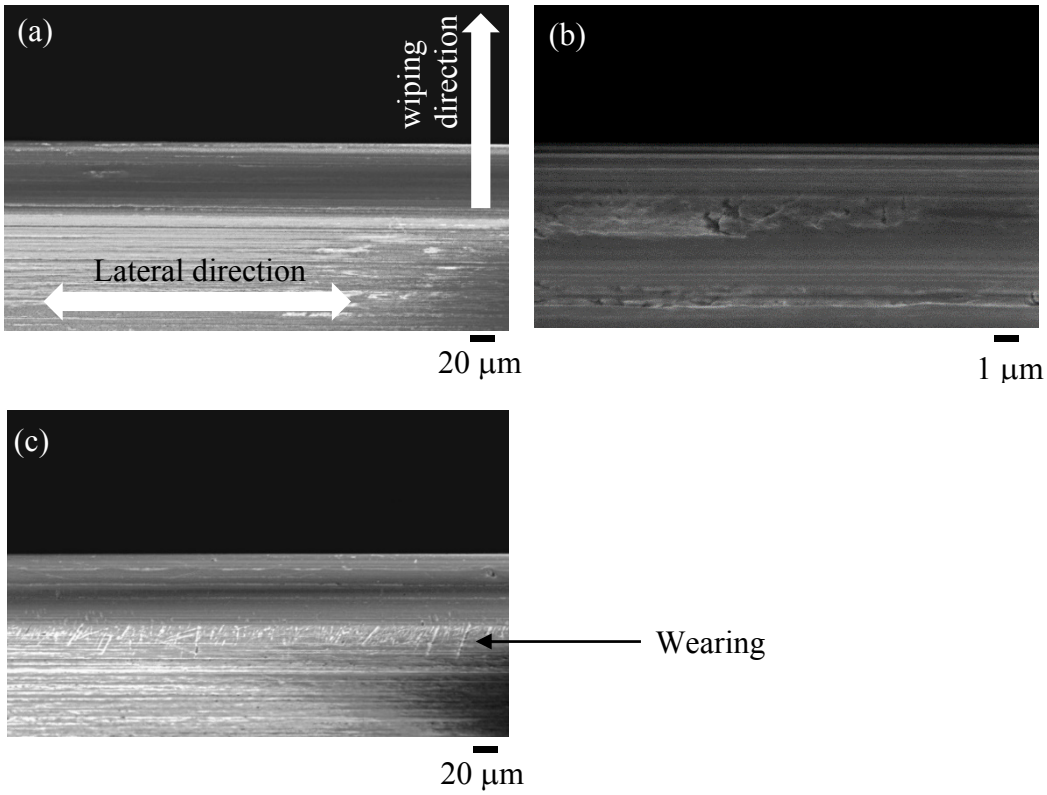

Figure 3.4 (a) a SEM micrograph of a pristine doctor blade, (b) zoom-in picture of one of the defects, and (c) the scratches in the doctor blade due to the blade wearing at the contact area after seven wiping experiments.

To combine the effects of viscosity and speed, U* is used, as suggested by Dowson [14]. Figure 3.5 shows Weibull plots of residue film thickness as a function of U*. We explain the large variation based on the doctor blade variation as above. In spite of the wearing shown in Figure 3.4, there was no significant effect on the distribution of film thickness for the higher viscosity measurements (Figure 3.5a to Figure 3.5b). On Figure 3.5e, there is crossover observed between U*=7.40E-9 and 3.53E-9. The reason for this is currently unconfirmed, but could be an effect of the wearing. It is interesting to point out that the distribution of film thicknesses appears to depend on U*. When U* is high, the distributions are generally narrow and can be fitted to normal distributions. However, at the lower limits of U*, in which the lubrication film is below 10 nm, the distributions are generally very steep when films are thin, but show significant spread for thicker films. This suggests that as U* is reduced, film thicknesses reduce and approach the thinnest film thickness values. This minimum film thickness weakly depends on U*. The thicker outliers are likely due to the aforementioned defects on the doctor blades. Note that the distribution of U*=1.94E-8 in Figure 3.5d is wider than that of U*=3.21E-9 in Figure 3.5c, in spite of the fact that U* is higher. The reasons for this are currently unclear.

Figure 3.5f shows the median of the thickness of the lubrication film as a function of U*. At high U* the thickness of lubrication film rapidly increases. At lower U* where the film thickness is

below 10 nm the film thickness departs from the trend line and appears to become largely independent of U*. A regression fit to a power law of film thickness with U*≥1E-8 is superimposed to provide a visualization of the general trend. The extracted exponent was 0.7465. Figure 3.5f also supports the use of the U*, since the data across multiple conditions collapses onto a single trend line, consistent with Dowson.

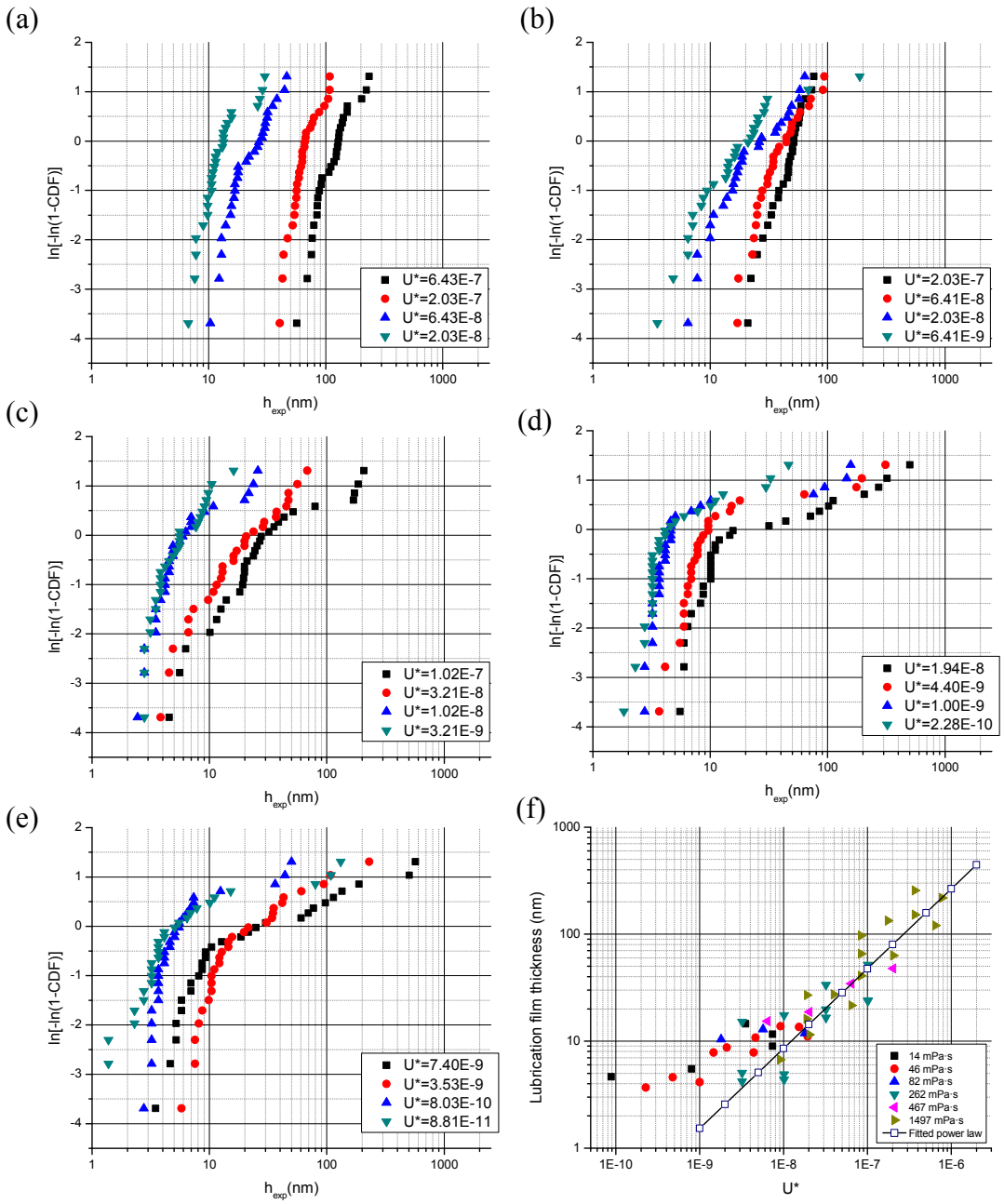

Figure 3.5 Weibull plots of the lubrication film thickness as a function of a product of viscosity and speed. Ink viscosities range from (a) to (e) 1497, 469, 262, 46 and 14 mPa·s, which correspond to PVP concentration of 40, 35, 32.5, 25 and 20 wt%. ln[-ln(1-CDF)] is a Weibull function, where CDF is a cumulative distribution of the lubrication film thickness. (f) The

median of lubrication film thickness as a function of the dimensionless speed parameter, U*. The viscosity was varied by altering the PVP concentration.

Next, the effects of loading force are shown in Figure 3.6. The loading force experiments were performed only in the range 1E-9≤ U*≤1E-7, where the lubrication films are thin and reasonable printed results can be produced. Figure 3.6b clearly illustrates that the film thickness reduces rapidly as loading force is initially increased, but ultimately becomes a weak function of the same at high loading force values. The dependence of the lubrication film thickness on U* also slightly reduces as the loading force is increased, as shown in Figure 3.6a.

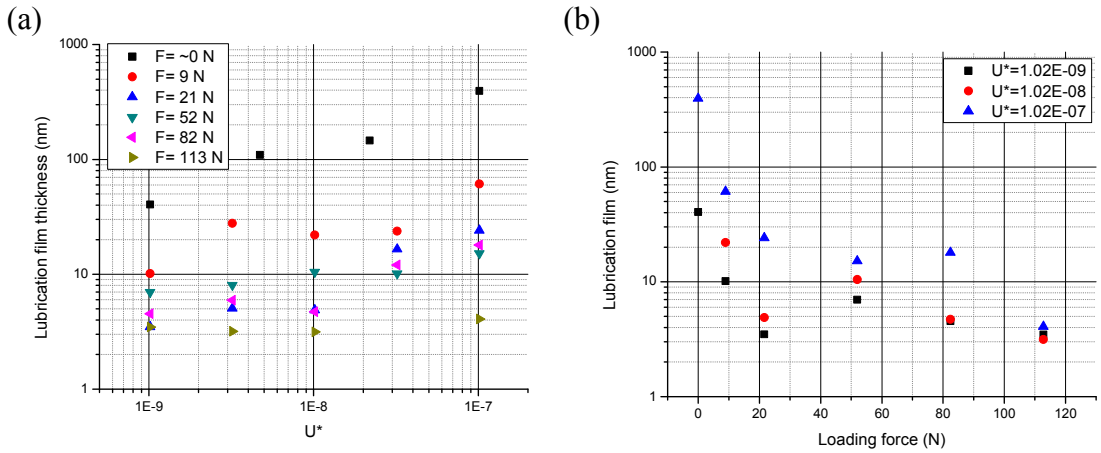

Figure 3.6 The effect of loading force on the median lubrication film thickness as a function of (a) speed parameter and (b) loading force. The loading forces are ~0, 9, 21, 52, 82, and 113 N, which correspond to actuator pressures of 27.6, 51.7, 69.0, 103.4, 137.9, and 172.4 kPa, respectively. At a pressure of 27.6 kPa the exact loading force was difficult to measure accurately; the ~0 value simply denotes the minimum pressure applied on the actuators that is barely sufficient to ensure contact during wiping.

The statistical distribution of film thickness as a function of the loading force is markedly different from that reported above with respect to U*. At low loading force, there is a large spread in the thickness distribution, as shown in Figure 3.7a and Figure 3.7b. With medium loading force, the distributions are much narrower as shown in Figure 3.7c and Figure 3.7d. Once the loading force is high (Figure 3.7e and Figure 3.7f), the distributions are very narrow. In addition, Figure 3.7f potentially also shows some information about wearing. The experiments were run in a series from U*=1.02E-7 to 3.21E-9. Note that during the high loading force experiment, Figure 3.7f, there was significant audible grinding produced for conditions of U*<3.21E-8. The first lubrication film at U*=1.02E-7 is very thin, but the second wiping at U*=3.21E-8 shows much thicker films. This is because the loading force is excessive and the blade is instantly worn during the first run, creating a large number of defects that increase the median thickness on the second wiping. This then represents a potential problem with use of high loading forces on the doctor blade.

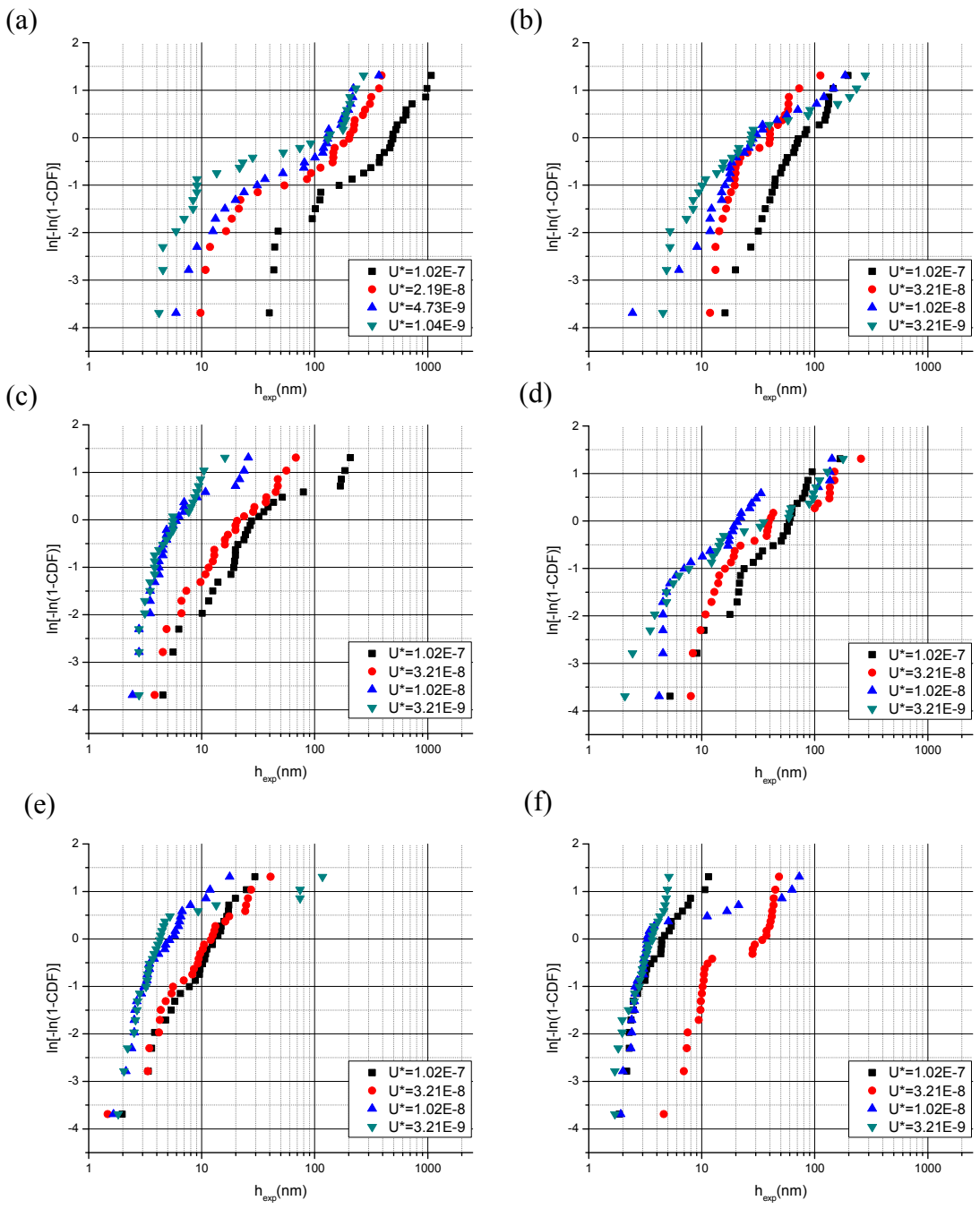

Figure 3.7 Weibull plots of lubrication film thickness as a function of speed parameter and loading forces. From (a) to (f), loading forces are ~0, 9, 21, 52, 82, and 113 N.

Finally, the effects of blade stiffness and angle on residue film thickness were also characterized, as shown in Figure 3.8. The stiffness was increased by using thicker blade tips and bodies as shown in Figure 3.3c. In general, the observed variations were found to fall within experimental

variance; therefore, based on our data to this point, we postulate that blade stiffness and angle are not significant factors affecting residue film thickness.

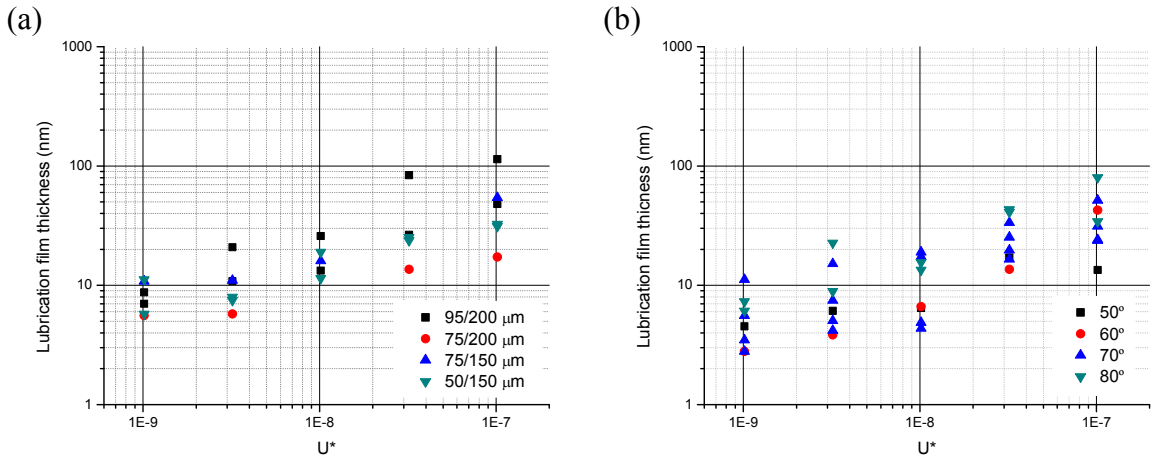

Figure 3.8 The effects of (a) blade stiffness and (b) blade angle on the lubrication film. The PVP concentration used was 32.5 wt% and viscosity was 262 mPa·s. A blade angle of 70° was used in the blade stiffness experiments. The 50/150 μm blade was used in the blade angle experiments. A loading force of 21 N was used in both experiments. Wiping speed was adjusted to obtain different U*.

3.6 Discussion

Wiping in gravure printing is a complex problem, involving both fluid and solid mechanics. A doctor blade is loaded such that when a printing plate is stationary, the blade makes a physical contact with the printing plate. The pressure in the contact zone can be estimated by Hertzian contact theory and the maximum Hertzian pressures between two cylinders with parallel axes ($p_{max} = \left(\frac{E'F}{\pi LR}\right)^{\frac{1}{2}}$) in our experiments range from ~0.7 to ~1.4 GPa, depending on the loading force and the blade radius [14]. Due to the curvature of the tip of the blade, a convergent and divergent channel forms at the inlet of and the outlet of the contact zone respectively. As the printing plate slides, the fluid is dragged along on the surface of the printing plate due to the no-slip condition and viscous force. When the fluid enters the convergent inlet, the pressure must be increased to satisfy the constant flow rate throughout the channel. The order of magnitude of this fluid pressure must be comparable to the Hertzian pressure mentioned earlier in order to establish the lubrication channel. In the divergent outlet with a free-surface flow, the pressure decreases from its peak and it is possible to reach a negative pressure. However, the pressure profile depends on the outlet boundary condition and fluid properties. Since the PVP solutions have a primary component of a volatile organic solvent (PGMEA) with a vapor pressure of 493 Pa, the negative outlet pressure due to the divergent channel and capillary pressure will be limited by this vapor pressure. To satisfy this physical phenomena, a boundary condition, known as Reynolds boundary condition, is typically used as the outlet boundary condition in lubrication bearings [15]. Moreover, in the case of patterned printing plates, the fluid contained in the

patterned cells can interact with this outlet free-surface flow, which we discussed earlier in [5]. This is known as the drag-out effect. Since the residue films from the drag-out effect decline as the doctor blade moves away from the cells, the experiments were designed such that the residue films from the drag-out effect were insignificant and the lubrication films can be studied simply as lubrication films between the blades and flat surfaces.

Because the thicknesses of the lubrication films are below 100 nm, the disjoining force can be important in the problem. To estimate the contribution of the disjoining force caused by the van der Waals force for the film thicknesses of 1 to 100 nm, we use the Hamaker constant, A, of 10E-19 to 10E-20 J and estimate a disjoining pressure ($\Pi(h) = A/6\pi h^3$) of 5 Pa to 0.5 MPa [16]. Since the pressure in the contact zone calculated by Hertzian contact theory is several order of magnitude higher, the contribution of the disjoining force is expected to be minor in the contact zone. However, when the lubrication films are released from the contact zone and slide along with printing plates due to the viscous force, the lubrication films are subjected to the capillary and disjoining forces. These forces determine the stability of these free-surface residue films. In our experiments, the thicknesses perpendicular to the wiping direction varied significantly, but were fairly uniform in the printing direction. This suggests that the major cause of the variation of the film thickness is the blade defects; we suggest that the dewetting of the free-surface films caused by the disjointing pressure is insignificant in comparison.

The rheology of nanometric-thin fluids like lubrication films in the wiping process is unknown and the precise measurement of the fluid properties, especially the viscosity, in such conditions is not available. In [5], we showed that the PVP solutions exhibits shear thinning behaviors and the viscosity approaches a constant at the shear rates of >1E4 1/s. We are also aware that in the wiping process the shear rates and fluid pressures are much higher and the fluid properties could dramatically change, but we pursue the analysis by using the same viscosities as in [5] as a starting point. Next we will propose a possible explanation of the mechanics of the wiping in gravure printing.

Fundamentally, lubrication is a process in which a thin fluid film flows between two solid surfaces. As the fluid flows through a convergent channel, hydrodynamic pressure develops. This hydrodynamic pressure can increase fluid viscosity and/or elastically deform the solids, depending on the fluid and solid properties. Therefore, lubrication can be divided into four regimes [17]. The first regime is called isoviscous-rigid, where the elastic deformation of the solids and the change of viscosity can be neglected. The second regime is known as piezoviscous-rigid, in which only the increase in viscosity is important. Isoviscous-elastic regime occurs when the deformation of solids is substantial. The last regime is known as piezoviscous-elastic. In this regime, both the elastic deformation of the solid and the viscosity increase due to high pressure have to be considered. To gain a physical understanding of lubrication in gravure printing, the lubrication regime must be first specified. Johnson proposed a map of the regimes of lubrication of a contact line [18]. While this work is based on lubrication between a rigid cylinder and a plate, we proceed under the assumption that this is a reasonable starting point, particularly since our experimental results suggest that blade stiffness is not of primary importance. Therefore, we adopted the map suggested by Johnson to evaluate the regime in

which the lubrication in gravure printing operates. The map is governed by three dimensionless parameters [19].

Equation 3.1 $$viscosity\ parameter: g_1 = \left(\frac{2\alpha^2 w^3}{\eta_0 U R^2}\right)^{\frac{1}{2}}$$

Equation 3.2 $$elasticity\ parameter: g_3 = \left(\frac{w^2 \pi}{\eta_0 U E_r R}\right)^{\frac{1}{2}}$$

Equation 3.3 $$film\ parameter: \bar{h} = \left(\frac{2h_m w}{\eta_0 U R}\right)$$

In particular the relationship between the film parameter and the viscosity and elasticity parameters in the piezoviscous-elastic regime can be expressed as [18]:

Equation 3.4 $$\bar{h} = 2.65 g_1^{0.54} g_3^{0.06}$$

Unfortunately, the pressure-viscosity coefficient α is an unknown. In order to estimate α, we calculated the empirical $\bar{h}$ from Eq. 3 using a fit from Figure 3.5f where or 1E-8<U*<1E-6. The Capillary number corresponding to this region ranges from 1 to 100, using a surface tension of 26.9 mN/m; in this regime, the surface tension force is negligible. We then calculated g_1, g_3 and the model $\bar{h}$ from Eq. 1, 2 and 4, respectively. By adjusting α until the ratio of the empirical $\bar{h}$ to model $\bar{h}$ is close to the unity, an estimated α was obtained. The physical parameters and the calculation numbers are listed in Table 3.3 and Table 3.4, respectively.

Table 3.3 Physical parameters for calculation of lubrication regimes

Young's modulus of SiO_2	75 GPa
Young's modulus of blade (carbon steel)	220 GPa
Poisson ratio of SiO_2	0.17
Poisson ratio of blade	0.3
Dimensionless speed	1E-8 to 2E-6
Film thickness	13 to 248 nm
Blade tip radius	25 μm
Loading force	21 N
Contact width	40 mm

Table 3.4 Parameters used to estimate the pressure-viscosity coefficient

h_{exp}(m)	R(m)	Speed×viscosity (N/m)	Pressure-viscosity coefficient (1/Pa)	Viscosity parameter (Eq.1)	Elastic parameter (Eq.2)	$\bar{h}$ empirical (Eq.3)	$\bar{h}$ model (Eq.4)	Ratio of $\bar{h}$ model to $\bar{h}$ empirical
1.31E-08	2.50E-05	0.06	4.70E-09	13.572	1.8910	9.93	11.26	1.13
2.61E-08	2.50E-05	0.14	4.70E-09	8.584	1.1960	7.90	8.55	1.08
4.40E-08	2.50E-05	0.28	4.70E-09	6.070	0.8457	6.65	6.95	1.04
7.40E-08	2.50E-05	0.56	4.70E-09	4.292	0.5980	5.60	5.64	1.01
1.47E-07	2.50E-05	1.39	4.70E-09	2.714	0.3782	4.46	4.29	0.96
2.48E-07	2.50E-05	2.78	4.70E-09	1.919	0.2674	3.75	3.48	0.93
Measured dependent variable		independent variable	Estimated					Targeting to 1.00

The extracted α was 4.7 1/GPa. To confirm that this pressure-viscosity coefficient is in the right range, we performed another estimation based on the experimental molecular weights by using known pressure-viscosity coefficients of similar organic solvents. The predicted value from this method was 6.0 1/GPa for PGMEA (Note that the solute can indeed affect the pressure-viscosity coefficient, but this effect was found to be small in similar polymer-oil solutions [20]), supporting our analysis using pure solvent values. The literature pressure coefficients and extrapolation are in Table 3.5. Thus, we find that the pressure-viscosity coefficients derived using the two methods are in the same range, giving us added confidence in our parameterization.

Table 3.5 The pressure-viscosity coefficients for various organic solvents

Fluid	**Viscosity (mPa·s)**	**Molecular Weight (g/mol)**	**Pressure-viscosity coefficient (1/GPa)**
PGMEA	1.10	132.6	6.00 [Estimated]
2-Propanol	1.96	60.1	4.17 at 22C [Bair and Kottke 2003]
Glycerol	1412	62.1	5.90 at 30C [Gohar 2001]
n-Hexane	0.294	86.2	4.88 at 30C [Brazier 1968]
n-Octane	0.542	114.2	5.88 at 30C [Brazier 1968]

We used α as 4.7 1/GPa to find the lubrication regime relevant to gravure printing. At high U*, i.e. low g_1 and g_3, the wiping lubrication is piezoviscous-elastic and bounded by isoviscous-rigid and piezoviscous-rigid regimes as shown in Figure 3.9. If the pressure-viscosity coefficient is larger than that estimated here, then the wiping will operate in the piezoviscous-rigid regime and if the pressure-viscosity coefficient is smaller, then the wiping will operate in the isoviscous-rigid regime. However, as U* decreases, the lubrication moves away from the boundaries and enters the pure piezoviscous-elastic regime. Since a minimum lubrication film thickness is

desired in gravure printing, it can be said that under optimal gravure printing conditions, we expect that the lubrication in gravure printing operates in the piezoviscous-elastic regime, also known as elastrohydrodynamic (EHD) lubrication. This is an important finding, since it then allows for further insight into the wiping mechanisms during highly-scaled gravure printing.

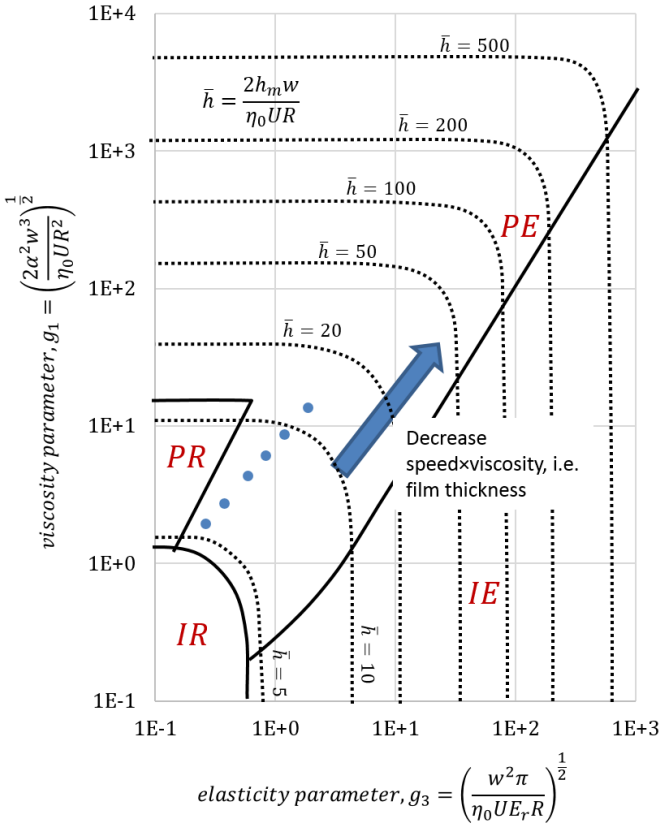

Figure 3.9 A map of lubrication regimes superimposed with experimental data gathered herein. The map is reproduced from [19]. Each regime is indicated as IR:isoviscous-rigid, PR:piezoviscous-rigid, IE:isoviscous-elastic, and PE:piezoviscous-elastic. The blue dots are experimental data from the effects of viscosity and speed where 1E-8<U*<1E-6.

Typically, the equations describing film thickness in EHL predict the central or the minimum film thickness (h_c and h_m) between two solids. In this work, the thickness of the lubrication films left behind were measured. Because the h_c or h_m defines the volumetric flow rate under the blade and the blade slides over the printing plate, this flow rate determines the thicknesses of the resulting lubrication film. Hence, the formula for h_c or h_m should predict the thickness of the lubrication films as well. The analytical solution for EHD lubrication, also known as the Ertel-Grubin equation [14], and the numerical solution by Dowson and Higginson predict that the film thickness is a strong function of U* and G*, but it is a weak function of W_L*. The Dowson and Higginson's formula can be expressed as:

Equation 3.5
$$H = 2.65 \frac{U^{*0.7} G^{*0.54}}{W_L^{*0.13}}$$

This equation is the same as Eq.4, but is differently written such that the dimensionless numbers are grouped to separate the effects of speed, material, and loading. This formula has been successfully tested again several experimental results [11], [19], [21], [22]. Considering again our experiment results on the effect of viscosity and speed in Figure 3.5f, we find that the extracted power low exponent in the range 1E-8<U*<1E-6 is 0.7465. The exponent is close to 0.7 as predicted by Eq. 5. This suggests that, to the first order, the thick lubrication films can be reasonably predicted by EHD model.

However, as the U* reduced below 1E-8, the film thicknesses depart from the formula and becomes a weak function of U*. This can be explained by the concept of mixed lubrication, where the total load is supported by EHD lubrication and something else, such as viscous-like or solid-like boundary films. Spikes and Olver described the transition from full-film EHD to boundary lubrication, based on the lubrication film thickness [23]. As the thickness of the lubrication film reduces, the lubrication transitions from EHD to micro-EHD, mixed lubrication and finally boundary lubrication. Micro-EHD is a condition under which each asperity operate as an EHD contact [14].

To identify the lubrication regime, another dimensionless parameter, lambda ratio ($\lambda = \frac{film\ thickness}{surface\ roughness}$), is normally used to predict the transition from EHD to micro-EHD, mixed lubrication and then boundary lubrication. Typically, a lambda ratio of 1 is the onset of mixed lubrication. In this work, the lambda ratio based on the roughness of the unloaded surfaces is 0.01 to 0.5, which is smaller than 1, and should thus place the all experiments well within the mixed and boundary lubrication regimes. However, the good fit to the EHD model suggests otherwise. This is likely due to the fact that micro-EHD happens in thick lubrication film regions (U*>1E-8). In micro-EHD, the amplitude of roughness in contact zone is attenuated, as was observed by Spikes and Olver, who found that roughness has little effect on the mean film thickness down to 20 nm [23]. In micro-EHD, the kinematics promote local pressure generation associated with asperities, which in turn tends to flatten the asperities causing the perturbation of the pressure. Therefore, the lambda ratio calculated from the roughness of the unloaded surface cannot predict the transition to mixed lubrication and EHD lubrication can thus persist for very small values of lambda [14]. Since EHD and micro-EHD lubrication regimes have a similar mechanism, the EHD model can predict film thicknesses in both conditions. This is consistent with our observation that EHD models describe lubrication films in gravure printing well, even though the blade roughness is larger than the thickness of the resulting lubrication films. The attenuation of the amplitudes of surface roughness under EHD contacts is also discussed in detail by Hooke and Venner [24].

Ultimately, for sufficiently small lubrication films, mixed lubrication will eventually occur. This may explain the deviation from the basic EHD framework observed for film thicknesses below 10 nm in Figure 3.5f. Mixed lubrication can also explain the spread in distributions presented in Figure 3.5f. Figure 3.5a shows that the distribution of film thicknesses is narrow and the median depends strongly on U*. This suggests that the lubrication is in full-film EHD or micro-EHD. As the U* is reduced, the lubrication enters the mixed-lubrication regime, where the minimum film

thickness is limited by the boundary film. Because the film thicknesses are very small here, small variations in the surface profile can spread the distribution dramatically. In other words, the sharp distributions of very thin films of a few nanometers are where the boundary films support the loading force, while the thicker regions are associated with defects, as shown in Figure 3.5e and Figure 3.5d. Because the thickness of lubrication residue depends on the thickness of boundary films, it is worthwhile to mention some parameters that influence boundary film thickness. Smeeth reported on the effect of polymer molecular polarity on the thickness of boundary films [25]. Smeeth's results indicate that polymers with high molecular polarity adsorb well from mineral oil onto steel or silica surfaces. Recently, Fu also demonstrated the effect of interfacial properties on EHD film thickness [26]. Under high load and low speed, a Cr-coated surface results in a lower film thickness and friction than SiO_2 coated surface. This is due to the fact that Cr has lower surface energy than SiO_2, as discussed in the same work.

The effect of actuator pressure on the lubrication film is now discussed. Since 1E-9<U*<1E-7 was selected for these experiments, these lubrication results are all in the mixed lubrication regime. Figure 3.6a shows that as the loading force increases the region of mixed-lubrication is extended with respect to U*. Using the same analysis as above, we would expect tighter statistical distributions then, as a function of increasing actuator pressure. This is indeed what we observe in Figure 3.7.

Operating in the mixed lubrication regime may provide an interesting side benefit; since there are deflections of the solid surfaces in this regime, the forces herein may effectively "flatten" the rough doctor blade with respect to the gravure plate, leading to tighter distributions as experimentally observed. In particular, for commercial gravure applications, where the flatness of the master is much worse than the silicon plate used herein, this is important. The typical radius tolerance of a commercial gravure cylinder radius is ~2 μm [27]. This variation can be considered a waviness of the surface and the value is huge compared to the thickness of the lubrication films. Therefore, the deformation of the blade is essential and guarantees that the lubrication films are thin and uniform throughout the roll surfaces. In other words, sufficient loading is used to ensure lateral deformation of the doctor blade; without this, there would be significant non-uniformity in wiping due to non-uniformity of the cylinder. This lateral deformation is a thus a benefit of operating in the mixed lubrication regime in gravure printing, since it works to improve overall process uniformity.

Next, the effects of blade stiffness and angle are discussed. The stiffness and angle of the blades can affect the vertical deflection of the blades, but do not alter the modulus of the blade. The vertical defection of the blades only effectively alters the blade contact angle, since the blade holder can slide downward freely in our setup. The stiffer blade can maintain a blade angle close to the installed angle, but it will also limit the lateral deformation and create non-uniformity. In the case of mixed lubrication, the film thickness is dictated by the geometry of the contact zone and the material properties within. Since the contact zone is much smaller than the blade length, the effect of vertical defection, i.e. blade stiffness, and blade angle is diminished. Therefore, to first order, the blade stiffness and angle should not affect the thicknesses of lubrication films significantly. This agrees with the experimental results shown in Figure 3.8. In addition, as the

blade angle was changed from 50° to 80°, there were only slight changes in the thickness of lubrication films as shown in Figure 3.8b. This suggests that the pressure developed under the blade body (as opposed to the tip) is insignificant. Therefore, it can be concluded that the loading is mainly supported by the tip of the blade. Therefore, the wiping problem can likely be adequately modeled as the lubrication of a small cylinder sliding over a flat surface.

By understanding the lubrication physics, we can derive some design rules to minimize the lubrication films. First, the gravure ink should have a small pressure-viscosity coefficient and form only a thin boundary film. This allows the printer to be operated at higher speed. Second, because the boundary film is formed by chemical or physical surface adsorption onto the solid surfaces, in order to minimize this film the polarity of the inks must be reduced, i.e. the plate/roll surface should possess somewhat low surface energy to reduce the boundary film. Note that the minimum surface energy of roll surfaces is limited by requirements of the filling process [5]. In additional, the doctor blade must have low surface energy to minimize the boundary film. The low surface energy not only reduces the lubrication film, but also eliminates the drag-out tails, as we previously demonstrated [5]. Third, the doctor blade should have a thin body and tip to promote lateral deformation. The reduction of tip radius also reduces the lubrication film as predicted by Eq. 5. This lateral deformation reduces lubrication film variation due to long wavelength roughness, i.e. surface waviness. Note that short wavelength roughness still remains a concern, since very high force will be required to deform the blade sufficiently over short distances. Therefore, short wavelength roughness must be minimized during the roll manufacturing to allow achievement of a uniform lubrication film.

Finally, recommended operation conditions are outlined. To obtain a thin and uniform lubrication film, significant loading force on the blade needs to be applied. The high loading force promotes the development of high fluid pressure under the contact point of the blade, leading to the lateral deformation of the blade. This is important as a correction mechanism for blade defects and roll waviness. Then, the printing speed and viscosity need to be optimized as discussed above and in our previous work [5]. This is a tradeoff between the wearing of the printer components and the residue. For practical applications, a wet film residue thickness of 5 nm is acceptable, which in turn leaves miniscule amounts of dry residue for typical ink loading values in printed electronics.

To validate our design guidelines regarding the residue films in gravure printing, we performed a comparison between a standard lamella blade (75/150 μm) and a polished blade with a tip radius of 3 μm. We reduced the tip radius in order to minimize both the drag-out and lubrication residues, as discussed earlier. The printed results shown in Figure 3.10 demonstrate a significant improvement of the printing quality, consistent with our expectations. The cross sections of the blades used in Figure 3.10 are available in Figure 3.11. We see that through proper optimization it is indeed possible to produce extremely high quality gravure-printed patterns with minimal residues.

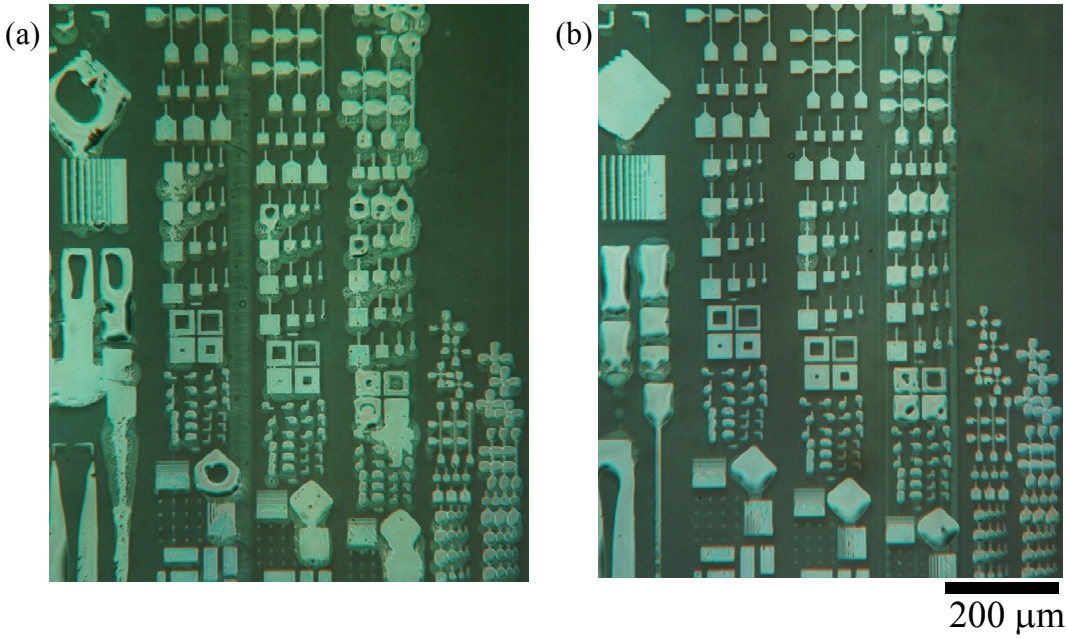

Figure 3.10 (a) printing results using silver nanoparticle inks with a pristine standard lamella blade (75/150 µm) and (b) using a polished blade with a tip radius of 3 µm. The printing speed was 0.5 m/s and the ink viscosity was ~100 mPa·s. The substrates were PQA1 from Dupont.

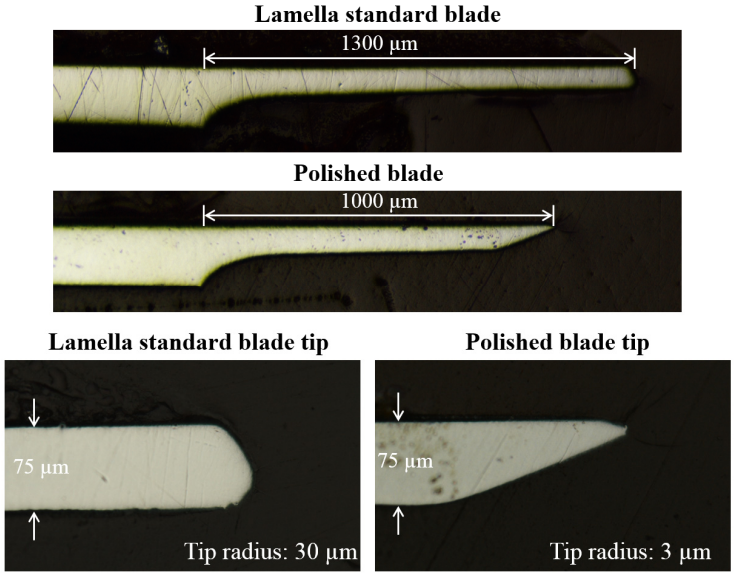

Figure 3.11 A comparison of cross sections of a standard blade (75/150 µm) and a polished blade. The blade was polished using SiC abrasive papers. The final grinding was performed at 1200 grit.

3.7 Conclusions

We provide insight into the physical mechanisms underlying lubrication residues in gravure printing. We use spatially calibrated reflectometry to quantify the lubrication film in highly-scaled gravure printing. The effects of viscosity, speed and loading force on the thickness of lubrication films were presented, along with impact of these parameters on the statistical distributions. Moreover, the effects of blade stiffness and angle were also investigated. The results reveal that at high viscosity and speed the gravure operates in a manner consistent with the elastohydrodynamic lubrication regime. By reducing the product of viscosity and printing speed, the EHD lubrication transits into micro-EHD and finally into the mixed lubrication regime. The thicknesses of lubrication films in the mixed lubrication is governed by the boundary films, setting a fundamental limit on residue reduction in gravure printing. Based on our physical understanding, we provide design guidelines for implementing gravure printing.

The effects of viscosity and speed can be combined into one dimensionless parameter, U*. To minimize the lubrication films, U* must be reduced, but by increasing the loading force, the viable printing speed and viscosity can be extended toward higher values. Additionally, doctor blade loading force is important to force the lubrication to enter EHL and mixed lubrication in the case of very thin films. This loading force not only reduces the median thickness of lubrication films, but also reduces the spread in the same, thanks to the lateral deformation of the blades.

3.8 References

[1] R. Kitsomboonloha and V. Subramanian, “Lubrication-related residue as a fundamental process scaling limit to gravure printed electronics.,” *Langmuir*, vol. 30, no. 12, pp. 3612–24, Apr. 2014.

[2] H. Kang, R. Kitsomboonloha, J. Jang, and V. Subramanian, “High-performance printed transistors realized using femtoliter gravure-printed sub-10 μm metallic nanoparticle patterns and highly uniform polymer dielectric and semiconductor layers.,” *Adv. Mater.*, vol. 24, no. 22, pp. 3065–9, Jun. 2012.

[3] N. Bornemann, H. M. Sauer, and E. Dtirsam, “Gravure Printed Ultrathin Layers of Small-Molecule Semiconductors on Glass,” *Analysis*, pp. 1–8, 2011.

[4] Y. Jung, R. J. Kline, D. a. Fischer, E. K. Lin, M. Heeney, I. McCulloch, and D. M. DeLongchamp, “The Effect of Interfacial Roughness on the Thin Film Morphology and Charge Transport of High-Performance Polythiophenes,” *Adv. Funct. Mater.*, vol. 18, no. 5, pp. 742–750, Mar. 2008.

[5] R. Kitsomboonloha, S. J. S. Morris, X. Rong, and V. Subramanian, “Femtoliter-scale patterning by high-speed, highly scaled inverse gravure printing.,” *Langmuir*, vol. 28, no. 48, pp. 16711–23, Dec. 2012.

[6] X. Yin and S. KUMAR, “Flow visualization of the liquid emptying process in scaled-up gravure grooves and cells,” *Chem. Eng. Sci.*, vol. 61, no. 4, pp. 1146–1156, Feb. 2006.

[7] A. K. Sankaran and J. P. Rothstein, “Effect of viscoelasticity on liquid transfer during gravure printing,” *J. Nonnewton. Fluid Mech.*, vol. 175–176, no. March, pp. 64–75, May 2012.

[8] R. Hanumanthu, “Variation of gravure coating thickness during early stages of doctor blade wear,” *AIChE J.*, vol. 45, no. 12, pp. 2487–2494, Dec. 1999.

[9] I. Lee-Prudhoe and C. Venner, “Experimental and Theoretical Approaches to Thin Film Lubrication Problems,” *IUTAM Symp. ...*, no. March 2003, pp. 241–255, 2006.

[10] G. J. Johnston, R. Wayte, and H. A. Spikes, “The Measurement and Study of Very Thin Lubricant Films in Concentrated Contacts,” *Tribol. Trans.*, vol. 34, no. 2, pp. 187–194, Jan. 1991.

[11] H. a Spikes, “Thin films in elastohydrodynamic lubrication: the contribution of experiment,” *Proc. Inst. Mech. Eng. Part J J. Eng. Tribol.*, vol. 213, no. 5, pp. 335–352, Jan. 1999.

[12] V. Subramanian, P. C. Chang, J. B. Lee, S. E. Molesa, and S. K. Volkman, “Printed organic transistors for ultra-low-cost RFID applications,” *IEEE Trans. Components Packag. Technol.*, vol. 28, no. 4, pp. 742–747, 2005.

[13] B. Dodson, *The Weibull analysis handbook*, Second. ASQ Quailty Press, Milwaukee, Wisconsin, 2006, pp. 20–25.

[14] D. Dowson, “Elastohydrodynamic and micro-elastohydrodynamic lubrication,” *Wear*, vol. 190, pp. 125–138, 1995.

[15] D. Dowson and C. M. Taylor, “Cavitation in Bearings,” *Annu. Rev. Fluid Mech.*, vol. 11, no. 1, pp. 35–65, Jan. 1979.

[16] P. De Gennes, F. Brochard-Wyart, and D. Quere, *Capillarity and wetting phenomena: drops, bubbles, pearls, waves*. Springer, 2004.

[17] B. J. Hamrock and D. Dowson, “Ball bearing lubrication: the elastohydrodynamics of elliptical contacts,” 1981.

[18] K. L. Johnson, “Regimes of elastohydrodynamic lubrication,” *Arch. J. Mech. Eng. Sci. 1959-1982 (vols 1-23)*, vol. 12, no. 1, pp. 9–16, Feb. 1970.

[19] R. Gohar, *Elastohydrodynamics*. World Scientific Publishing Company, 2001.

[20] S. Bair and F. Qureshi, “The high pressure rheology of polymer-oil solutions,” *Tribol. Int.*, vol. 36, no. 8, pp. 637–645, Aug. 2003.

[21] A. Dyson and A. R. Wilson, “Film thicknesses in elastohydrodynamic lubrication by silicone fluids,” *Arch. Proc. Inst. Mech. Eng. Conf. Proc. 1964-1970 (vols 178-184), Var. titles Label. Vol. A to S*, vol. 180, no. 311, pp. 97–112, Jun. 1965.

[22] M. Smeeth, H. A. Spikes, and S. Gunsel, “The Formation of Viscous Surface Films by Polymer Solutions : Boundary or Elastohydrodynamic Lubrication ?,” *Tribol. Trans.*, vol. 39, no. 3, pp. 720–725, 1996.

[23] H. A. Spikes and A. V. Olver, “Basics of mixed lubrication,” *Lubr. Sci.*, vol. 16, no. 1, pp. 1–28, Nov. 2003.

[24] C. J. Hooke and C. H. Venner, “Surface roughness attenuation in line and point contacts,” *Proc. Inst. Mech. Eng. Part J J. Eng. Tribol.*, vol. 214, no. 5, pp. 439–444, Jan. 2000.

[25] M. Smeeth, H. Spikes, and S. Gunsel, “Boundary Film Formation by Viscosity Index Improvers,” *Tribol. Trans.*, vol. 39, no. 3, pp. 726–734, Jan. 1996.

[26] Z. Fu, P. L. Wong, and F. Guo, “Effect of Interfacial Properties on EHL Under Pure Sliding Conditions,” *Tribol. Lett.*, Sep. 2012.

[27] K. Gillett, “Gravure—Process and Technology,” *GAA GEF, Rochester, 2nd Ed. New York*, 2003.

Chapter 4 Cell Filling in Gravure Printing

The filling of the cells on the gravure cylinder is a critical process, since the amount of ink in the cells strongly impacts printed feature size and quality. Therefore, an understanding of cell filling is crucial to make highly scaled gravure printed electronics viable. In this chapter we report a novel experimental setup to investigate the filling process in real time, coupled with numerical simulations to understand this process in depth. By varying viscosity and filling speed, we ensure that the dimensionless capillary number is a good indicator of filling regime in real gravure printing. In addition, we also examine the effect of cell size on filling as this is important for increasing printing resolution. In the light of experimental and simulation results, we are able to explain the dominant failure in the filling process, i.e. air entrapment, which is caused by contact line pinning and interface deformation over the cell opening. All results in this chapter are in preparation for publication in [1].

4.1 Introduction

To ensure the technological viability of gravure printing, and to enable the continued scaling and optimization of the same, detailed studies on the various phenomena involved in gravure printing are required. Gravure printing is composed of four successive processes as described in chapter 2: 1) filling of cells on the gravure master with ink, 2) wiping of excess ink using a doctor blade, 3) transferring of ink from the gravure master to the target substrate and 4) spreading of the transferred ink on the target substrate to realize the final printed pattern. A schematic representation of an archetypal gravure printing process is shown in Figure 4.1a. The details of the wiping and transferring processes have been previously described by various researchers, including ourselves [2]–[5]. The spreading process, which involves surface energy minimization during drying, has been described [6]–[10] as well; most past work in this regard has mainly focused on inkjet, but provides an excellent body of knowledge for analysis of gravure-deposited ink patterns since these are also deposited in a sequentially pixelated manner, similar to inkjet. However, reports on the cell filling process during gravure printing are scarce, in spite of the fact that the filling process is a crucial step for successful printing because partial filling of cells can dramatically reduce total printed volume, which in turn significantly impacts overall print resolution and quality and also impacts process throughput. The reduction in printed volume results in defective features such as discontinuous lines and non-uniform coating films, which are very disadvantageous for precision printing of electronic devices. We addressed this concern in chapter 2 by working at low capillary numbers, but did not show detailed experimental studies of the filling process at high capillary number, which is important in high-speed printing. In this chapter, we report a unique experimental setup that allows us to explore the filling process at high capillary number in more detail. In addition, we also perform numerical simulations to further analyze the filling mechanism. Therefore, in this work, for the first time we provide a comprehensive view of the cell filling process in high-speed, high-resolution gravure printing, and use our obtained experimental results to provide a physical understanding of the phenomena involved during cell filling. This understanding will be critical for the continued scaling and optimization of gravure printing, as will be required to make gravure printed electronics a reality.

Fundamentally, the filling process in gravure printing involves a moving contact line on engraved surfaces and the deformation of an air-liquid interface into/over engraved cells. There are several reports discussing the motion of a contact line and the effect of geometric structures such as groove edges on contact line motion. This edge effect was first considered by Gibbs [11] when he analyzed the equilibrium of air-liquid-solid contact lines on solid surfaces. An inequality based on the geometric relationship between the equilibrium contact angle and the sharp edge was derived. Starting from this derivation, Oliver [12] experimentally investigated the effect of a sharp edge on liquid spreading at the macroscale. As the contact line reaches the sharp edge, its apparent liquid-solid contact angle is increased due to pinning at the sharp edge. When the apparent contact angle exceeds the critical value defined by the static liquid-solid contact angle and wall inclination angle, the contact line slides down the sides so that the liquid-solid contact angle can be decreased to the equilibrium value. Ondarcuhu [13] showed the pinning effect on sharp edges at a nanometric scale by studying the dynamics of dewetting of polystyrene films on terraced alumina surfaces. The terraced alumina surfaces consist of nanometric upward and downward steps. During the dewetting process, the contact line moves up the upward steps but pins at the downward steps, agreeing with Gibbs [11]. This suggests that the contact line pinning is valid in macro and microscopic length scales.

Similarly, various studies have been conducted on liquid interface deformation over basic topography such as grooves. Bankoff [14] theoretically discussed conditions under which air entrapment during filling of inverse triangular grooves can occur based on different geometries and contact angles. For a very steep groove whose inclination angle Φ (angle between groove wall and the horizontal boundary) is much larger than 45° and where the liquid-solid contact angle θ is not approaching zero, complete filling with liquid is not possible. On the other hand, for an inclination angle much smaller than 45°, the filling process will be complete regardless of liquid-solid contact angle. Bankoff also states that small θ will promote complete filling. Therefore, to achieve complete filling in grooves, small inclination and small contact angles are preferred. Reddy [15] simulated the interface deformation through a sharp groove using 2D simulation at low capillary number with a static contact angle of 30°. Their model consisted of fluid flowing through a small channel with a groove located on the top boundary. Their results show that the top contact line pins at the rounded corner of the groove while the bottom contact line continues moving along the bottom of channel, stretching the liquid-air interface. When the interface is sufficiently stretched, the contact line enters the flat surface of the groove. The stretched interface then experiences a rapid reconfiguration such that a lower surface energy is attained, leading to complete filling. None of these works discuss the effects of three-dimensional (3D) cell geometry, which is relevant to the filling process in gravure printing. To begin addressing 3D effects, Brethour and Benkreira [16] simulated a filling process on a shallow quadrangular gravure cell using a controlled-volume VOF method at different capillary numbers. Their model used a static contact angle of 30° and was performed at a capillary number of 0.25. Their results show that the advancing contact line moves into the groove quickly enough so that air entrapment is not present. Their results further showed that low roller speed and low static contact angle give the greatest filling fractions. Low roller speed allows the contact line to move farther down the groove before air is entrapped and low contact angle leads to faster

advancement of the contact line. These studies focused entirely on low capillary number scenarios and lack detailed experimental results at high capillary numbers and at different cell sizes.

Although filling for simple groove geometries has been studied intensively as described above, a complete understanding of filling in gravure printing requires more realistic analyses than contact line pinning and filling of these simplified structures due to the fact that gravure printing deals with a geometrically complex cell at the microscale. Therefore, in this chapter, we report an experimental setup to provide a direct observation of the filling process, displaying moving contact lines and interface deformation over realistic engraved cells. By varying filling speed, liquid viscosity and cell size, we are able to establish a successful filling process window based on capillary number and cell size. In addition, we couple our experimental results with simulations using a level-set method to gain a physical understanding of the filling process. Based on our experimental and simulation results, we propose a pathway to achieve complete filling at high speed.

4.2 Experimental section

In direct gravure printing, the inking of the gravure cylinder can be considered to be a one-sided puddle coating system, as shown in Figure 4.1a. The wedge between the doctor blade and the roll surface acts as an ink reservoir. When the roll rotates, the liquid-air interface deforms and a dynamic contact angle is developed at the moving contact line on the roll surface. The cell filling process occurs at the dynamic contact line when engraved cells enter the liquid-air interface. At high speed, where the capillary number is larger than 1, the dynamic contact angle is larger than 90° [21]. Therefore, a direct observation of the filling process is difficult on a real system because the liquid-air interface curvature prohibits a direct optical path. In order to study the filling process in real time at high capillary number, we simplify the geometry of the system as follows. Since the roll radius for any realistic gravure printer is much larger than the cell dimension for highly-scaled features, we posit that the roll curvature has negligible effects on the filling process and thus, the filling process can be studied on a flat surface. Hence, the filling process can be experimentally simulated by plunging an engraved flat surface into a liquid container as shown in Figure 4.1b and Figure 4.1c, where a directly observable optical path can be obtained. This is because a dynamic contact angle forms at the substrate and a static contact angle forms at the container wall as illustrated in Figure 4.1c. Since the dynamic contact angle depends on the filling speed, ink viscosity and surface tension, it is typically quantified using a single dimensionless number, the capillary number Ca [2]. The actual dynamic contact angles are observed during the experiment using a high-resolution side camera as shown in Figure 4.1b. A relationship between dynamic contact angle and Ca in our experiments is available in Figure 4.2. To guarantee a consistent filling process, the filling process is recorded by a digital camera only when the dynamic contact angle is stable.

Because the optical path for camera-based observation must pass through the wall of the container and the test fluid as shown in Figure 4.1c, silicone oil is selected here to match the refractive index of the glass container and to provide a different refactive index than that of air.

This allows clear observation through a glass container and a good contrast at the liquid-air interface. Due to this optical contrast, the contact line and liquid-air interface can be seen as a darker region and its deformation and the behavior of air entrainment can be directly observed. In addition, silicone oils are available with a wide range of viscosities, which allows a comprehensive study covering a wide range of capillary numbers.

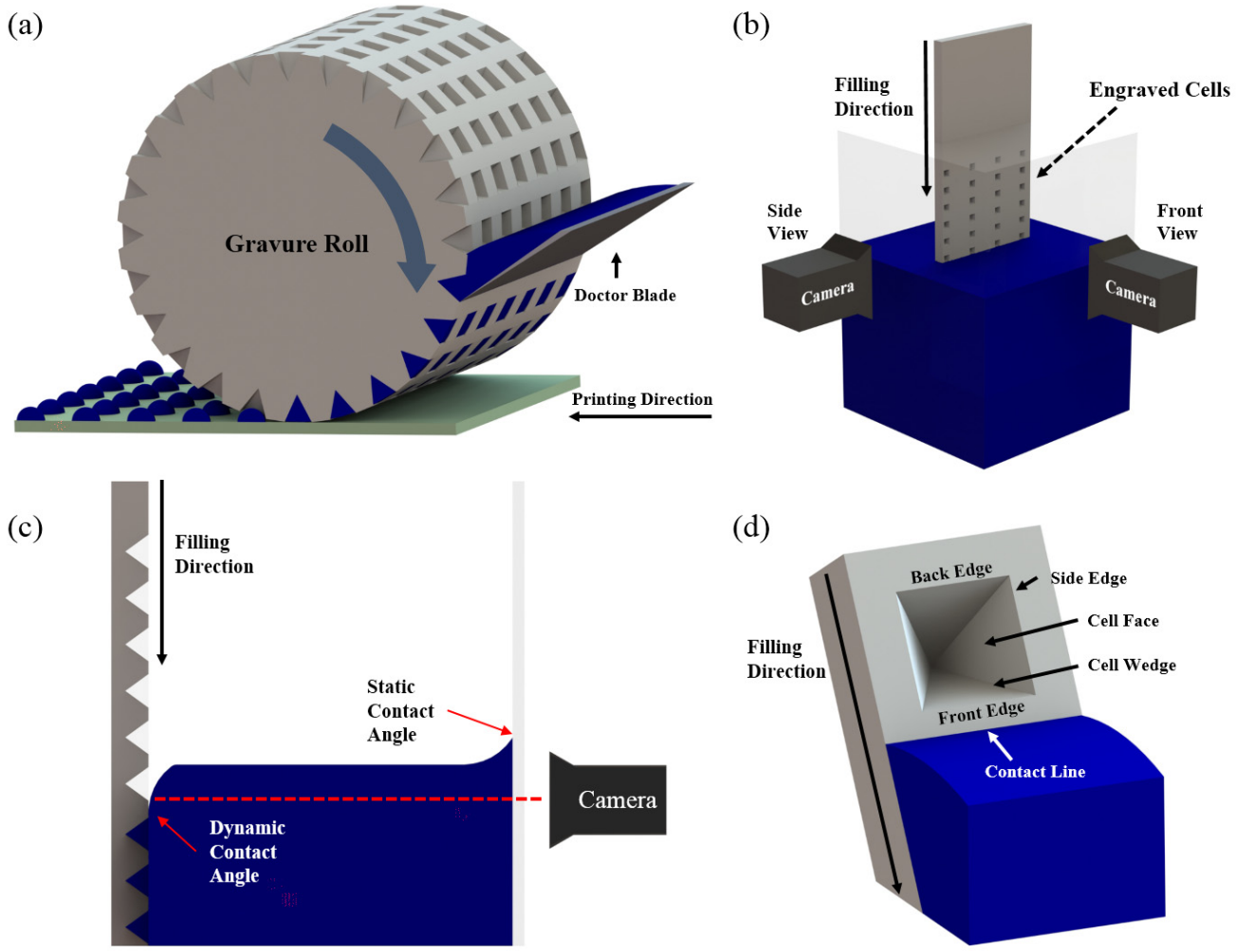

Figure 4.1 a) Typical gravure printing process; b) Overview of filling experiment setup; c) Cross sectional schematic of filling experiment, showing deformation of the liquid-air interface and observational optical path; d) Close-up of filling process with an engraved cell rolling towards the liquid-air interface and definition of the cell features.

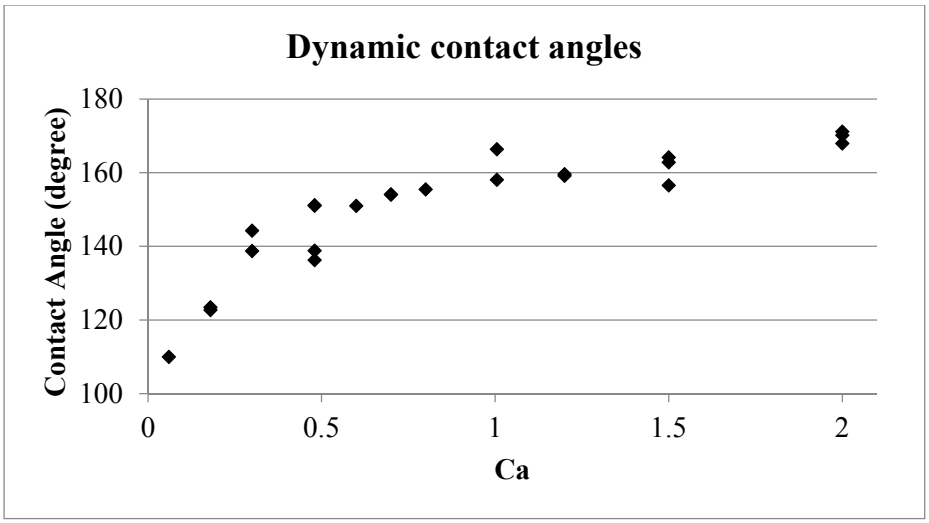

Figure 4.2 Experimental contact angles as a function of capillary number, measured by optical imaging using a side-view camera during filling experiments.

To precisely fabricate arrays of microscale square cells with smooth surfaces, we use silicon substrates as the "engraved" surface and standard microfabrication techniques to create the "engravings". The resulting cells match those we have previously reported in our studies on highly-scaled gravure printing [2], and indeed, are also similar and shape and structure to engraved cells using state of the art engraving techniques [18]. The fabrication process starts by using optical lithography and reactive ion etching to define a cell opening in an oxide masking layer on a (100) silicon wafer. The wafer was then dipped into a potassium hydroxide (KOH) solution to perform anisotropic wet etching of the silicon, forming ideal inverted pyramid cells. After that, the oxide layer was removed by wet etching using hydrofluoric acid. As a result of this process, a prefect inclination angle of 54.74° with smooth surfaces and sharp edges can be obtained. Figure 4.1d illustrates the cell features and definitions of cell feature nomenclature. Cell sizes, defined as the opening width of inverted pyramid cells used in this study, were 30, 40, 60 and 100 μm. After performing filling experiments, the substrate is wiped with toluene to remove most of the silicone oil on surfaces, followed by sonication in toluene for 10 min. After cleaning, a contact angle measurement with water droplets was performed to ensure the cleanliness of the substrates. The values of measured contact angle are generally less than 15°. By varying viscosity and filling speed, different filling regimes can be studied with respect to capillary number. The complete set of experimental conditions used are available in Table 4.1.

Table 4.1 filling conditions

Fluid kinematic viscosity (m^2/s)	Cell size (μm)	Capillary number
0.300	100, 60, 40, 30	10.0
0.100	100, 60, 40, 30	0.1, 0.3, 0.5, 0.7, 0.8, 1.0, 2.0, 3.0
0.060	100, 60	0.1, 0.2, 0.5, 0.8, 1.0, 2.0
	30, 40	0.1, 0.2, 0.5, 0.7, 0.8, 1.0, 2.0

0.030	100, 60	0.1, 0.3, 0.5, 0.7, 0.8, 1.0, 2.0
	30, 40	0.1, 0.2, 0.3, 0.5, 0.7, 0.8, 1.0, 2.0
0.010	100, 60, 40, 30	0.04, 0.07, 0.1

4.3 Experimental results

To properly discuss experimental results, we define two dimensionless parameters. The first is the capillary number, which relates different filling speeds and fluid properties and is defined as:

Equation 4.1 $$Ca = \frac{U \cdot \eta}{\sigma}$$

Where U is the filling speed, η is the fluid viscosity and σ is the surface tension.

The second number is dimensionless time, which relates the interface deformation at different filling speeds and cell sizes. Therefore, the relative dimensionless time is defined as:

Equation 4.2 $$t^* = \frac{U \cdot t}{W}$$

Where W is the cell size and t is the dimensional time. In this study, t* = 0 is selected as the time when the front cell edge reaches the contact line.

We begin the experimental study by performing the filling process at various viscosities and filling speeds at the same capillary number in order to experimentally confirm that the filling process is governed by the proposed capillary number. Figure 4.3a shows optical micrographs of cells filled with inks of different viscosity, with speed adjusted to provide a fixed capillary number. Each row shows the filling status for the different inks at the same t*. The results clearly establish the similarity of the contact line deformation and air entrapment, regardless of viscosities and filling speeds. This confirms that the proposed capillary number is a good candidate for non-dimensionalizing the filling process. Dimensionless time also represents a good time scale for studying filling process, since cells with different sizes follow similar temporal trends at the same dimensionless time (Figure 4.5). By varying the capillary number used, the filling process is rapidly changed from completely filling to non-filling as illustrated in Figure 4.3b. As Ca increases, the movement of the contact line is changed and the volume of entrapped air, which is bounded inside the cell, increases. Figure 4.3c highlights the difference in experimental results, depending on the capillary number. The boundaries of air entrapment can be clearly seen at Ca>1.0.

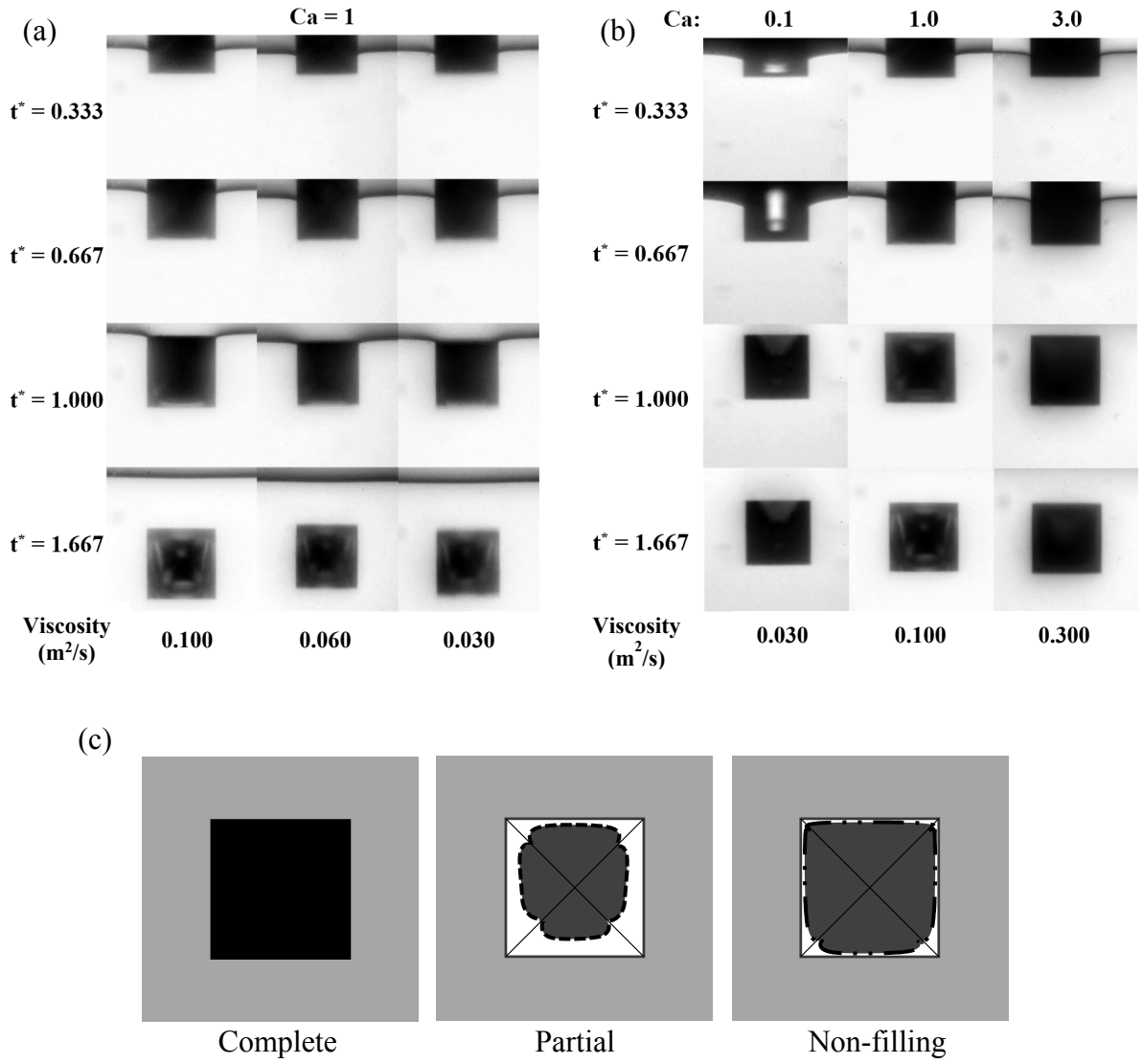

Figure 4.3 (a) Filling processes (top-view) of 100-μm cells using various viscosities at the same capillary number are compared at the same dimensionless times. The cell moves from top to bottom. Light and dark areas in the cell indicate liquid and air regions, respectively. Similar contact line deformation as well as air entrapment deformation are observed regardless of different viscosities and filling speeds, suggesting that the capillary number, Ca, and dimensionless time, t*, represent the filling process. (b) Filling process at capillary numbers of 0.1, 1 and 3, showing complete, partial filling, and non-filling conditions. The kinematic viscosities are 0.030, 0.100 and 0.300 m^2/s from left to right. (c) Schematics of different cell filling status at t*=1.667 showing: complete filled, partial filled and non-filling, from left to right, respectively. Dashed curves show the boundaries of air entrapment.

A detailed filling process of a 100-μm cell at low Ca is demonstrated in Figure 4.4a. As the cell enters the interface by moving from top to bottom in Figure 4.4a, the contact line pins at the front cell edge and the interface deforms around the cell edges. When the cell moves down further, the

contact line is released from the front edge and moves along the cell faces. This motion of the contact line displaces air from the cell. As the cell continues moving downward, the side contact lines reach the back edge and the center contact line comes close to the bottom of the cell. Along the surface behind the back edge, the contact line moves freely, as shown in Figure 4.4b. Because the contact lines move laterally, the air channel gets smaller, leading to a capillary necking effect. When the air channel is sufficiently narrow, a capillary breakup occurs, as shown between t*=0.607 and 0.613. The capillary breakup leaves a small air bubble behind at the bottom of the cell. Although there is a small air bubble, we consider this condition as the threshold for complete filling when we define different filling regimes, since the air bubble is generally found to be subsequently displaced, leaving the cell fully filled. After the capillary breakup, the contact line relaxes back to a straight contact line, as shown from $t^* = 0.643$ to 0.693, such that minimum surface energy can be achieved. At lower capillary number, complete filling is always observed.

At high capillary number, the contact line pinning phenomenon profoundly affects the filling process, as shown in Figure 4.4c. The contact line pins at the front edge, but moves freely along the side cell edges. Once the contact lines on the side edges reach the back edge, they quickly move along the back edge toward the center of the cell, breaking the air channel between the cell and outer interface, trapping the air. In Figure 4.4c from t* = 0.6 to 1.4, the contact line can only slightly enter the cell from the front edge. Therefore, the air entrainment is almost equal to the cell volume. It is interesting to observe that the interface of the entrapped air continues to deform even when the moving contact line is separated from the cell from t*= 1.4 to 3.4. This significant interface deformation of the dark area in the cell confirms the existence of an air bubble at high capillary number. The contact line at the front edge advances faster than it does at the back edge due the fact that the contact line near the front edge moves down the cell face first whereas the contact line near the back edge is still pinned at the edge. As the liquid-air interface deforms in Figure 4.4c from t* = 1.8 to 3.4, the contact lines on the cell wedges move toward the center of the cell faster than on the cell faces, resulting in trapping of air within the cell. This trapped air within the cell thus prevents complete filling of the cell. In other words, air entrapment represents a fundamental limit for gravure printing since it places an upper bound on the capillary number usable during the filling process. This in turn sets limits on the maximum achievable printing speed for a given ink.

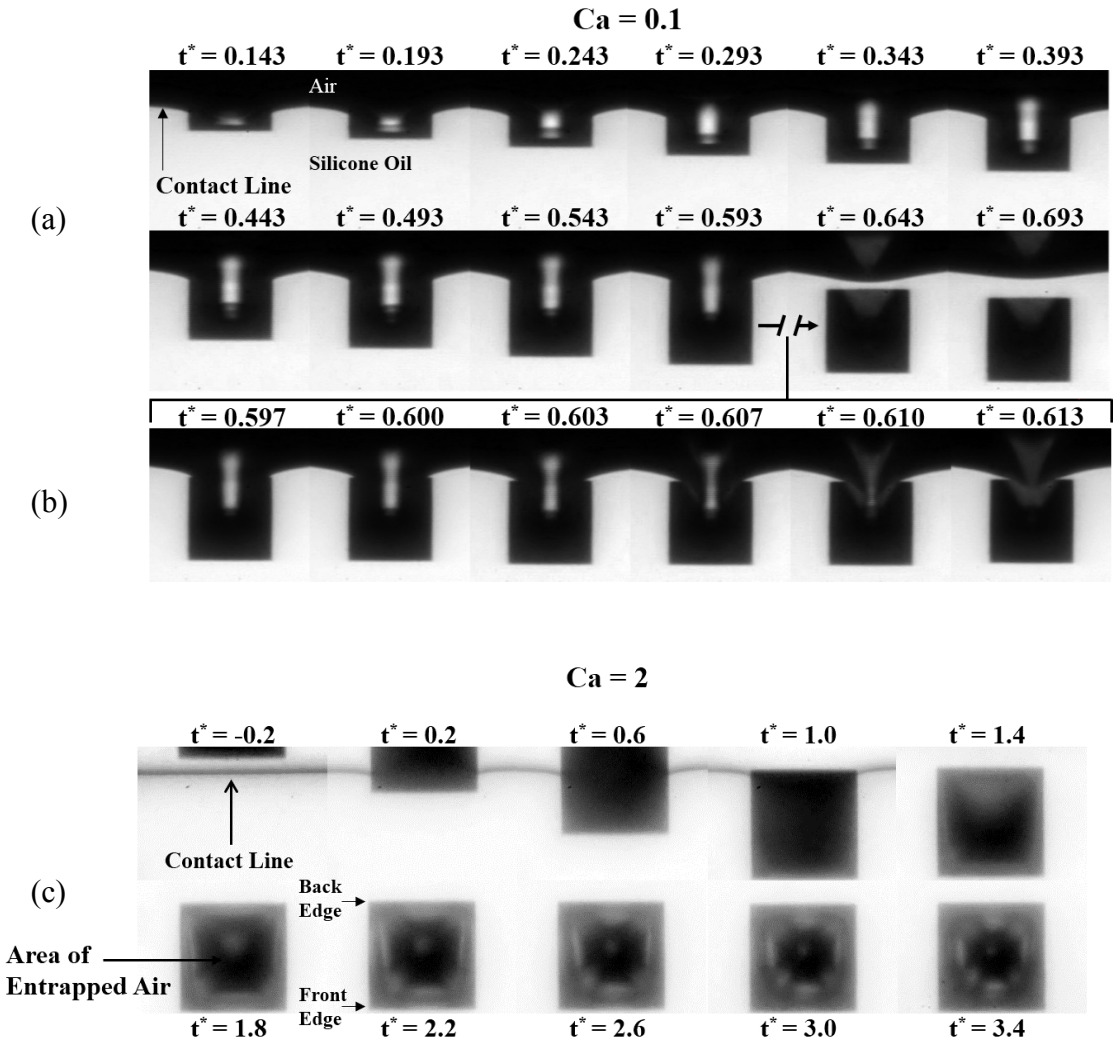

Figure 4.4 Filling processes of a 100-µm cell using 0.100 m^2/s silicone oil. (a) Filling process at Ca = 0.1. Fast time lapsed photographs showing a complete filling process as the contact line displaces air; (b) Slow time lapses photographs highlighting a capillary breakup during the filling process, causing a small air bubble at the bottom of the cell. (c) Filling process at Ca = 2: Cell approaches the stable contact line from the top (t* = -0.2); Contact line pins at the corner and edges of the cell (t* = 0.2 to 1.0); Contact line leaves the cell but air bubble remains (t* = 1.4); Air bubble starts to deform (t* = 1.8 to 3.4).

Next, the effect of cell size is studied. At the same capillary number, the filling processes of different cell sizes can be compared by using the dimensionless time, t*, as proposed earlier. With respect to t*, the filling processes are similar as shown in Figure 4.5a. This similarity of filling at the same capillary number is also presented for the high capillary number condition, where air entrainment exists. A comparison of the filling process of cells with different sizes at high Ca is available in Figure 4.5b. Similar contact line deformation at the cell edges and air entrapment occurrence can be seen as well as the deformation of entrapped air. Therefore, it is

experimentally observed that the filling process does not depend on cell sizes when considered at the appropriate dimensionless time.

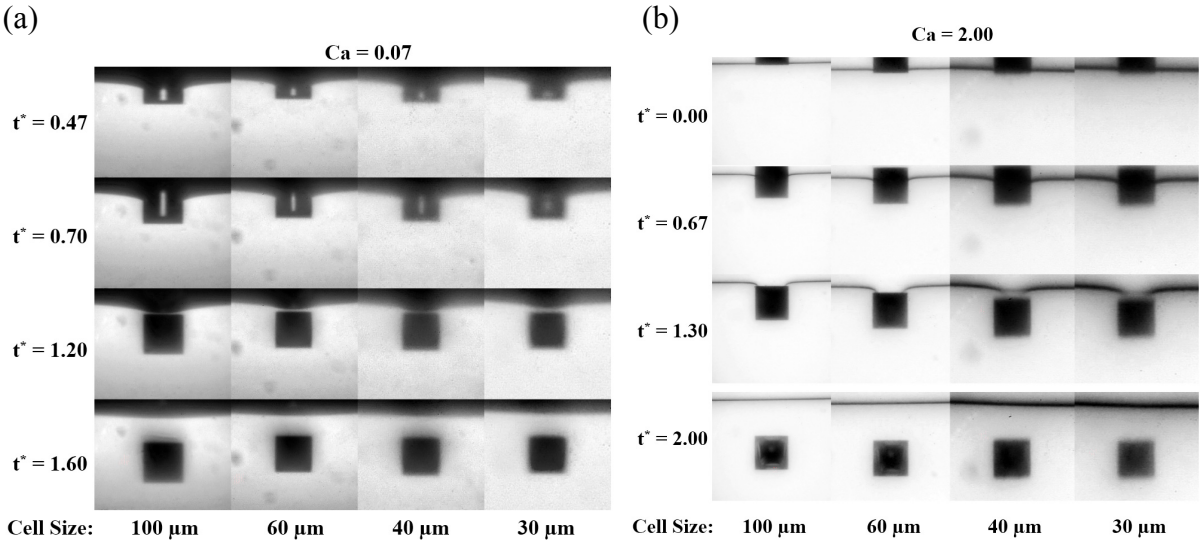

Figure 4.5 (a) Effects of cell size at Ca = 0.07 using 0.010 m^2/s silicone oil. Filling processes are compared by using dimensionless time and images are scaled accordingly to the same size to show a similarity of the filling process regardless of cell sizes. In all cases, the filling process is complete, because contact lines can be deformed and move along cell faces freely in all directions. (b) Effect of cell sizes at high capillary number of Ca = 2 using 0.100 m^2/s silicone oil. Filling processes are compared by using dimensionless time and images are scaled accordingly to the same size to show the similarity of filling processes regardless of the cell size. Air entrapment and air bubble deformation are clearly visible at t*=2.0 for 100 and 60-µm cells but are not obvious for 30 and 40-µm cells due to limitations of lighting and optical resolution.

Finally, we establish filling regimes by summarizing the experimental results obtained from filling experiments using various cell sizes, filling speeds and liquid viscosities. Figure 4.6 shows that the completion of the filling process is independent of cell size but is strongly dependent on the capillary number. The transition between the completely filled and the unfilled cases falls between Ca=0.1 to 1. Above capillary number of 1, completely unfilled cells (air entrapment) are observed.

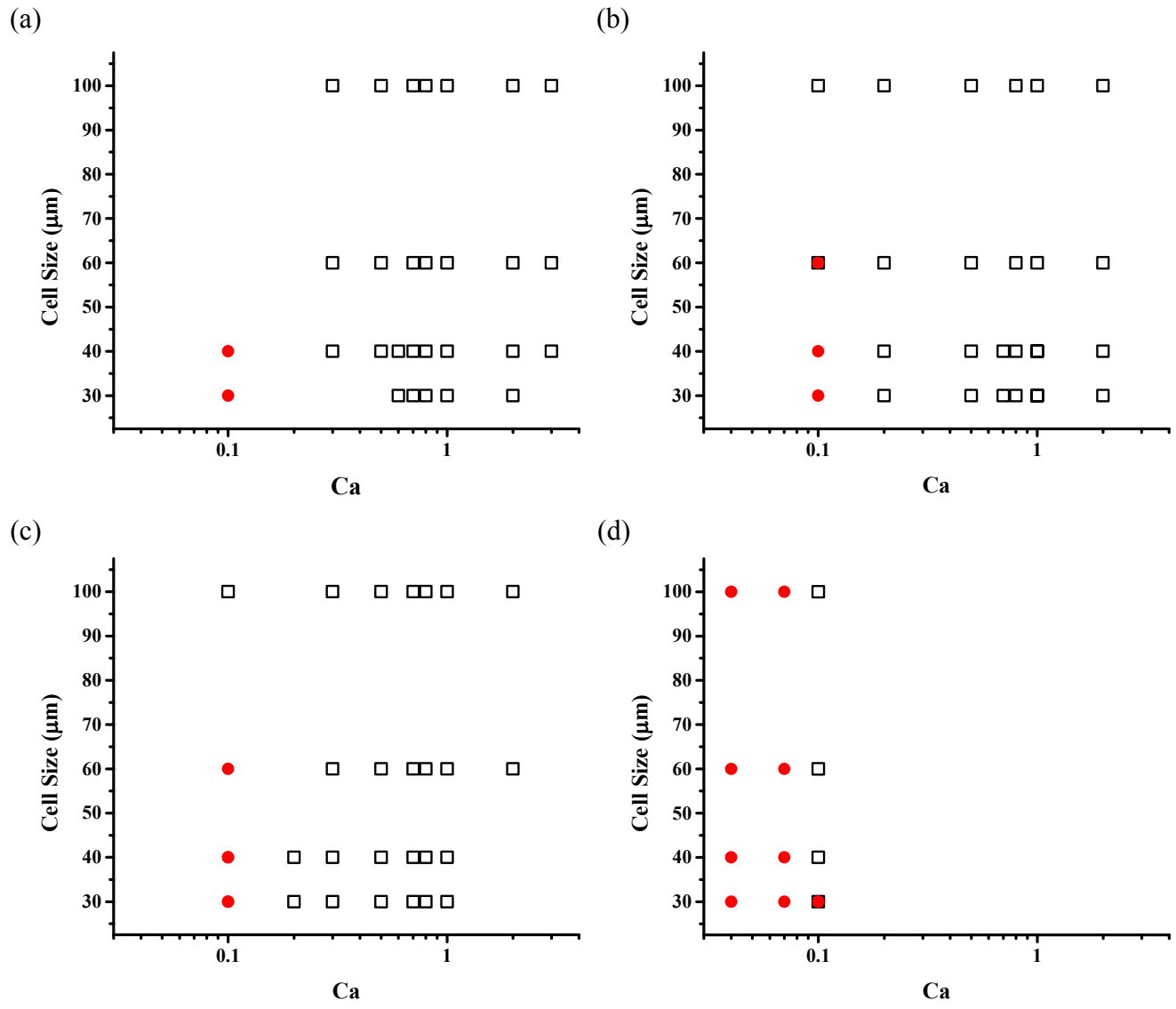

Figure 4.6 Summarized experimental results. Filled cells are represented by solid circles while the open squares stand for unfilled cells. Completely filled cases are observed under capillary number of 0.1. The kinematic viscosities are 0.100, 0.060, 0.030, and 0.010 m^2/s from (a) to (d), respectively.

4.4 Simulation section

In order to understand the filling process in detail, we simulate the multiphase-flow using a level-set method to track the interface movement using COMSOL Multiphysics. Despite the fact that the simplified simulations limit quantitative accuracy, they are found to be useful in providing physical insight into the processes involved, since the experimentally observed major filling and air entrapment phenomena are all observed in the simulation at well, albeit at different dimensionless times than observed under experimental conditions.

4.4.1 Simulation of a laminar two-phase flow

In order to track the interface movement in our simulation, a laminar two-phase flow with level set method has been used [19]. The air-fluid interface is described by the 0.5 contour of the level set function, φ, which has a value of 0 in the air phase and 1 in the fluid phase. The level set function is governed by the following transport function:

Equation 4.3 $$\frac{\partial \varphi}{\partial t} + \vec{v} \cdot \nabla \varphi = \gamma \nabla \cdot (\varepsilon \nabla \varphi - \varphi(1-\varphi)\frac{\nabla \varphi}{|\nabla \varphi|})$$

where $\vec{v}$ is the velocity field in m/s. The factor, γ, determines the amount of reinitialization. The parameter ε controls the thickness of the interface. The density and viscosity are defined by the following equations:

Equation 4.4 $$\rho = \rho_{air} + (\rho_{fluid} - \rho_{air})\varphi$$

Equation 4.5 $$\eta = \eta_{air} + (\eta_{fluid} - \eta_{air})\varphi$$

where ρ in kg/m^3 stands for the density and η in Pa·s is the dynamic viscosity. The interface normal can be calculated by:

Equation 4.6 $$\hat{n} = \frac{\nabla \varphi}{|\nabla \varphi|}$$

The Navier-Stokes equation describing the mass and momentum transportation for incompressible flow is defined by:

Equation 4.7 $$\rho \frac{\partial \vec{v}}{\partial t} + \rho(\vec{v} \cdot \nabla)\vec{v} = \nabla \cdot [-P\vec{I} + \mu(\nabla \vec{v} + (\nabla \vec{v})^T] + \vec{F}_{surface\ tension} + \rho \vec{g}$$

Equation 4.8 $$\nabla \cdot \vec{v} = 0$$

where P is the pressure in Pa, μ is the viscosity in Pa·s, and $\vec{g}$ is the gravitational vector in m/s^2. The surface tension term acting at the air-fluid interface is added to account for the capillary effect.

It can be computed by:

Equation 4.9 $$\vec{F}_{st} = \nabla \cdot [\sigma \left(\vec{I} - (\hat{n}\hat{n}^T)\right)\delta]$$

Equation 4.10 $$\delta = 6|\nabla \varphi||\varphi(1-\varphi)|$$

The δ function is nonzero only at the air-fluid interface.

4.4.2 Simulation of completely filled cells

The 3D simulation setup shown in Figure 4.7 is a half model. The boundary conditions are indicated. The 100-µm pyramidal cell attached to the rectangular pipe has a rounded corner with 1-µm radius at the junction to smooth out the simulation. A normal inflow of U is applied at the inlet on the left and it flows through the pipe and exits at the outlet on the right. The gauge

pressure at the inlet and outlet are set to be zero. At the bottom boundaries and cell faces, a wetted wall condition with imposed static contact angle θ_s and slip length of β is used to allow for slip. β is chosen to be the local grid size of h. On the top and side walls, we use a symmetrical boundary condition satisfying the following conditions:

Equation 4.11 $$\vec{v} \cdot \overrightarrow{n_b} = 0, \quad \vec{\kappa} - (\vec{\kappa} \cdot \overrightarrow{n_b})\overrightarrow{n_b} = 0$$

where $\overrightarrow{n_b}$ is the normal to the boundary and $\vec{\kappa} = \eta(\nabla\vec{v} + (\nabla\vec{v})^T)\overrightarrow{n_b}$ is the stress tensor. This condition prescribes no penetration and vanishing shear stresses at the selected faces. The values of level set parameters are listed in Table 4.2. The largest grid size h_{max} is about 2.5-μm whereas the smallest is about 0.2-μm.

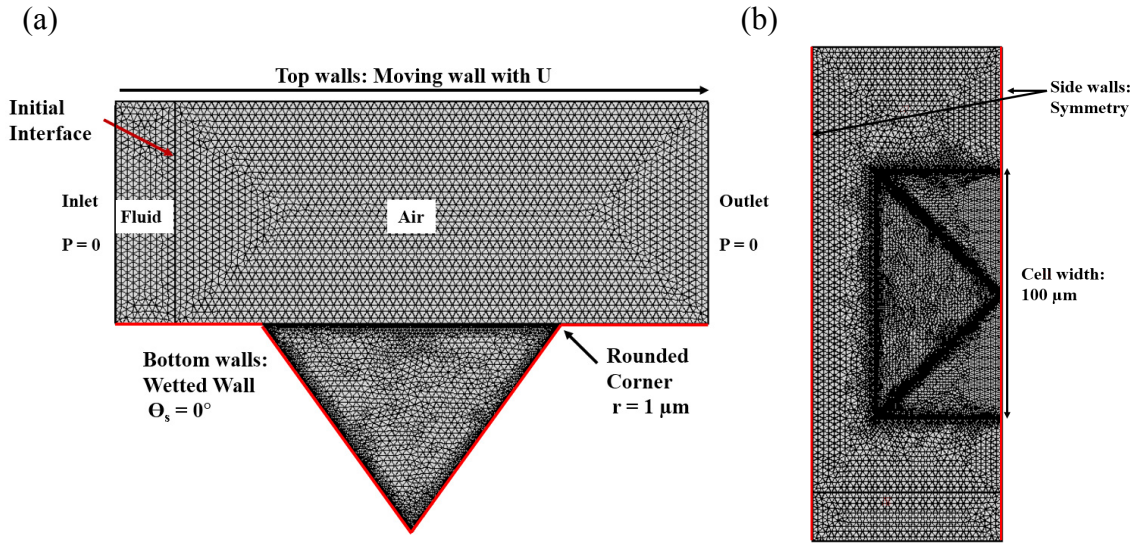

Figure 4.7 3D simulation model setup with boundary conditions. (a) Side view including indicated boundary conditions. Fluid initially exists on the left of initial interface while air is on the right. (b) Top view of the model.

Table 4.2 Simulation parameters

Physical parameter	Value
Air density (kg/m^3)	1.22
Air dynamic viscosity (Pa·s)	18E-6
Liquid density (kg/m^3)	970
Surface tension, σ, (N/m)	20E-3
Reinitialization parameter, γ (m/s)	U
Interface thickness, ε (m)	$0.5h_{max}$

4.4.3 Simulation of deformation of trapped air

A 3D simulation is used to study the interface deformation of trapped air. Shown in Figure S4, the same bottom boundaries with wetted wall conditions are used. Assuming 100% air

entrapment in the cell at the beginning, the initial interface is chosen as indicated and fluid occupies the top tank initially. At the inlet and outlet, the gauge pressure is set to be zero. At the top walls, a moving wall with U is applied in order to simulate the shear rate above the air interface that matches the experiment. The same boundary conditions are used at the side walls as in the previous simulation.

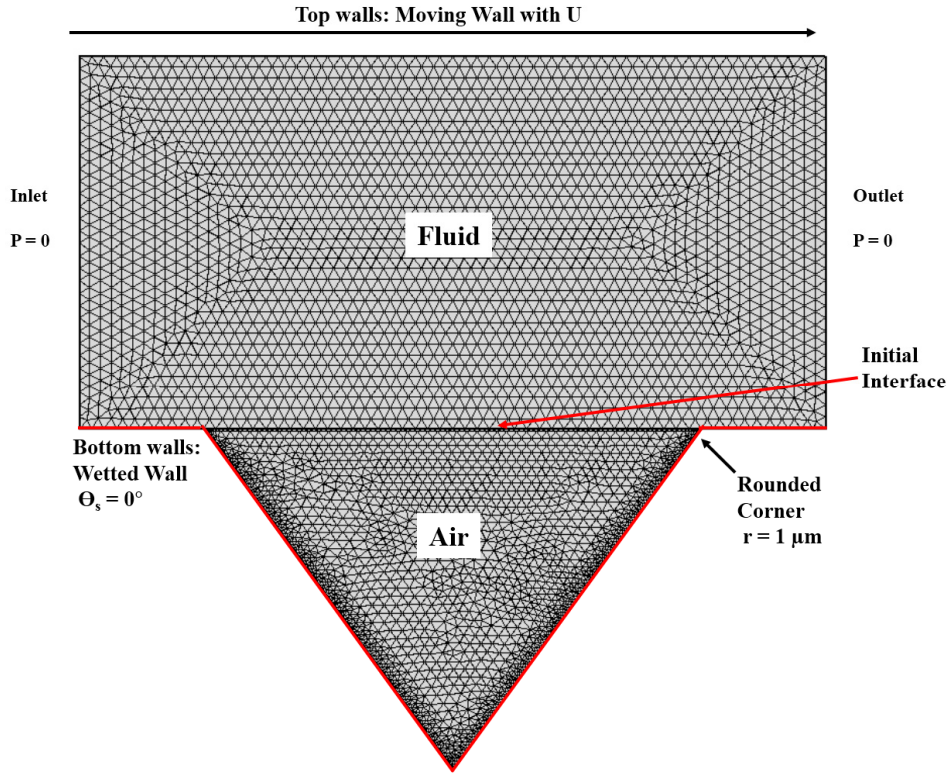

Figure 4.8 3D simulation model setup for air bubble deformation

4.5 Discussion

Figure 4.4a and Figure 4.4b show that filling at low capillary number depends on the releasing of the contact line from the front edge and the movement of the contact line on the cell faces, thus displacing air. If the releasing process happens before the side contact lines reach the back of the cell, the filling process tends to be complete. This releasing process depends on the dynamic contact angle at the front cell edge as stated by Gibbs [11] and demonstrated experimentally by Oliver [12]. As shown in Figure 3a, this releasing process happens around t*=0.443. The first simulation is designed to study a completely filling case, where Ca is small and liquid can fully displace air from the cell. The simulation setup is shown in Figure 4.7. A small cell edge rounded with a radius of 1 µm was used to emphasize the pinning effect seen in experiments and to avoid divergence issues during simulation. Figure 4.9 shows a simulation result at Ca ≈ 0.05 across a 100-µm cell. In the top row side view, 0.010 m^2/s silicone oil (black) displaces the air (white) from left to right. When the moving contact line reaches the front edge, its moving speed is

decreased, showing a pinning effect similar to theoretical predictions and the above experimental results. When the dynamic contact angle becomes large enough, the contact line is released from the front cell edge, similar to Figure 4.4a from t*=0.143 to 0.593. Then the contact line slowly moves to the bottom of the cell and it quickly climbs up along the back cell face, moving out from the cell, completely displacing the air with liquid. The isosurface in Figure 4.9 shows the interface deformation when the contact line moves across the cell. At t* = 0, the contact line pins at the front edge, but moves further along the side edges. While the inner contact line is released and moves down the front cell face, the outer line moves faster at the side edge (t* = 0.15 to 0.60). Starting from t* = 0.75, the inner contact line climbs up along the right cell face and finally joins the outer contact line, relaxing back to the equilibrium position. Because the center contact line can catch up with the side contact line in the simulation, the simulation results do not produce the capillary breakup as observed in our experiments and shown in Figure 4.4b. The overall filling time is also approximately two times larger than the experimental result in Figure 4.4a. We also observed that the side contact line moves much slower in our simulation, which can extend the filling time as well. The origin of these temporal discrepancies is unknown; however, despite the overall discrepancy in the timing of the observed events, the simulations are still found to be qualitatively descriptive of observed experimental phenomena. Overall, there is good qualitative agreement between the simulations and the experimental observations, despite the time scales being different.

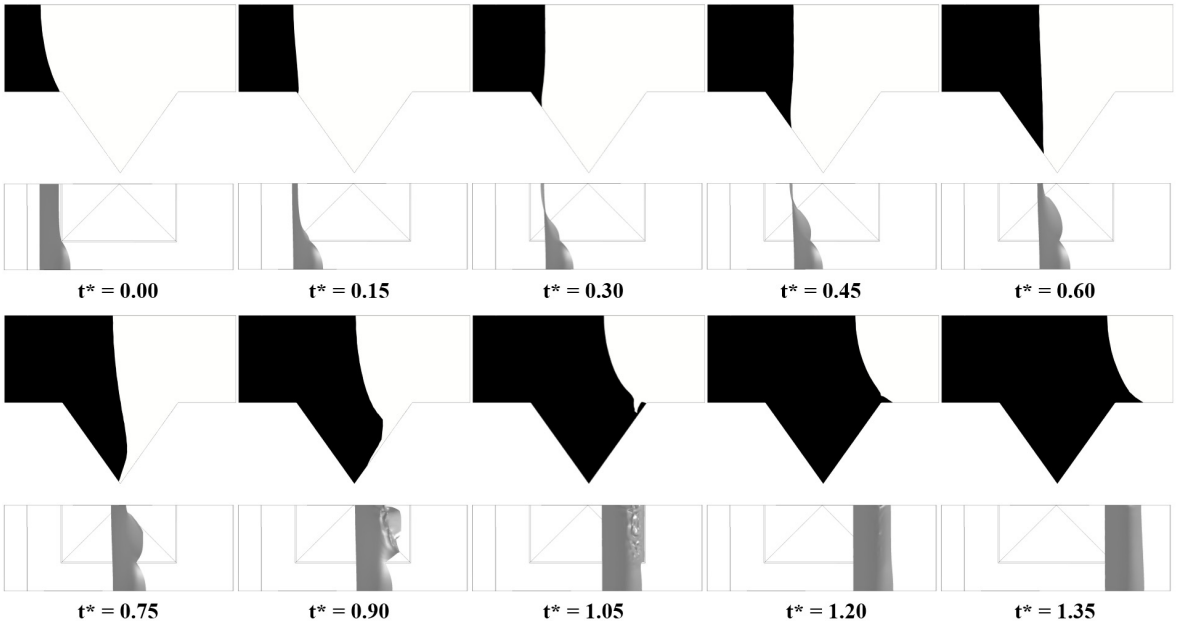

Figure 4.9 3D simulation of a completely filled cell. At each time step, a 2D center-cut plot (top row) shows the air-liquid interface movement from the side view and a 3D plot with isosurface shows the interface movement across the cell in 3D. Black and white regions represent 0.010 m^2/s silicone oil and air phases, respectively.

For unfilled cases, the simulation is more challenging because of the significant deformation of the interface and the rapid closing effect on the back cell edge discussed earlier. This prevents a full simulation of the unfilled case using the above methodology (i.e., with a flow field transiting over the cell). However, in accordance with the experimental results at high Ca, it is a good assumption to start with a complete unfilled cell and study the interface deformation of an air bubble, which is shown in Figure 4.4c. In this scenario, the fluid has completely covered the cell and trapped an air bubble; the bubble subsequently deforms. We simulate how the entrapped air deforms right after the contact line leaves the back cell edge and relaxes back to its equilibrium position. The 3D simulation is presented in Figure 4.10, starting from the case where the cell is filled fully with air. The details of the simulation are provided in Figure 4.8. The same wetted wall boundary conditions with an imposed static contact angle of $\theta_s = 0°$ is applied at the bottom boundaries and at the cell faces. To best match the simulation model with the experimental results, the same liquid viscosity as well as shear rate above the air-liquid interface of the trapped air are applied. The shear rate is calculated by dividing the speed of dipping substrate by the distance between the substrate and the wall of container, based on a Couette flow developed between a substrate and wall container. In the simulation model, the shear rate is simulated by imposing a moving plane on the top boundary. In the simulation shown in Figure 4.10, we simulated the air bubble deformation that occurred in the experiment at Ca = 2 with silicone oil kinematic viscosity of 0.100 m^2/s. A shear rate of about 0.0162 s^{-1} is applied to the model to match the experimental shear rate of about 0.016 s^{-1}. Comparing the model with the experimental results, we observe qualitatively similar behavior, though again, there are discrepancies with respect to the specific timing. Specifically, both experiments and simulations show that the fluid advances faster at the cell wedges than at the cell faces. This is expected based on capillary flow considerations at the wedges. The deformation of the air bubble observed in the experiments can be explained by the simulation model as well. The entrapped air is gradually deforming into a dome shape and stays at the center of the cell, causing the “shrinking” seen from the top view as show in Figure 4.4c at t*=2.2 to 3.4. Note that in Figure 4.4c, the liquid advances faster from the front edge than from the back edge during the air bubble deformation. This is because the contact line pins at the front edge and moves down the cell wall first. This is not included in the simulation, since we start the simulation with both the front and back edges fully covered.

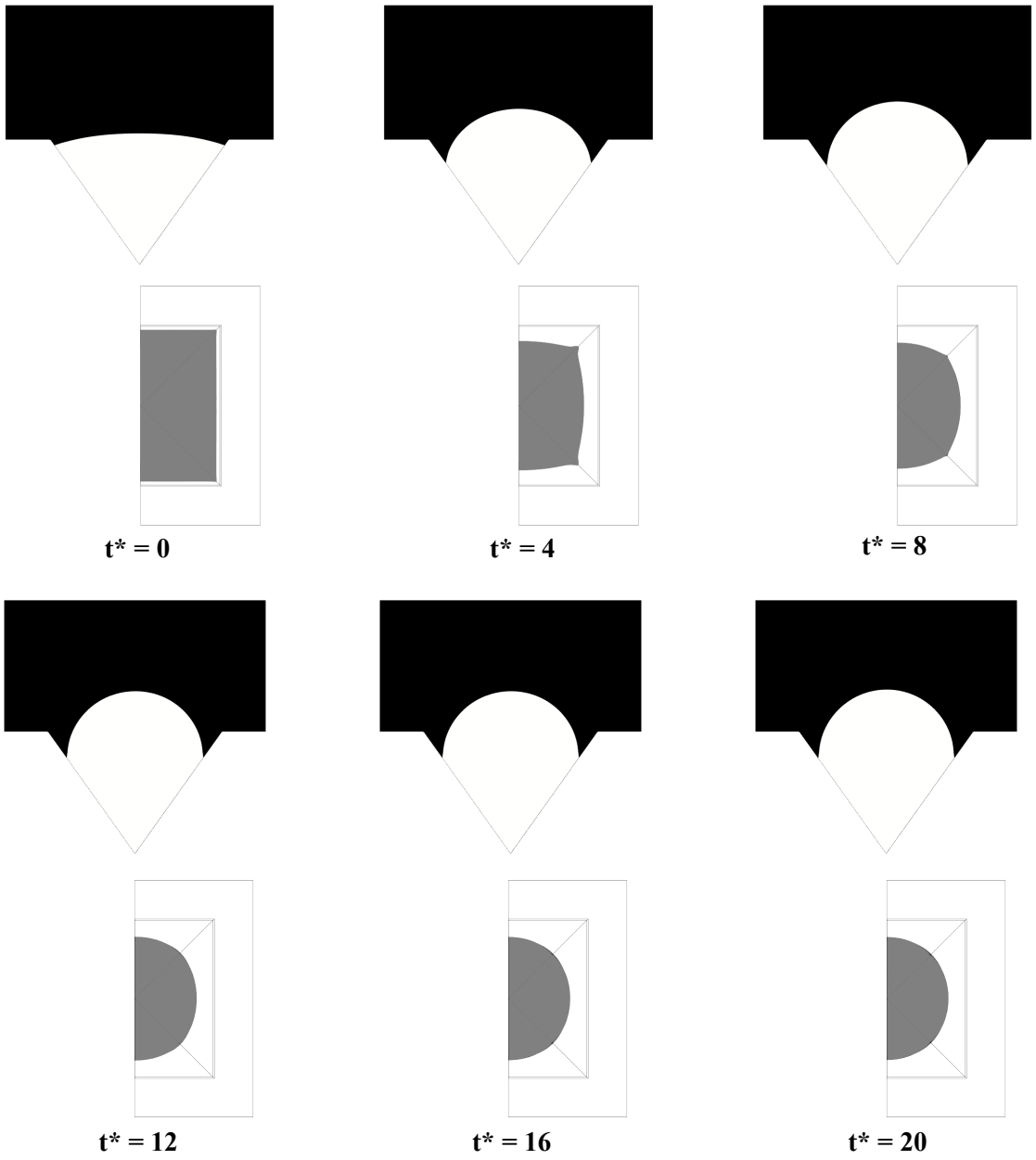

Figure 4.10 3D simulation model for air entrapment deformation at Ca= 2 including side view and top view. The air interface is represented by an isosurface. Air is fully filled in the cell and fluid occupies the volume above the air interface. The kinematic viscosity is 0.100 m^2/s.

In addition to the numerical simulation, the deformation of the interface of entrapped air can be simply explained as follows. For simplicity, we assume maximum air entrapment initially. In the experiment, since the contact lines are pinned at the cell edges then moves down the cell faces, the contact line speed becomes small and the contact angle is reduced to its static contact angle, which is <15° in our cases. Based on the experimental results, in the simplified simulation model

the initial contact angle at the cell face is larger than the equilibrium contact angle, therefore the contact line advances toward the bottom of the cell to decrease it. During the process of decreasing contact angle, the mean curvature also changes its sign. According to the Young-Laplace equation, the pressure inside (P_{inside}) the air bubble is larger than the pressure far away from the interface ($P_{outside}$), creating a pressure gradient, which can be seen from the simulation results shown in Figure 4.11. This pressure gradient prevents the contact line from rapidly moving toward the bottom of cell. This explain our experimental results in Figure 4.4c, where the air bubble quickly deforms at the beginning and slows down afterward.

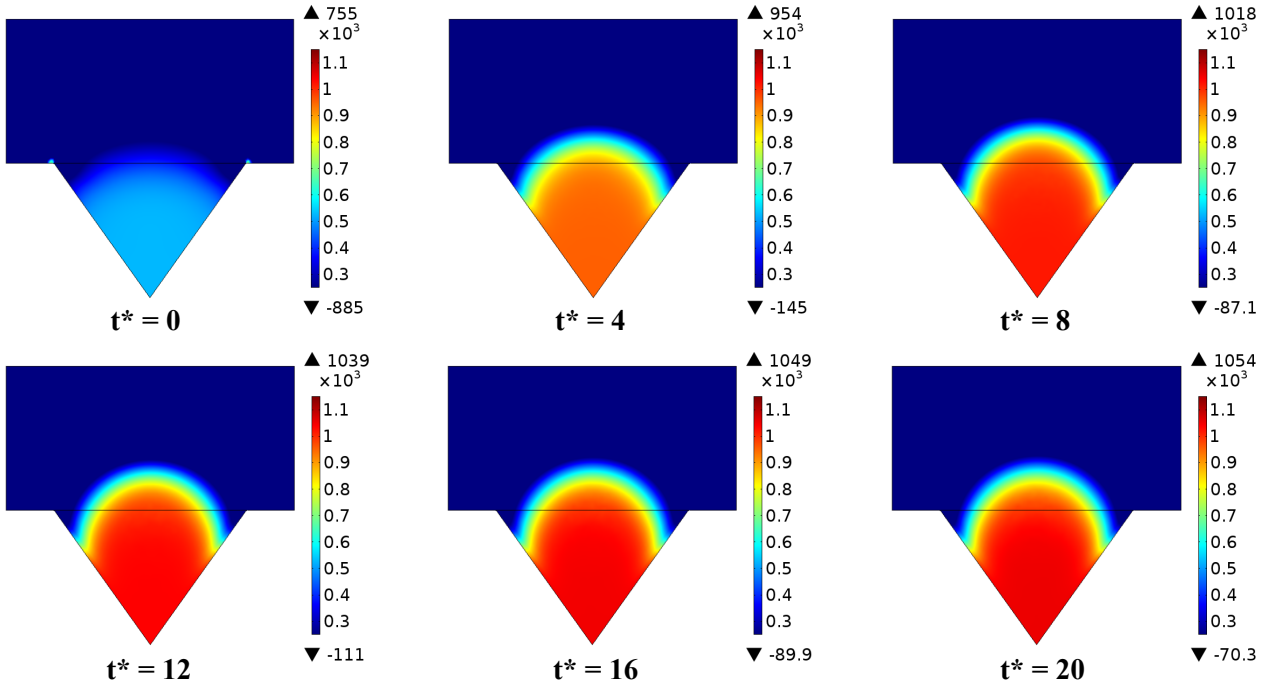

Figure 4.11 Pressure development during the air entrapment deformation. Air pressure increases as the interface deforms from a flat to a dome-like interface. The high-pressure points at the corners appear to be a simulation artifact.

Based on our experimental and simulation results, we now propose a technique to enhance the filling process for high-speed gravure printing. At high capillary number, air is fully trapped, but it deforms quickly right after air entrapment, exposing a dome shape above the substrate surface. By applying appropriate shear rates above the liquid-air interface, the air bubble can be forced out of the cell. We confirm this hypothesis using the 3D simulation discussed earlier with various shear rates. The kinematic viscosity is chosen to be about 0.001 m^2/s in this simulation in order to reduce overall simulation time. An example of shear-rate assisted filling is illustrated in Figure 4.12a. The top wall moving from left to right creates an averaged shear rate of 260 s^{-1} above the air interface. The air is forced out from the cell while the interface is experiencing deformation. Eventually, the air bubble is displaced by the fluid and moved to the back side; it is ultimately pushed out of the cell. Various simulations with different shear rates have been examined. The results in Figure 4.12b show that with increased shear rate, the air bubble will be displaced from

the cell more rapidly. The shear rate can be applied in a real system by introducing a small gap between the roll surface and a stationary wall such as a post-filling blade. We suggest therefore that this represents a possible method to enhance the filling process in high speed gravure printing. In other words, the results herein provide guidance for design of doctor blade systems for use in highly-scaled gravure; use of a double blade, with a gap-inducing post-filling blade followed by a wiping blade may allow for optimized filling and wiping. More generally, of course, the overall set of experimental and simulation results also show the effect of cell geometry on filling. Use of shallow cell geometries with corner fillets can work to enhance filling, since these conditions will extend the range of capillary numbers over which air entrapment is avoided. Given that air entrapment places a fundamental limit on cell filling, this study thus provided insight into how to extend the capabilities of gravure printing.

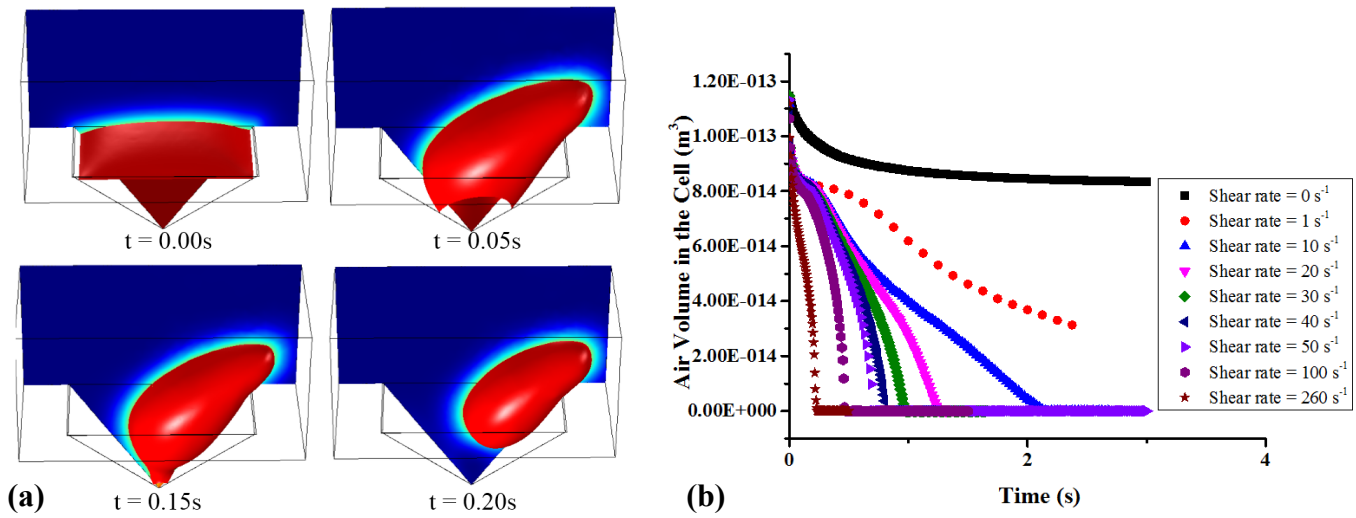

Figure 4.12 a) Air entrapment deformation under effect of flow with shear rate of 260 s^{-1}. Air is forced out from the cell while deforming. b) Air volume in the cell vs. time at increasing shear rate. The kinematic viscosity used is about 0.001 m^2/s. Increased applied shear rate forces the air out from the cell more rapidly.

4.6 Conclusions

In this chapter, for the first time, we report on detailed experimental results and simulations of the filling process in highly-scaled gravure printing, particularly focusing on the technologically vital regime with capillary number larger than 0.07. The experimental results reveal that contact line pinning at the cell edges and interface deformation over the cell opening causes air entrapment, i.e. filling failures. Our results suggest that the filling process strongly depends on the capillary number and the filling process of different cell sizes are similar when compared at the same dimensionless time. At high capillary number, the filling process fails and air bubbles are trapped. The interface of the air bubble quickly deforms to a dome-shape to minimize overall surface energy. Furthermore, various filling regimes can be defined based on experimental results. Complete filling can be expected when the capillary number is below 0.1; higher

capillary numbers produce successively worse filling, with complete air entrapment ultimately occurring at high capillary numbers. Moreover, we also posit based on simulation that it is possible to introduce an appropriate shear effect to completely eliminate trapped air. More generally, because the contact line pinning limits the filling process, a shallow cell geometry and fillet edges should be used in highly-scaled gravure printing. These are important strategies to enhance the filling process for high speed printing.

4.7 References

[1] J. Cen, R. Kitsomboonloha, and V. Subramanian, "Cell Filling in Gravure Printing for Printed Electronics," *Langmuir*, no. In preparation.

[2] R. Kitsomboonloha, S. J. S. Morris, X. Rong, and V. Subramanian, "Femtoliter-scale patterning by high-speed, highly scaled inverse gravure printing.," *Langmuir*, vol. 28, no. 48, pp. 16711–23, Dec. 2012.

[3] R. Kitsomboonloha and V. Subramanian, "Lubrication-related residue as a fundamental process scaling limit to gravure printed electronics.," *Langmuir*, vol. 30, no. 12, pp. 3612–24, Apr. 2014.

[4] S. Dodds, "Stretching and Slipping Liquid Bridges : Liquid Transfer in Industrial Printing by," University of Minnesota, 2011.

[5] A. K. Sankaran and J. P. Rothstein, "Effect of viscoelasticity on liquid transfer during gravure printing," *J. Nonnewton. Fluid Mech.*, vol. 175–176, no. March, pp. 64–75, May 2012.

[6] D. Soltman and V. Subramanian, "Inkjet-printed line morphologies and temperature control of the coffee ring effect.," *Langmuir*, vol. 24, no. 5, pp. 2224–31, Mar. 2008.

[7] H. Kang, D. Soltman, and V. Subramanian, "Hydrostatic optimization of inkjet-printed films.," *Langmuir*, vol. 26, no. 13, pp. 11568–73, Jul. 2010.

[8] P. C. DUINEVELD, "The stability of ink-jet printed lines of liquid with zero receding contact angle on a homogeneous substrate," *J. Fluid Mech.*, vol. 477, no. -1, pp. 175–200, Mar. 2003.

[9] J. Stringer and B. Derby, "Formation and stability of lines produced by inkjet printing.," *Langmuir*, vol. 26, no. 12, pp. 10365–72, Jun. 2010.

[10] A. Darhuber, S. Troian, and S. Miller, "Morphology of liquid microstructures on chemically patterned surfaces," *J. Appl.*, vol. 87, no. 11, p. 7768, 2000.

[11] J. Gibbs, H. Bumstead, and W. Longley, "The collected works of J. Willard Gibbs," 1928.

[12] J. Oliver, C. Huh, and S. Mason, “Resistance to spreading of liquids by sharp edges,” *J. Colloid Interface Sci.*, vol. 59, no. 3, pp. 568–581, 1977.

[13] T. Ondarçuhu and A. Piednoir, “Pinning of a contact line on nanometric steps during the dewetting of a terraced substrate.,” *Nano Lett.*, vol. 5, no. 9, pp. 1744–50, Sep. 2005.

[14] S. G. Bankoff, “Entrapment of gas in the spreading of a liquid over a rough surface,” *AIChE J.*, vol. 4, no. 1, pp. 24–26, Mar. 1958.

[15] S. Reddy, P. R. Schunk, and R. T. Bonnecaze, “Dynamics of low capillary number interfaces moving through sharp features,” *Phys. Fluids*, vol. 17, no. 12, p. 122104, 2005.

[16] J. M. Brethour and H. Benkreira, “Filling and Emptying of Gravure Cells – Experiment and CFD Comparison,” *11th Int. Coat. Sci. Technol. Symp.*, 2002.

[17] R. Hoffman, “A study of the advancing interface. I. Interface shape in liquid?gas systems,” *J. Colloid Interface Sci.*, vol. 50, no. 2, pp. 228–241, Feb. 1975.

[18] H. Kang, R. Kitsomboonloha, J. Jang, and V. Subramanian, “High-performance printed transistors realized using femtoliter gravure-printed sub-10 μm metallic nanoparticle patterns and highly uniform polymer dielectric and semiconductor layers.,” *Adv. Mater.*, vol. 24, no. 22, pp. 3065–9, Jun. 2012.

[19] “Multiphase Flow Modelling,” in *COMSOL Multiphysics CFD Module Users Guide V4.1*, 2010.

Chapter 5 High-Resolution Gravure Roll Fabrication

In previous chapters, the physics and challenges of scaling gravure printing are discussed thoroughly. The effects of ink properties, particularly surface tension and viscosity, are explained in chapter 2. The aspects of doctor blades such as blade geometry and wettability are discussed in chapters 2 and 3. Chapter 4 explains the filling process. However, the remaining challenge is to integrate this knowledge and fabricate a high-resolution gravure roll. In gravure printing, patterns are constructed by using grooves (also known as intaligo) and cells. Cell-based patterns pose an advantage for optimization, since they can be considered as a basic building block of patterns. By doing so, the patterns can be optimized in stages, namely cells, arrays of cells and patterns. In this chapter, we will try to redesign gravure cells from the ground up. First of all, the status of current engraving technologies is reviewed to summarize current cell geometries available and their shortcomings. Then, the effects of cell opening shapes and profiles will be examined, because cell geometry controls microscale flows of inks during printing processes. Standard lithography and etching processes were used to fabricate the different cell geometries on printing plates. These printing plates were used to optimize cell geometry for the best printing performance. After that, a simple roll fabrication process is proposed. The process leads to several advantages over conventional engraving methods. The advantages are as follows: 1) small cell and gap features, which is necessary for increasing printing resolution; 2) arbitrary cell arrangement, which is important for pattern optimization in high resolution printing; 3) smooth surface finishing, which is critical for minimizing residue films.

5.1 Current Engraving Technologies

Typically, a gravure roll consists of three layers; base core, engraving, and hard layers. The base core is typically made of steel to provide low-cost, machinability and rigidity. The cores can be sleeve-cylinder, in which the shaft is removable, or integral shaft cylinder. A sleeve cylinder provides lighter weight, but is mechanically less accurate. An integral shaft cylinder is normally used for precision printing, but it is more expensive. After the core is machined and polished to the desired dimensions, an engraving layer, normally a copper layer, is deposited by an electroplating process. This engraving layer is 150-250 μm thick. After electroplating, the copper surface is polished down to the designed dimension and surface roughness. This is crucial for the subsequent step, engraving, which requires a smooth surface for reliable operation. The engraved cell is formed on this copper layer and never reaches the steel core. After engraving, the roll is cleaned and a hard layer is deposited by electroplating. Chrome is the current material of choice because it provides a hard, low friction surface. The chrome layer is typically 6 μm thick, this is enough to provide a robust gravure roll surface. Another unique feature of the chrome layer is chrome cracks. During chrome electroplating, internal stress is built up and relaxes once a critical thickness is reached. These cracks create lubricated micro channels on roll surfaces that prolongs life time of the gravure roll and doctor blade. Normally the current density of electroplating is varied such that the density of chrome cracks is at least 150 cracks per cm [1]. Finally, the gravure roll is polished to gain smooth roll surfaces. Generally, gravure rolls are expensive and the cost of the core is a substantial factor of the total cost. In order to reuse the

steel core, a technique called the *Ballard shell* is sometimes used instead of the base copper technology described above. The idea of the Ballard shell is to plate a thin engraving copper layer non-adhesively to the base copper. This allows the engraving copper and chrome layers to be removed easily from the core when needed. The challenge of this technology is to optimize the adhesion of the Ballard shell such that it can be engraved and prints consistently, but can be stripped off later on.

The three main engraving technologies for forming gravure rolls are electromechanical, direct laser and indirect laser engravings. These engraving techniques aim to produce three dimensional structures below gravure roll surfaces in order to control ink volume per unit area, i.e. film thicknesses. Usually, the cell depth and cell density are varied to control final film thicknesses. Direct laser engraving uses a high power laser to ablate material from the roll surface, instead of mechanical removing. The laser pulses are controlled digitally by a computer. In indirect laser engraving, a lower power laser is used to pattern a mask resist and then isotropic wet etching is used to form recessed cells. To fabricate high resolution rolls using direct/indirect laser engraving, multiple issues must be addressed. The resolution of laser engraving relies on the spot size of the laser beam. It is possible to create a sub-micron spot size on a planar surface, but directly focusing on a curved, large area surface turns out to be much more challenging. Metal ablation requires high power and tends to create rough cell edges (known as burrs) and walls and widened cells. Indirect laser engraving suffers from an undercutting of the mask layer due to the isotropic wet etching process. To minimize the power requirement and defect density related to ablation, Daetwyler developed a new direct laser system (DLS). This technique uses electroplated zinc with organic additives, instead of copper, to reduce heat transfer and maximize ablation effects. Because Zinc can be ablated and vaporized, the cell size is smaller and burrs are reduced to 2-3 μm around the cell. Cell volume is adjusted by controlling the pulse energy of the laser. Due to the nature of the laser spot, only circular cells are possible. However, laser spots can be manipulated easily without mechanical constraint as in electromechanical engraving. Other cell opening shapes are possible by combining circular cells at the expense of increasing cell sizes. Another advantage of laser engraving is that it is a non-contact tool and wearing is not a concerns. The cell size can be adjusted by zoom optics as well. Figure 5.1 shows engraved cells fabricated by DLS. By tuning the laser intensity, several cell profiles can be obtained. There is a weak effect on cell size and depth due to the ablation and steep side walls are produced with various bottom topographies. The smallest cell size was 28 μm [2].

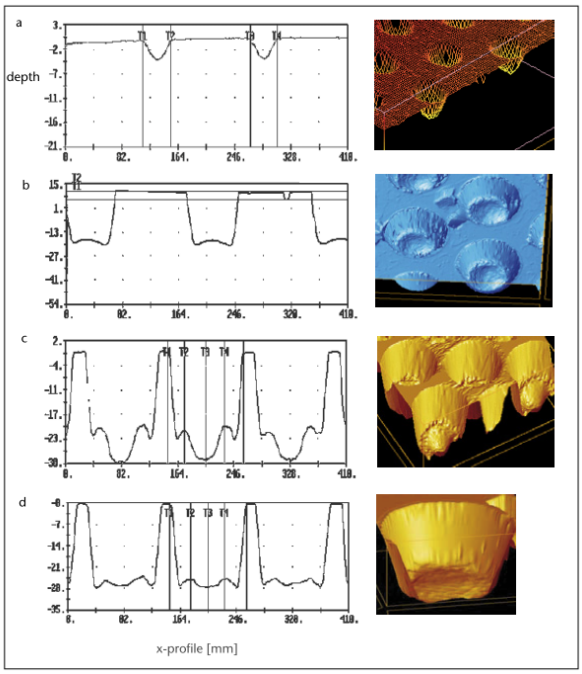

Figure 5.1 Example of engraved cells by direct laser engraving. By adjusting laser ablation, several cell profiles can be generated such as dome, top-hat, and bottom-ring (from top to bottom). Reproduced from [3].

Electromechanical (EM) engraving is a mechanical cutting technique that uses a diamond stylus and computer-controlled stages to engrave into roll surfaces as illustrated in Figure 5.2a. As a roll rotates, a diamond stylus moves in and out of the roll surface synchronously. When the stylus moves below the roll surface, it removes copper material, creating recessed cells. To simplify mechanical motions, EM engraving normally uses a constant screen number and angle as shown on Figure 5.2b to define the location of each cell and density of cells per unit area. Due to the shape of the diamond stylus, screen number, and angle, EM engraving produces only diamond-like shapes. During the engraving, only the cutting depth of the stylus is digitally controlled to adjust cell volume. Figure 5.2c demonstrates EM patterns with varied cell volume from 100% to 20% cells. Because the positions of cells are fixed, the cell gap is enlarged as the cell volume is reduced due to mechanical constraint. This technique is used to create a halftone feature in graphic arts, where color intensity is adjusted by ink volume per unit area. However, in printed electronics this constraint is undesirable. Patterned uniform films are essential for fabricating electronics devices and any voids in the print pattern resulting fromcell gaps are considered as defects. Figure 5.2d shows optical microscope images of EM-engraved cells with cell depths varied from 45 to 30 μm, highlighting the dependency of cell gap on opening size. The image also provides a sense of surface roughness on the non-patterned area.

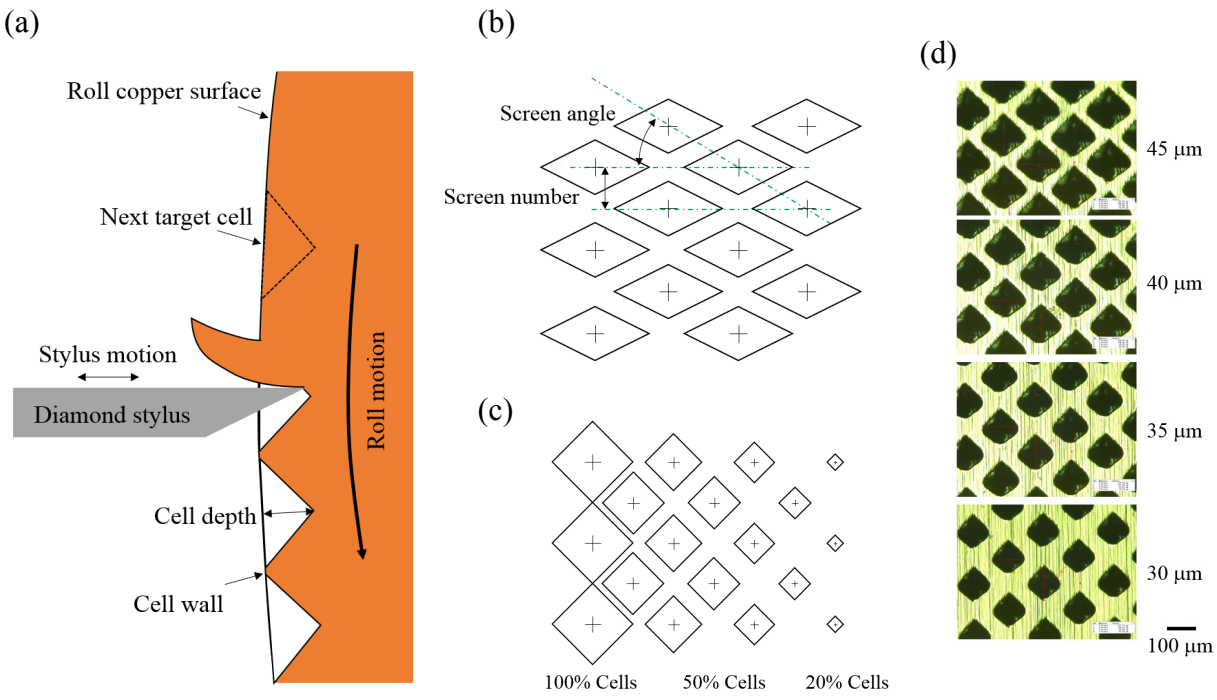

Figure 5.2 (a) principle of electromechanical (EM) engraving technique (b) definitions of screen number and angle that are used to specify cell locations. The screen angle is 30° in this case. (c) Various cell volumes in the EM engraving used to control ink volume per unit area. (d) Optical images of EM cells and roll surfaces. The screen number and angle are 70 line/cm and 53°. (a-c) after [1].

Although modern engravers can satisfy resolution requirements for the graphic arts industry (minimum features ~10 µm), they cannot truly fulfill the requirements for printing high-performance electronic devices. There are several attempts to meet this demand. For example, the Microstar MicroEngraving System developed by Daetwyler can engrave cell sizes of 5 µm with cell gaps of 2.5 µm [4]. In this extreme EM gravuring, the cell shape is a rounded square. The pattern is created by arranging square cells into arrays or strings. Due to currently restricted mechanical capabilities, the arrangement of cells is limited and cell sizes must be uniform over certain areas. In addition to Microstar engraving, extreme EM engraving is an on-going research topic. Figure 5.3a shows an example of such extreme engraving by Daetwyler, where the defined cell size and cell gap is 2.5 and 2.0 µm. The system successfully engraved cells, but repeatability of patterns and surface finishing become limiting factors of this engraving technology. Moreover, Figure 5.3b and c show chrome crack features on a gravure roll and the poor surface roughness of extreme EM engraving. A polishing step after chrome plating was omitted in this roll process, because of the limitations of current polishing technology. Sub-5µm cells are polished away by conventional polishing processes. Chrome cracks and poor surface finishing represent fundamental limits to current EM engraving to achieve high-resolution printing due to large lubrication film residues.

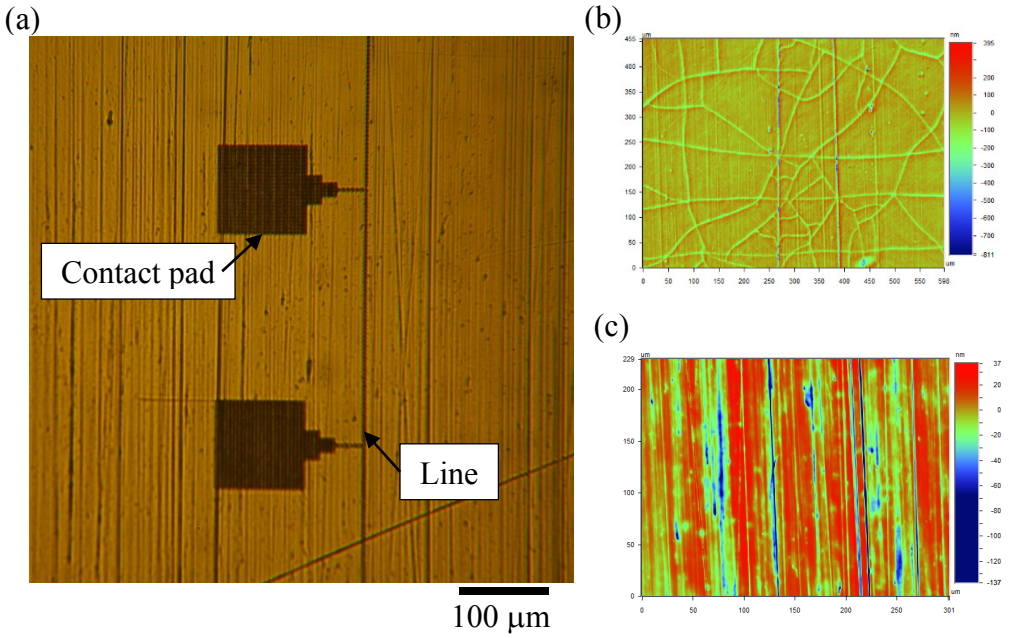

Figure 5.3 Image of extreme EM engraving. The defined cell size and gap are 2.5 and 2.0 μm, respectively. The image shows two contact pads connect to a line from its side. One can also observe poor surface finishing, where scratches are of similar size as engraved patterns. (b) Surface topography showing chrome crack features. (b) Magnified surface topography showing surface roughness of extreme engraved roll. The final chrome polishing step is skipped to preserve sub-5μm cells.

In order to realize high-resolution gravure printing, a new high-resolution roll engraving must be established. First, standard microfabrication on silicon wafers will be used to fabricate gravure cells, i.e. “engraving”, because it is a well-established technique that can precisely fabricate features down to nanometers. Then, effects of cell formation by dry and wet etching will be discussed. Next, effects of cell geometry and arrangement on printing performance will be considered. Finally, a roll fabrication based on a thin metal sheet wrapped around a magnetic roll will be demonstrated along with corresponding printed results.

5.2 Cell formations on silicon wafers

Fundamentally, cell formation is a process that etches materials below a flat surface. This is simply an etching process in microfabrication. Etching processes can be performed using wet and dry etching. Wet etching uses etching solutions that chemically react with target materials to remove material. On the one hand wet etching is typically isotropic due to the uniformity of chemical reactions. However, anisotropic wet etching is possible on crystal substrates, where etching rates depend on crystal planes. On the other hand, dry etching uses gases and plasma to activate etching processes. Directional etching is gained by increasing physical bombardment with reactive ions. This is crucial for etching single micron features.

To fabricate gravure cells, a thick silicon oxide thermally grown on a 100 silicon wafer was used as a hard mask. This hard mask is necessary to preserve patterns during etching processes, because photoresists can be easily altered and damaged during etching. The patterns were transferred into a photoresist by using a deep UV stepper (ASML 5500/300), and then to the hard mask by dry etching (Lam Rainbow etcher) using CHF_3 and CF_4. Dry etching provides good pattern fidelity during the etching process. The opening in the oxide defines the opening of gravure cells. After that, dry and wet etching of silicon can be performed to create various cell geometries. Figure 5.4a and b show top-views of gravure cells fabricated by uniform dry etching and anisotropic wet etching. Both methods preserved opening dimensions very well. Dry etching ensures uniformly etched silicon. Figure 5.4c shows cross sections of various cell sizes fabricated by dry etching. This allows the fabrication of arbitrary cell shapes. The cell depth is controlled by etching time for all cell sizes. However, when the opening is smaller than 2 μm, the opening size affects the etching rate and the etching rate is reduced. Figure 5.4d shows the detailed cross section of a dry-etched cell. The cell wall is roughened and the edges of the bottom surface are trenched. This phenomenon is called microtrenching, which is a result of the reflection of energetic ions from side walls [5]. Because the cell depth is a constant, cell volume per unit area can be controlled by reducing the number of cells per unit area and/or cells sizes as illustrated in Figure 5.4e. The side wall angle was ~80° and there is a slight undercut below the hard mask. To engrave cells by using wet etching, samples were dipped into 33 wt% potassium hydroxide solution at 80 °C. This etching process results in perfect 54.7° inclining walls and only square or rectangle opening shapes due to the crystal orientation of 100 silicon wafers. This process is a self-limiting process and is capable of correcting pattern errors on the hard mask layer. For example, a 1-μm cell is transferred to the hard mask as a circle instead of a square due to resolution limits of the lithography and etching processes. But during the anisotropic wet etching process, the opening will undercut the hard mask and automatically stop when a square opening is achieved. Moreover, anisotropic wet etching can fabricate different cell depths by controlling the opening size as shown in Figure 5.4e. This allows the cell volume to be adjusted independently from the cell gap.

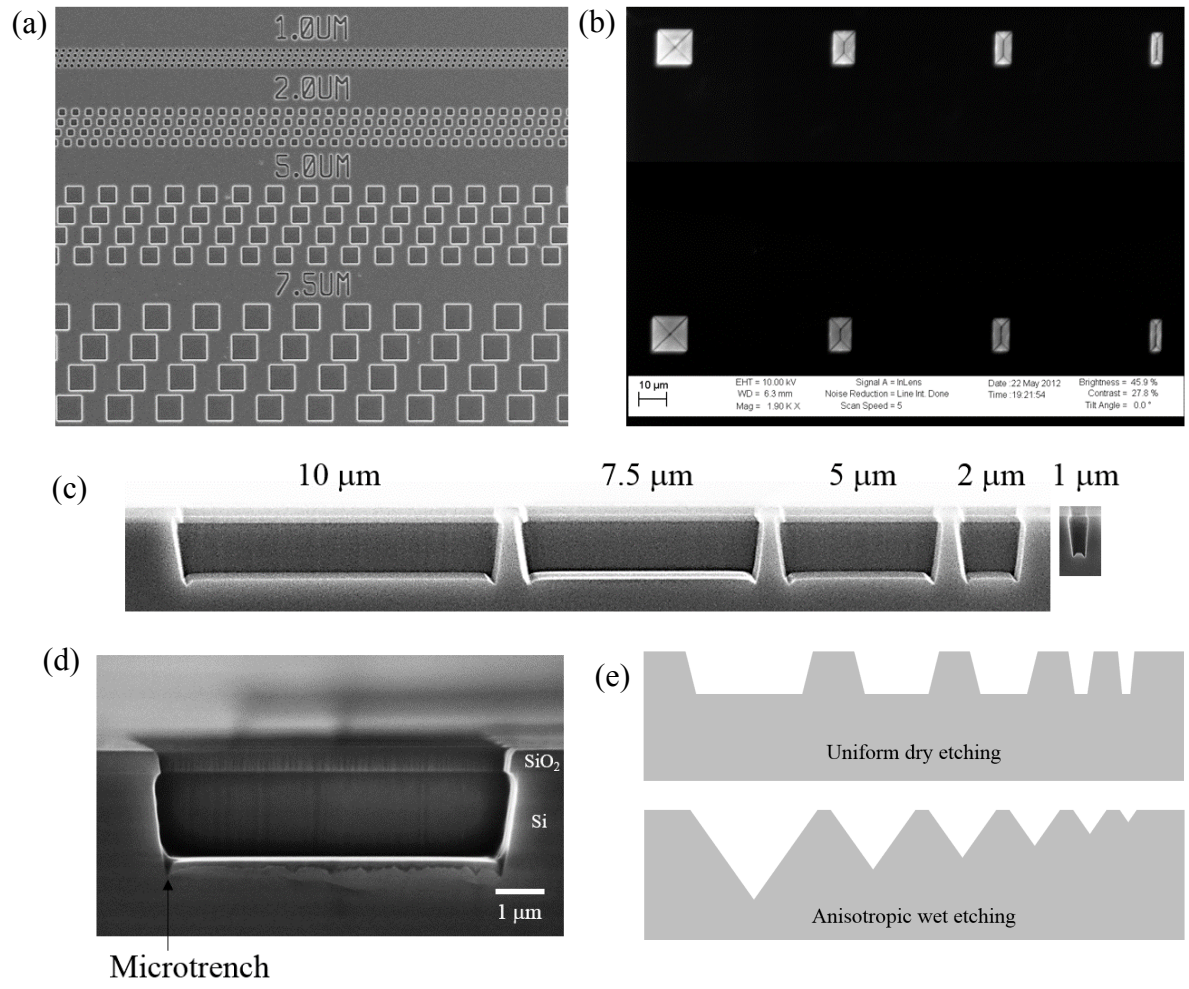

Figure 5.4 Cell profiles engraved by (a) uniform dry and (b) anisotropic wet etching. (b) lines inside cells show an intersection between crystal planes. (c) cross sections of engraved cells by dry etching. (d) zoom in of drying etched cell, highlighting microtrench and rough surfaces. (e) a comparison of cell profiles between uniform dry etching and anisotropic wet etching, highlighting how cell volume can be varied by each method. Uniform dry etching requires increased cell spacing to decrease cell volume per unit area. Anisotropic wet etching inherently creates multiple depths by simply varying cell width.

In addition to defining cell geometries, the cell gap is a crucial dimension as well. In cell based patterns, each cell prints individual dots and then they merge and form designed patterns during the ink spreading process. To form a uniform patterned film for electronic devices, cell gaps, which are considered as defective areas, should be minimized as much as possible. Therefore, the capability of fabricating narrow gaps is essential. Figure 5.5 shows the smallest gap defined by the lithography tools used herein, 0.25 µm. With other microfabrication techniques like etching, the feature size can be reduced further as shown in Figure 5.5b. The undercutting during dry etching can reduce cell gaps down to 50 nm. The fundamental limitation on the downscaling

of cell gaps is the mechanical stability of cell walls during printing. Nanometric thin cell walls can be broken during the printing process due to the significant shear forces.

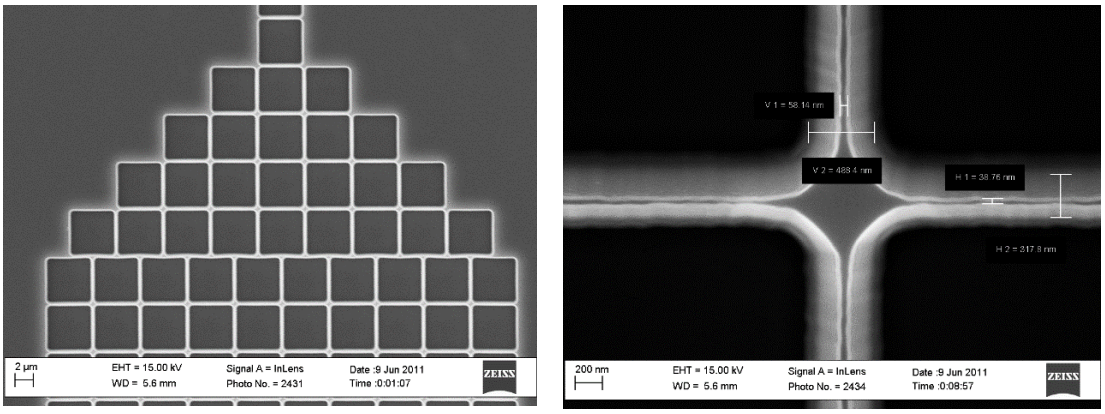

Figure 5.5 Critical dimension of fabrication: cell wall. With dry etching cell walls as small as 50 nm can be fabricated by controlling the lateral etching rate.

As explained earlier, various cell geometries can be fabricated by microfabrication, depending on the opening shapes defined by lithography, and etching methods. The cell geometry here refers to cell opening shape, cell wall slope, and cell bottom. In the next section, we will address each parameter and attempt to find the best cell geometry for high resolution gravure printing.

5.3 Cell opening shapes

Various cell opening shapes are examined in order to find the best performing cell opening shapes. This study focuses on both conventional shapes and innovative shapes. The conventional shapes are diamond, square, rectangle, which resemble cells engraved by electromechanical engraving, circle and hexagon, which represent direct and indirect laser engraving. The innovative shapes are triangles, zigzag and jigsaw. These various cell opening shapes were fabricated by dry etching because of its directional etching. Figure 5.6 shows drawings of the tested cell opening shapes, which are square, rectangle, diamond, triangle, zigzag, jigsaw, circle, and hexagon, from left to right and top to bottom respectively. Each drawing is associated with its representative printed result below. The ink was a polymer solution, PVP in PGMEA of 21.4 wt% and substrates were PET. Features were printed by using inverse direct gravure at a printing speed of 1 m/s. Blade pressure and angle were 15 psi and 70°. The printed results were measured by using an interferometer. Black spots in interformetry images are caused by a large gradient of film thickness. This indicates the profile of printed films cannot be resolved due to limited resolution. The printing direction is from top to bottom of the figure. Interestingly, regardless of cell opening shape, the cell corners always print a small amount of material onto the substrate. However, only square, rough square, jigsaw, circle and hexagon can print over the entire edges. Rectangles show very interesting behaviour. Printed features can only be observed on the short edges and the length of printed features is approximately equal to the length of the short edge. Printed dots look like squares. As the short edge is shortened, this length is also reduced proportionally as shown in Figure 5.6 top row from left to right. The rotation of rectangles with

respect to the printing direction does not alter this relationship. Because of defective areas at the center of rectangles, these cell opening shapes are suitable as a building block for high-resolution patterns. In the cases of diamonds and triangles, they only printed from the corners, even though they have edges with the same length as square and rectangle. For symmetrical shapes, which are zigzag, jigsaw, circle and hexagon, printed dots resemble the designed shapes. These suggest that square, zigzag, jigsaw, circle and hexagon have better overall printing performance. Since the goal is to find the best cell opening shape for high-resolution gravure printing, these cells will be examined further as a function of cell size next.

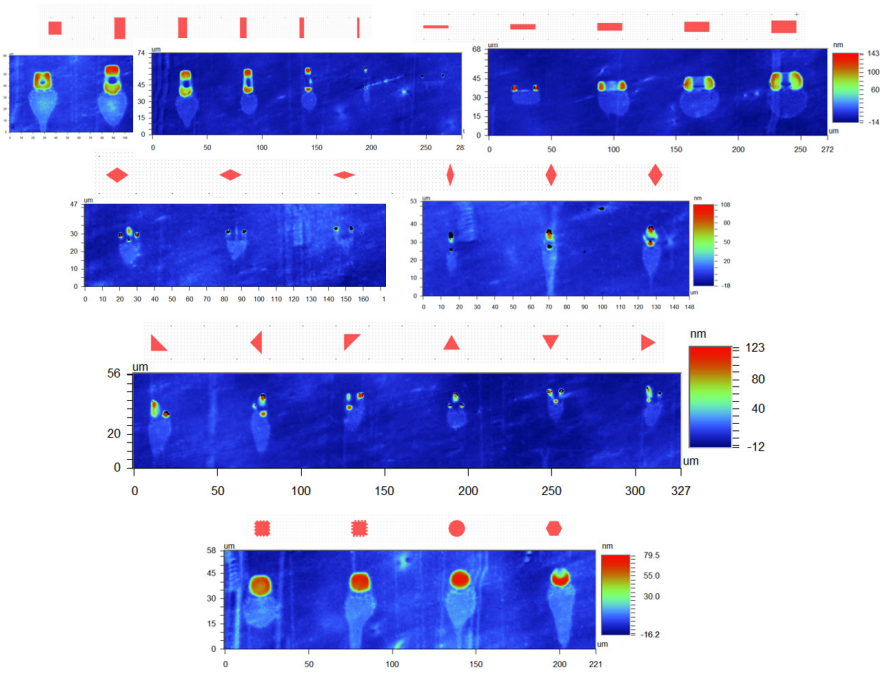

Figure 5.6 A comparison of designed and printed cell shapes. Tested shapes are square, rectangles, diamonds, triangles, zigzag, jigsaw, circle, and hexagon, from left to right and top to bottom. This shows the effect of cell shapes on printing performance of polymer solutions on plastic substrates. Surface profiles of printed results were measured by using an interferometer.

To test scalability of cell openings, three nominal cell widths were fabricated and tested the same way as previously. Figure 5.7 shows the printed results of square, zigzag, jigsaw, circle and hexagon. As cell width reduces, only square opening shapes can maintain well defined printed features. This indicates that square cells have the best printing performance and scalability. Therefore, only square cells will be used to test the effects of cell profiles (i.e. slopes and depths).

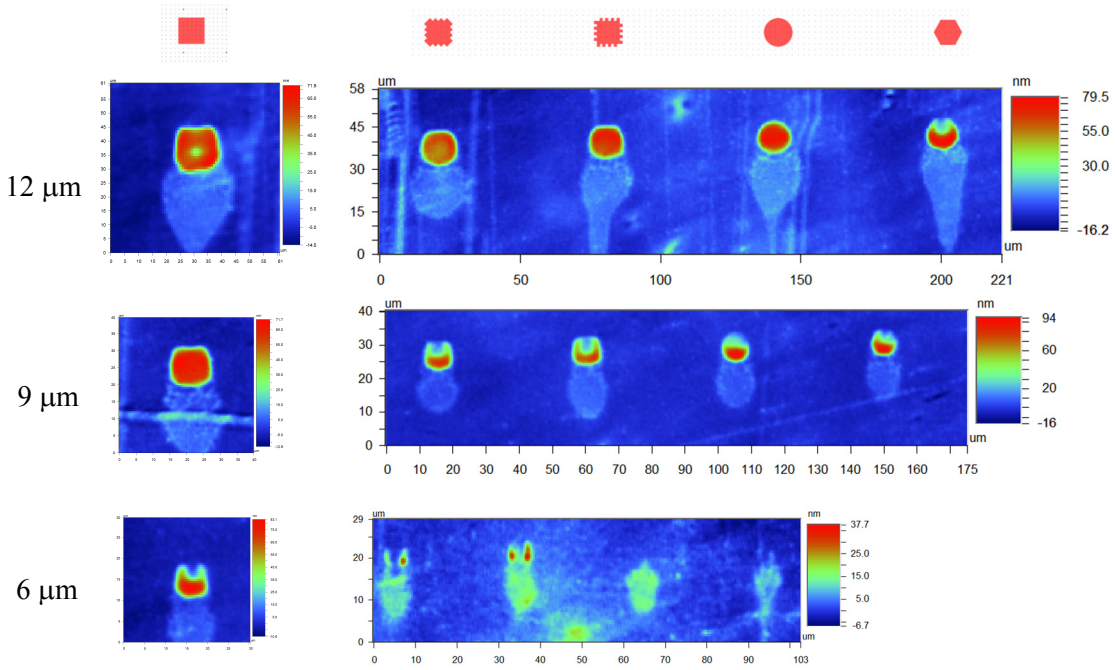

Figure 5.7 The scalability of square, rough square, jigsaw, circle and hexagon. Nominal cell size is scaled to 12, 9 and 6 µm. interestingly, square cells show the best performance.

Furthermore, square cells are suitable as a building block for electronic patterns because of the effectiveness of cell arrangement. Most electronic patterns are rectangles, which can be decomposed into pixels. A pixel is the smallest square unit. Constructing electronic patterns using a square unit results in better edge definitions. For example, consider a line pattern comprised of squares versus circles or hexagons. In high-resolution patterning, a line pattern is a string of the smallest units. While squares result in a straight line edge with periodic small defects due to the cell gap, circles or hexagons cause a wavy line edge due to the curvature of the cell opening shape. These defects are much larger than cell-gap defects in the square case. It requires a great deal of spreading to guarantee that these defects are healed and perfect line edges can be achieved. Zigzag and jigsaw not only suffer from this problem, but they are also difficult to be scaled because their smallest feature is one tenth of the cell width. This requires higher fabrication accuracy.

5.4 Cell profiles

Here the cell profile is defined as a profile of cell slope and cell depth. This profile can affect printing quality through the filling and transfer processes. To get some insight into the effect of cell profiles, three different profiles were fabricated as shown in Figure 5.8a. Only square cell openings were investigated because of their performance and scalability. Three different cell profiles were engraved by two dry etching recipes and one anisotropic (KOH) wet etching. These cell profiles resemble conventional engraving techniques. The first etching process gives rounded wells, which is similar to engraving by indirect laser engraving, i.e. chemical etching. The second etching process gives small trenches at the cell bottom to replicate direct laser

engraving. The third etching process results in an inverse pyramid profile to replicate the electromechnical engraving process. These profiles will be referred to as CM, LS, and EM for indirect laser, direct laser, and electromechanical engraving, respectively.

The printing performance was tested by printing silver nanoparticle ink and measuring sheet resistance. The silver ink used was NPS from Harima. The ink was diluted by AF5 to achieve a viscosity of ~100 mPa·s. After printing, samples were sintered on a vacuum hotplate at 225 °C for 40 min. The printing was performed by using inverse direct gravure at a printing speed of 0.8 m/s. The sheet resistance indicates the thickness of printed lines, assuming that resistivity of sintered printed silver lines is the same for all conditions. The lower the sheet resistance , the thicker the printed line, all else being unchanged. Therefore, a cell profile generally has higher performance if sheet resistance is low. To find printing performance, sheet resistance is normalized by cell volume. This parameter and the aspect ratio of the cell profile indicate the printing performance of cell profiles. Cell aspect ratio is defined as cell depth divided by cell width for CM and LS profiles. For EM profiles, the cell height is calculated by cell volume divided by cell opening. A lower sheet resistance per cell volume and aspect ratio suggests that cells have a higher printed volume fraction. Figure 5.8b shows a diagram of these parameters. Figure 5.8c shows that printed line width is a constant for all cell profiles. Therefore, the sheet resistance indicates film thickness. The sheet resistance per cell volume rapidly reduces as the aspect ratio increases from ~0.2 to ~0.35 and then levels out for larger aspect ratios. This means a higher aspect ratio than ~0.35 does not increase printed volumes. Increasing cell depth further actually reduces printed volume fraction. While CM and LS profiles result in approximately the sample sheet-resistance per cell volume, EM profile can print lower sheet resistance with lower cell aspect ratio. This suggests that EM profiles actually give the highest printed volume faction. Therefore, it is clear that the EM profile is the best cell profile.

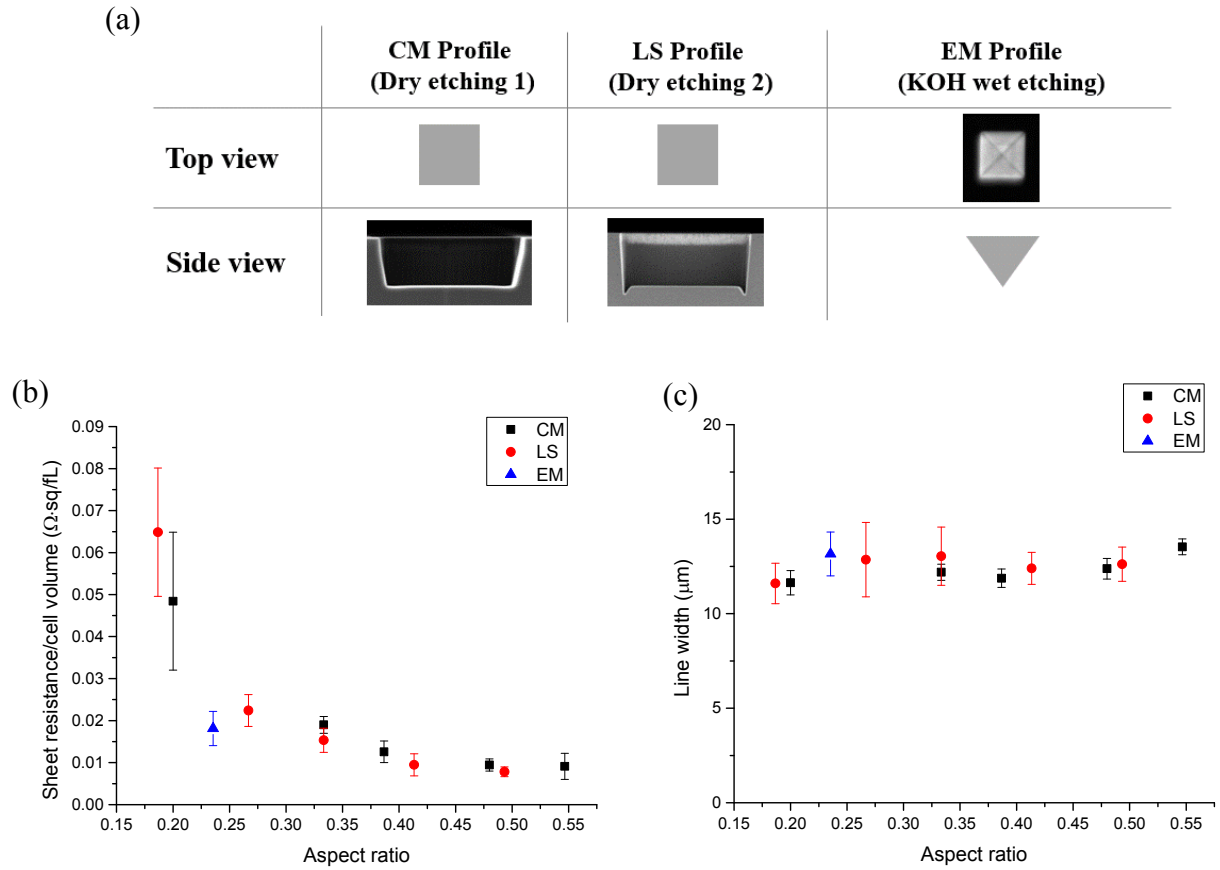

Figure 5.8 (a) three different cell profiles engraved by two dry etching recipes and anisotropic (KOH) wet etching. Top view and side view are given. (b) sheet resistance per cell volume as a function of cell aspect ratio (cell depth to cell width). (c) line width as a function of cell aspect ratio.

It can be understood easily why the EM cell profile is the best. The cell profiles affect mainly the filling and transferring processes, assuming wiping is done by an optimized blade where drag-out is minimized. The EM cell profile provides much better slopes for microscale flows than the steep walls in CM and LW profiles. These inclined walls allow fluids to flow in and out easily and reduce pinning effects on the edges during the filling and transferring processes. Moreover, the EM profiles are fabricated by anisotropic KOH wet etching, which is a self-limiting process. This delivers perfect cell definition with various cell depths. Being able to combine multiple cell depths is critical for complicated pattern optimization. Since liquid patterning needs to balance internal pressures created by Laplace pressures and/or disjointing pressures, multiple cell depths give the freedom of controlling printed volume without depending on cell gaps alone.

5.5 Cell density

Cell density per unit area can affect printed volume due to the drag-out effect. This section demonstrates this by comparing two printed results with different overall cell density. The

experiments were also conducted as a function of printing speed to confirm the effect of drag-out. The cell density was varied by excluding half of the patterns as shown in Figure 5.9 on the left. The first (top row) is the full pattern and the second (bottom row) is the half pattern. The half pattern had much lower overall cell density, but these two patterns contain the same rectangle cells, which are located on the top left of each pattern block. The two printing plates were used to print the same ink, 27wt% PVP solution, at different speeds. The printed results shown on the right of Figure 5.9 reveal that the printed volume is a stronger function of printing speed, if the pattern density is low. This suggests that drag out effect is related to the outlet meniscus. When the pattern density is high, the outlet meniscus is saturated, which effectively reduces dragged-out volume. Therefore, printed volume is a weaker function of printing speed for high cell density. This suggests an important design rule for high-resolution gravure printing. To gain a consistent printed volume, overall cell density must be constant.

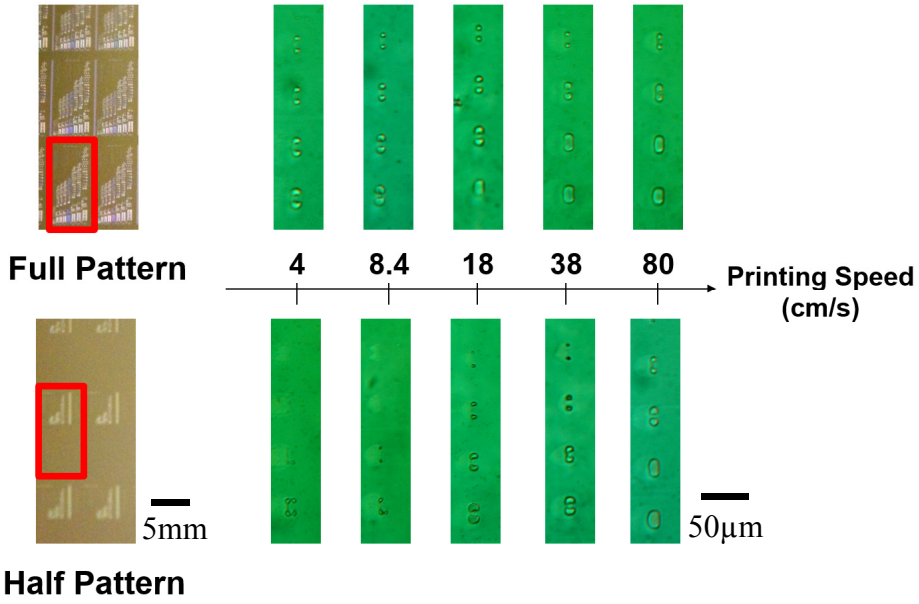

Figure 5.9 the effect of pattern density on printed volume fraction. Top row images show the printed dot patterns as a function of printing speed. Bottom row images show the printed features from the same dot patterns, but nearby patterns are replaced by non-pattern area.

5.6 High-resolution roll fabrication

A high-resolution roll requires smooth finishing of surfaces, small cell size, inverse pyramid cell profile, and arbitrary arrangement of cells. These stringent requirements are not possible with current engraving technologies. In this section, a simple roll fabrication process based on the optimized silicon printing plates and modern microfabrication is demonstrated. First of all, a silicon master is engraved by anisotropic wet etching (KOH solution) to gain the best cell geometry. After that the master is cleaned thoroughly with DI water. The master was then treated with FOTS self-assembly monolayer to reduce its surface energy. This is to facilitate de-moulding process.

Next, a molded replicate is prepared by the following steps. Epoxy was drop cast on the center of a silicon master. Then a glass carrier wafer was slowly pressed onto the uncured epoxy, squeezing epoxy towards the wafer edges. Due to its viscosity and a capillary bridge epoxy stops at the edges. The sample was then thermally cured. However, thermal cross-linking leads to a build-up of undesirable internal stress due to expansion. Therefore UV crosslinking is preferred to thermal cross-linking to avoid internal stress. The molding polymer was changed to Polyurethane acrylate (PUA), because it has high Young's modulus, low surface energy, UV-curing ability, and low viscosity [6]. These properties make PUA an excellent choice for molding nanoscale features. After UV-crosslinking, the mold was easily released by mechanically separation thanks to the low surface energy surfaces of both the master and the PUA replicate. During separation, IPA was added to the gap between the silicon master and the PUA to facilitate the de-molding process for a 6-inch wafer. After that, the PUA replicate on a glass carrier wafer was cleaned by toluene, acetone and DI water.

The next step is to form a metal layer by electroplating. First, a seed layer, Cr/Au, was evaporated onto PUA. PUA was treated by 50W O_2 plasma for 3 min to promote the adhesion of the seed layer. The Cr layer was evaporated just 5 nm thick to promote adhesion between activated PUA and the Au layer. The Au layer was evaporated 60 nm thick. This thickness provides enough conductivity for the electroplating process. Then a thick layer of 80:20 Ni:Fe alloy, also known as Permalloy, was electroplated by using the electroplating solution in [7]. Permalloy provides a strong magnetic holding force due to its high magnetic permeability. The current density was held constant at 27 mA/cm^2. This gave an approximate deposition rate of 28 μm/hr. The plating was processed at 50 °C. After plating for 3-4 hr, where the Ni:Fe alloy was ~100 μm, the sample was pulled out and cleaned with DI water. The top surface (back surface that will be mounted onto roll) looked shiny and showed cell textures. To maximize the magnetic holding force, this top surface was polished by using SiC abrasives until the cell textures disappeared and the surface is mirror-like. Finally, the metal plate (Permalloy layer) was mechanically released from PUA and cut into the roll width. This metal plate is thin enough to be wrapped around a magnetic roll and used as a printing surface of a gravure roll. The edges of the metal plate were held down by Kapton tape. The overall roll fabrication process is displayed in Figure 5.10.

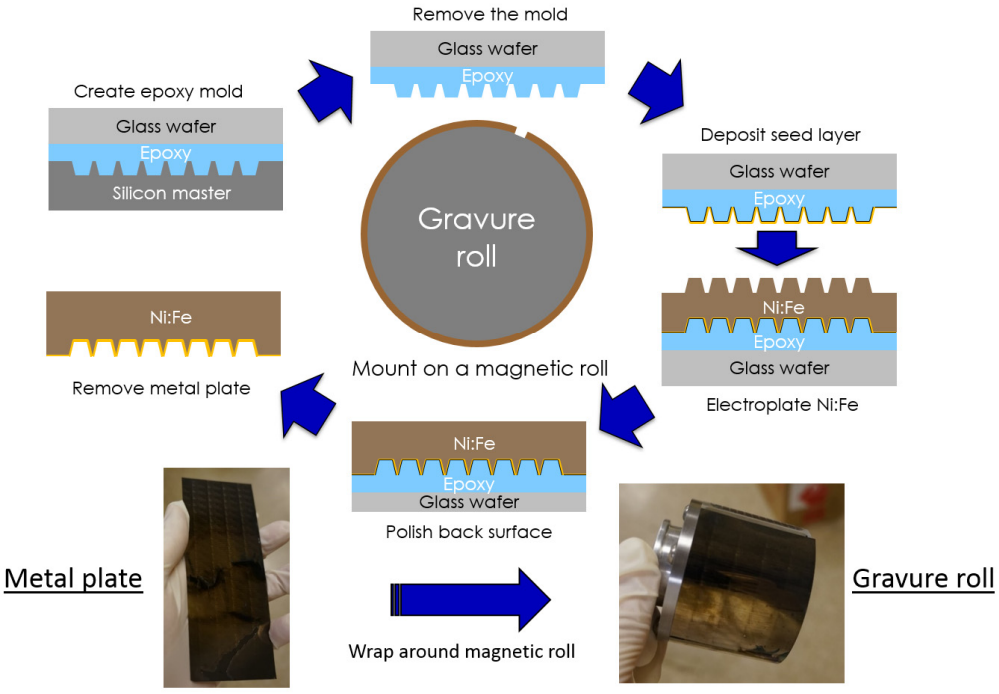

Figure 5.10 High-resolution roll fabrication process. The process flow is as follows: molding an inverse replicate; forming a thin metal plate; releasing and mounting on a magnetic roll.

Figure 5.11 shows optical images of replicated cells. Cell sizes varying from 10 to 1 μm were successfully replicated. Cell gaps as small as 250 nm is also preserved very well. Figure 5.11 (bottom right picture) demonstrates the advantages of this process. Various cell size and depth can be arbitrary arranged in close proximity. This is not possible by conventional engraving technologies as explained earlier. In addition, the surface roughness is extremely low, thanks to the smoothness of the silicon master. Although the surface hardness of Permalloy is lower than a chrome layer, it is robust enough for short printing. The advantage of this process is that gravure patterns can be interchangeable on a fixed roll printer. This facilitates the printing processes, especially in research laboratories.

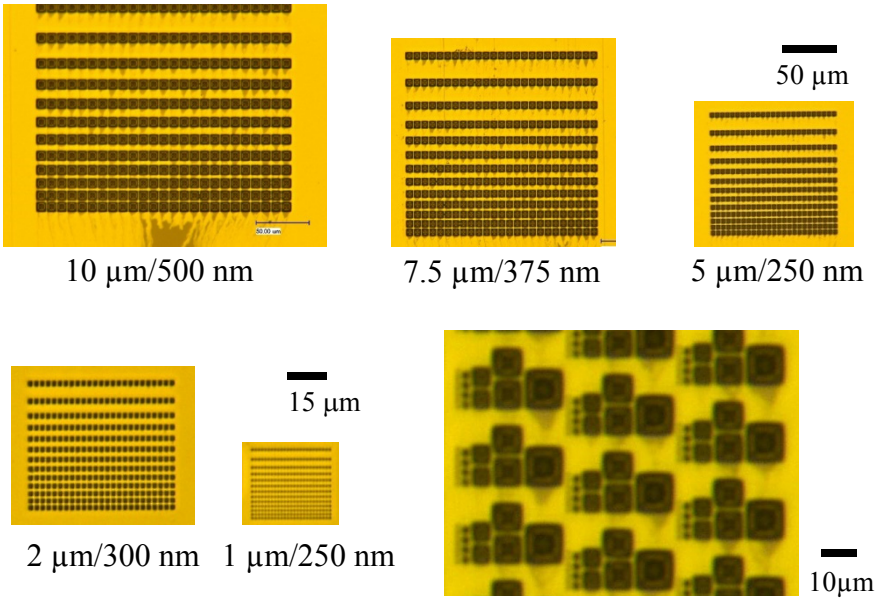

Figure 5.11 Optical images of cell replicates on a metal plate

The printing performance of the high-resolution roll was tested by printing 32.5 wt% PVP in PGMEA on plastic substrate (PQA1) at a speed of 0.5 m/s. The substrate was treated by UVO for 10 min before printing. Figure 5.12 shows printed results from 10, 7.5 and 5-µm cells. The printed patterns preserved the design pattern. 2 and 1-µm cells were printed, but residues overwhelmed the desired features, due to imperfections in the metal plate mounting. These printed results confirmed that the proposed roll fabrication process successfully produces high-resolution rolls with cell sizes as small as 5 µm. The surface finishing was supreme compared with conventional chrome finishing.

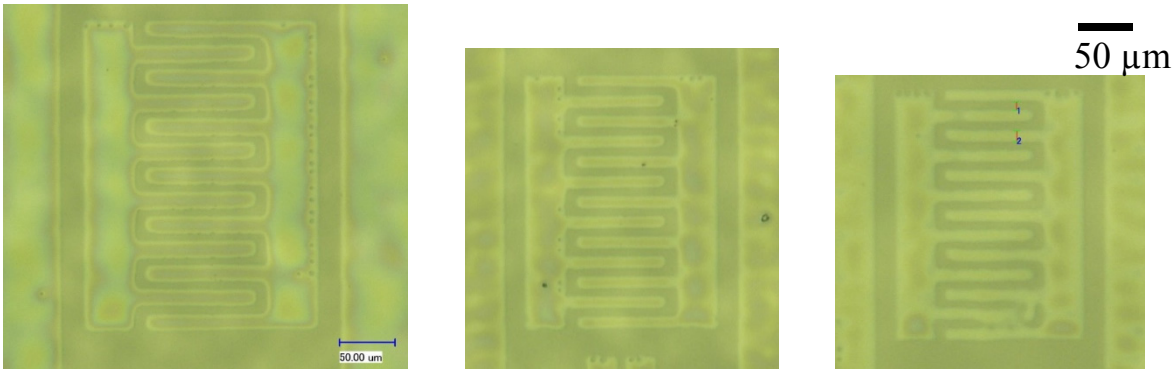

Figure 5.12 Optical images of printed features by using a high-resolution roll.

5.7 Conclusions

In this chapter, current engraving technologies are reviewed. Upon the review, it reveals that the shortcomings of the current technologies are a hindrance for high-resolution gravure printing. To overcome this, the effects of cell geometry is investigated, leading to a simple high-resolution roll fabrication. This process is rooted on modern microfabrication, which has several advantages for fabricating sub-micro features. Both anisotropic dry and wet etching were investigated as alternatives to the conventional engraving techniques, such as mechanical cutting, laser ablation and isotropic chemical etching. Various cell opening shapes were investigated to find a suitable cell opening for highly-scaled gravure printing. The results suggest that square is the best of all tested opening shapes, because it has a symmetric shape, maintains printing performance as cell size is scaled down and is suitable for composing electronic patterns. Different cell profiles affecting the filling and transferring processes were also examined by using different etching processes. The results confirmed physical understanding built from earlier chapters; that is the inverse-pyramid cell profile performs better than other profiles. This best cell geometry, square opening and inverse-pyramid cell profile, can be fabricated by simple lithography and anisotropic wet etching, which give a further advantage of this fabrication process. In addition to studying individual cells, the effect of cell density is also examined and explained. The drag-out effect causes the printed volume to depend on cell density. A higher density is required to print small cell volume, since it can reduce the drag-out effect. Finally, a high-resolution roll is fabricated. The process is simple and satisfies stringent requirements in terms of the smallest features, surface finishing, and cell arrangements. The high-resolution roll is a magnetic roll with a thin metal sheet carrying the patterns. The metal sheet is a replicate of optimized silicon printing plates by polymer molding and electroplating processes. By using this roll, features below 10 μm can be printed. The features are worse compared to printed results from silicon printing plates, but better than conventional engraved rolls. However, this fabrication demonstrates a feasible pathway for realizing high-resolution gravure printing.

5.8 References

[1] K. Gillett, “Gravure—Process and Technology,” *GAA GEF, Rochester, 2nd Ed. New York*, 2003.

[2] G. Henning, K.-H. H. Selbmann, S. Mattheus, R. Kecke, Stephen Bruning, G. Hennig, and S. Brüning, “Laser Precision Micro Fabrication in the Printing Industry,” *J. Laser Micro/Nanoengineering*, vol. 1, no. 2, pp. 89–98, Jul. 2006.

[3] G. Hennig, K.-H. Selbmann, and A. Brockelt, “Laser engraving in gravure industry,” *Proc. SPIE*, vol. 6157, p. 61570C–61570C–14, 2005.

[4] O. G. Technologies, M. Microengraving, and C. Micro, “Gravure.”

[5] M. a. Vyvoda, M. Li, D. B. Graves, H. Lee, M. V. Malyshev, F. P. Klemens, J. T. C. Lee, and V. M. Donnelly, “Role of sidewall scattering in feature profile evolution during Cl[sub 2] and HBr plasma etching of silicon,” *J. Vac. Sci. Technol. B Microelectron. Nanom. Struct.*, vol. 18, no. 2, p. 820, 2000.

[6] S.-J. Choi, P. J. Yoo, S. J. Baek, T. W. Kim, and H. H. Lee, “An ultraviolet-curable mold for sub-100-nm lithography.,” *J. Am. Chem. Soc.*, vol. 126, no. 25, pp. 7744–5, Jun. 2004.

[7] T. E. Buchheit, S. H. Goods, P. G. Kotula, and P. F. Hlava, “Electrodeposited 80Ni–20Fe (Permalloy) as a structural material for high aspect ratio microfabrication,” *Mater. Sci. Eng. A*, vol. 432, no. 1–2, pp. 149–157, Sep. 2006.

Chapter 6 Fully-Printed Top-Gate Organic Thin Film Transistors

6.1 Introduction

Thin-film transistors (TFTs) are the building block of electronic systems and it is critical to develop a fabrication process for high performance TFTs that is roll-to-roll (R2R) compatible to enable truly low-cost mass production techniques. Numerous researchers have reported printed TFTs fabricated using various printing techniques, including inkjet, step-and-flash imprint lithography, screen, flexography, offset, bar coating and gravure printing [1]–[8]. While progress has been substantial, performance still largely falls below that required for the modern electronic applications. This performance gap can be addressed by improving printing resolution to realize devices with smaller channel lengths and by using higher performance materials. Several pattern printing techniques have been proposed to produce such high-resolution (sub-5 μm) printed features such as electrohydrodynamic (EHD) printing [9], capillary printing [10], hybrid printing (print-and-drag) [11], soft lithography [12], and micro-imprint lithography [13]. However, these printing techniques are generally not suitable for mass production, since they requires multiple process steps, complicated tooling, and slow printing speeds. Our previous chapters showed that direct gravure printing does offer scalability to the 5 μm range and thus is attractive for fabrication of MHz-class TFTs [14].

While high-resolution, high-speed printing in the sub-5μm is now technologically within reach, this does not completely address the issues associated with realization of high-performance TFTs. In particular, while patterning resolution has scaled, layer-to-layer alignment has not scaled in a commensurate manner. Given the large distortion common in typical flexible plastic substrates, coupled with the high printing speeds used therein, it is necessary to couple improvements in printing resolution with device structures that are tolerant to misalignment. Indeed, given the aggressive resolution scaling we are able to achieve, the limiting factor on device geometry is alignment, rather than resolution; while very fine features can be printed, aligning to them using plastic substrates moving at high speeds is virtually impossible. Therefore, in this chapter, we report on a comprehensive approach to realizing high-performance printed OTFTs that addresses all of these issues. Specifically, we report a large-area, high-speed, high resolution printing technique for forming fully printed high performance TFTs using advanced nanomaterial and organic materials, coupled with a misalignment-tolerant device stucture that allows us to aggressively scale device geometry without being impacted by poor alignment. This in turn allows us to realize fully printed transistors on plastic with transition frequencies >1 MHz. Given that layer-to-layer alignment during high-speed printing on flexible substrates remains challenging, this then delivers a promising pathway for realizing high-performance printed electronics.

6.2 Experimental section

To precisely fabricate gravure cells with atomically smooth surfaces, we used silicon substrates as the “engraved” surfaces and standard microfabrication techniques to create the “engravings”. The fabrication process started by using optical lithography and reactive ion etching process to

define a cell opening in an oxide masking layer on a (100) silicon wafer. The wafer was then dipped into a potassium hydroxide (KOH) solution to perform anisotropic wet etching of the silicon, forming ideal inverted pyramid cells. After that, the oxide layer was removed by wet etching using hydrofluoric acid. As a result of this microfabrication process, a prefect inclination angle of 54.74° with smooth surfaces and sharp edges can be obtained. Cell widths (CW), defined as the opening width of inverted pyramid cells used in this study, were 2, 3, 4, 5 and 6 μm. The cell gaps (CG) of lines and contacts were kept constant at 0.1 and 0.2 times the cell width, respectively. For uniform film coating, a commercial gravure roll from IGT testing systems was used. A gravure roll from IGT 402.101 consists of 4 engravings patterns and is engraved by electromechanical engraving. Printing plates and rolls were cleaned by effective solvents for each ink and dried by a nitrogen gun. In order to deliver the ultimate printing quality, we used polished blades as demonstrated in [15]. The doctor blades used are lamella blades, also known as standard blades, supplied by Max Daetwyler Corp. The doctor blades have a tip diameter of 75 μm and a body thickness of 200 μm. The blade was polished using diamond lapping films. The final polishing was performed on 1-μm diamond lapping film.

This study focuses on the process integration of advanced materials for organic thin transistors. The S1200 top gate package (B.36303) was supplied by EMD Chemicals. The material package consists of semiconductor (lisicon® S1200-1572), contact surface treatment (lisicon® M001), two gate dielectrics (lisicon® D139 and lisicon® AP043X-MAK). D139 is a gate dielectric forming on top of semiconductor layer and AP043X-MAK is a surface treatment solution, which allows direct printing on a low surface energy surface of D139. D139 was modified by Fluorinert® solvents (FC-70 and FC-770) purchased from Sigma Aldrich to obtain a very uniform film. AP043X-MAK was diluted by Ethyl 3-ethoxypropionate (EEP) purchased from the same company. A silver nanoparticle ink (NPS) from Harima chemicals Group was used for source/drain electrodes. To obtain the correct viscosity, NPS was diluted by its solvent AF5 so that its viscosity was ~100mPa·s. Silver nanoparticle ink (DGP 40LT-15C) was used for the inkjetted gate electrodes. All substrates used were plastic substrates (PQA1 from Dupont Teijin Films).

The fabrication process started with cleaning substrates in an ultrasonic bath with isopropanol and acetone for 10 min each, following with oxygen plasma treatment for 30 s. Then, source and drain electrodes were printed using an inverse direct gravure at speed of 0.6 m/s. The nanoparticle ink was filtered before printing. After printing, the substrates were heated on a hotplate with a ramp rate of 3 °C/min until the surface temperature reached 220 °C and then held for 1 hr. To increase the work function of the electrodes, samples were treated using an H_2/N_2 (5/100 sccm) plasma at 40 W for 30 s. The semiconductor was printed using a sheet-fed direct gravure printer at a speed of 0.5 m/s. Immediately after printing, the semiconductor was dried on the substrate carrier using a hot air gun. The drying temperature is ramped from room temperature to 80 °C with a ramping rate of 4 °C/s. After that, samples were air cool to room temperature. Dielectric layers were also printed by direct gravure at a speed of 0.5 m/s. Film thickness was controlled by cell depth and ink concentration. Total gate dielectric thickness was ~200 nm. The unifromity was promoted by using a mixture of three solvents, as discussed above.

After printing dielectric layers, the samples were dried in an oven at 75 °C for 5 min. Finally gate electrodes were printed using a Dimatix inkjet printer. The sample was sintered at 100 °C surface temperature for 30 min with a ramp rate of 5 °C/min. For spin-coated test devices, the semiconductor and dielelctric layers were deposited by spin coating instead of gravure printing. The semiconductor layer was spun at 8500 rpm at dried in oven at 75 °C for 1 min. The first and second dielectric layers were spun at 3000 rpm and 6000 rpm, respectively. D139 and AP043x inks were diluted by FC-70 and EEP with 1:1 and 1:2 by volume to produce total gate dielctric of ~200 nm. A detailed process flow of fully printed TFTs is shown in Figure 6.1. Devices were fabricated on plastic substrates over an area of 50×50 mm^2.

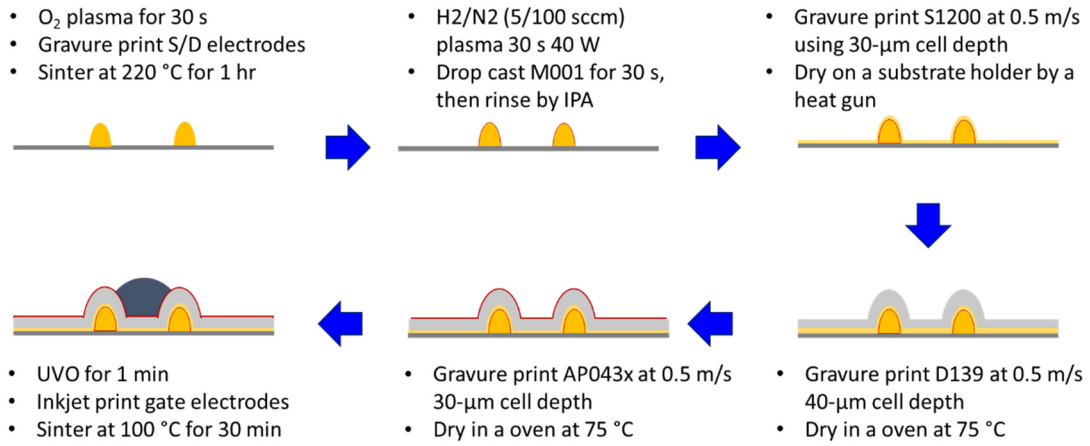

Figure 6.1 Process flow used to fabricate fully printed high performance thin film transistors

Line metrology including critical dimension, line width roughness and line edge roughness were analyzed using SuMMIT software. Sheet resistances were measured by using four point probe structures and an Agilent 4156C semiconductor parameter analyzer. DC characteristics of the TFTs were measured by using an Agilent 4156C semiconductor parameter analyzer under nitrogen environment. AC performance was tested by constructing common source amplifiers using external resistors. The input signal was applied directly to the gate electrodes by a HP 33120A function generator and the output signal was measured on the drain electrodes by using a Tektronix DPO2024B mixed signal oscilloscope. The source electrode was supplied by a DC power supply at 15V. The AC characterization was performed under ambient air.

6.3 Printing high-resolution source/drain electrodes

Printing nanoparticle inks for sub-5µm features requires a deep physical understanding of grauvre printing as discussed in [15]. High-resolution, high-speed printing of fine features is possible by supressing lubrication-related residues. Harima silver nanopaticle ink is selected, because of small paritcle size, high mass loading, and low evaportion rate, which are necessary for high-resolution, high-speed gravure printing. The small size nanoparticle and encapsulating ligands also minimize any possible shear thickening caused by high shear rates during wipping as discussed by Wagner and Brady [16]. A mass loading of ~75wt%, which is much higher than

typical inkjet printing inks, is essential to achieve high resolution conductive lines, since printed volume is scaled aggressively [14], [15]. However, an increased sintering temperature was needed for this ink to deliver good adhesion the of silver electrodes on plastic substrates. Sintering at temperatures as low as 140 °C is possible to achieve conductive lines, but during subsequent processes, the silver electrodes were found to delaminate from the substrates. To improve the mechanical stability of the source/drain electrodes, sintering above the glass transistion temperature of a plastic substrate was found to be required [17]. After sintering, the sheet resistance of the resulting high resolution lines was tested using four point probe structures as shown in Figure 6.2. The sheet resistance was below 3.35 Ω/□, which is very suitable for high performance printed electronics applications.

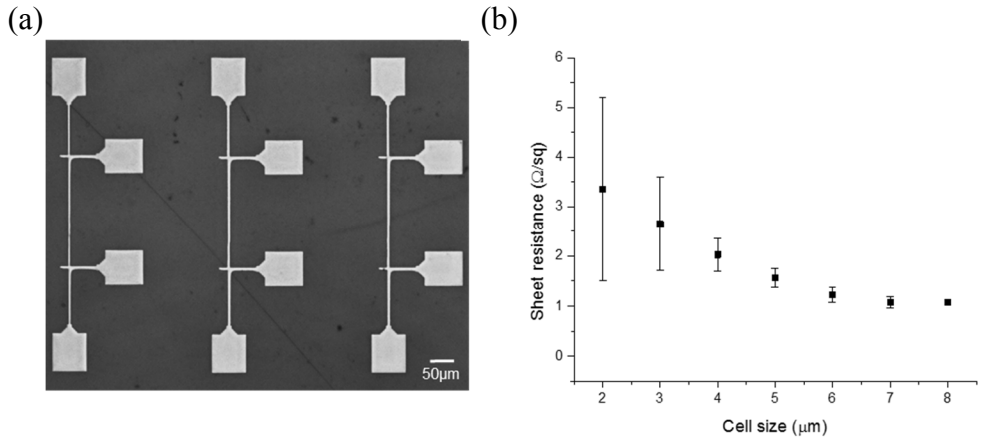

Figure 6.2 (a) Printed four point structures for measuring sheet resistance. After printing, samples were sintered at 220 °C for 1 hr with ramp rate of 3 °C/min. (b) extracted sheet resistance as function of cell size from 8 to 2 μm. The median of sheet resistance of the smallest lines is below 3.5 Ω/□.

In addition to reducing lubrication-related residues, designing a master pattern is a key to achieving high resolution patterning in gravure printing. There are two types of gravure patterns, groove-based and cell-based. Groove-based patterns are normally referred as Intaglio; these are typically not preferred in complex patterns, since the print quality typically shows a strong orientation dependence. In cell-based patterns, the features are constructed by using an array or string of individual cells with designed cell gaps. Figure 1a shows definitions for a cell-based gravure master pattern. The cell width, CW, is defined as an opening of a square cell and the cell gap, CG, is a gap between nearest cell edges. The CG acts as a barrier prohibiting drag-out effects, but create unprinted areas within desired patterns [14]. After printing, some spreading of the ink as shown in Figure 6.3a is essential to successfully form continuous features. The effects of the ratio of CG to CW were investigated from 0.05 to 0.35 as shown in Figure 6.3b. A ratio of 0.5 causes bulging similar to that reported previously for inkjet printed lines, indicating too much ink volume per unit area [18]. At the other extreme, ratios larger than 0.15 result in increased line edge roughness due to insufficient spreading. Therefore, a ratio of 0.1 was used in this work to

achieve the best line pattern fidelity. To define short channel lengths, we varied the ratio, α , of channel length, L, to CW as shown in Figure 6.3a.

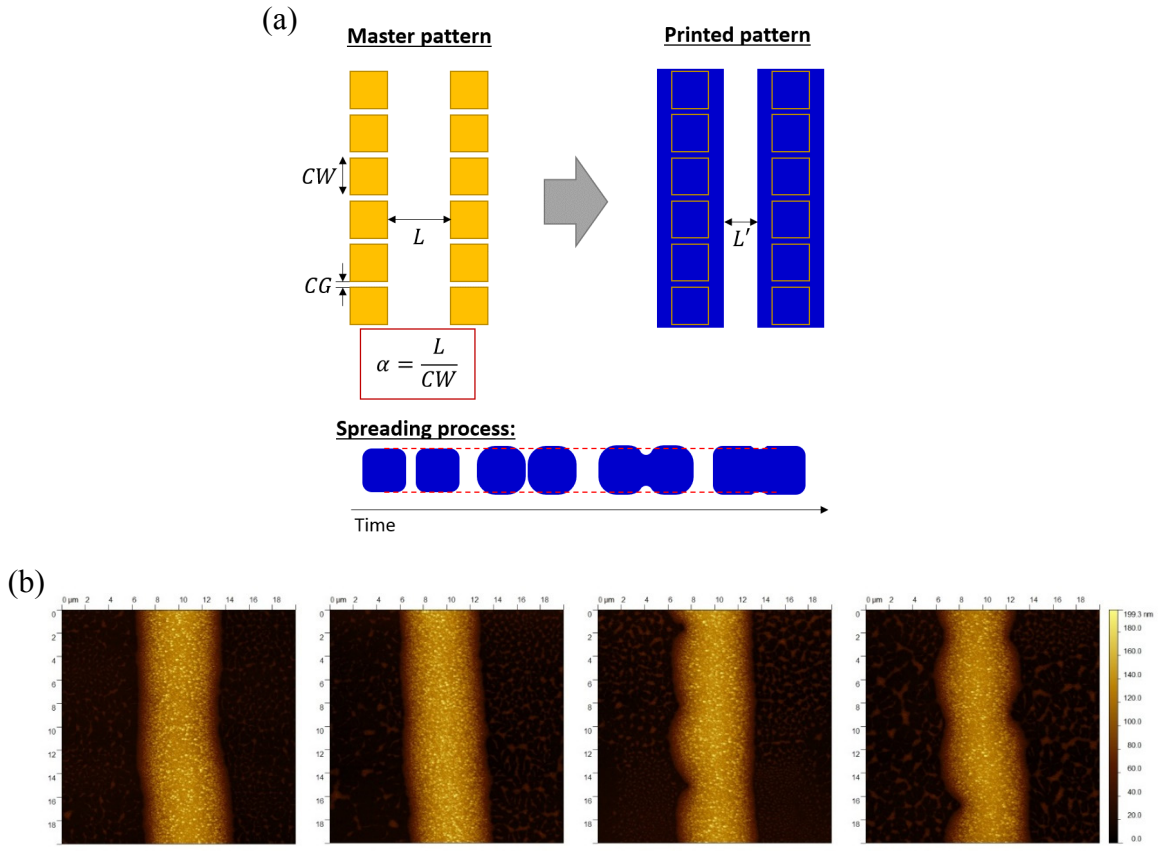

Figure 6.3 (a) Definitions of highly-scaled gravure patterns. Cell width and channel length are defined as width of square cells and spacing between cell edges, respectively. Printed channel length, L′, is smaller than defined channel length, L, due to the spreading process. (b) Effects of cell gap on line width roughness. Cell width was 5 μm and cell gaps were 0.25, 0.75, 1.25, 1.75 μm from the left to right.

Figure 6.4a shows gravure patterns of S/D lines and contacts on a printing plate with cell width of 2 to 6 μm. Figure 6.4b shows a close-up image of contacts, S/D lines and taper joints. The ratio of CG to CW on contacts array is 0.2, to achieve optimized volume and aviod any bulging on the contacts. A taper joint between electrodes and contacts is used to minimize fluid pressure differences due to Laplace pressure that can cause discontinutity between lines and contacts [19]. As a result of these optimization strategies, the ultimately achieved high resolution S/D electrodes is demonstrated in Figure 6.4c. The inset shows details of the electrodes. The line width is ~2.38 μm and channel length is ~1.7 μm; this is a dramatic improvement over the state of the art in printed electronics patterning technology.

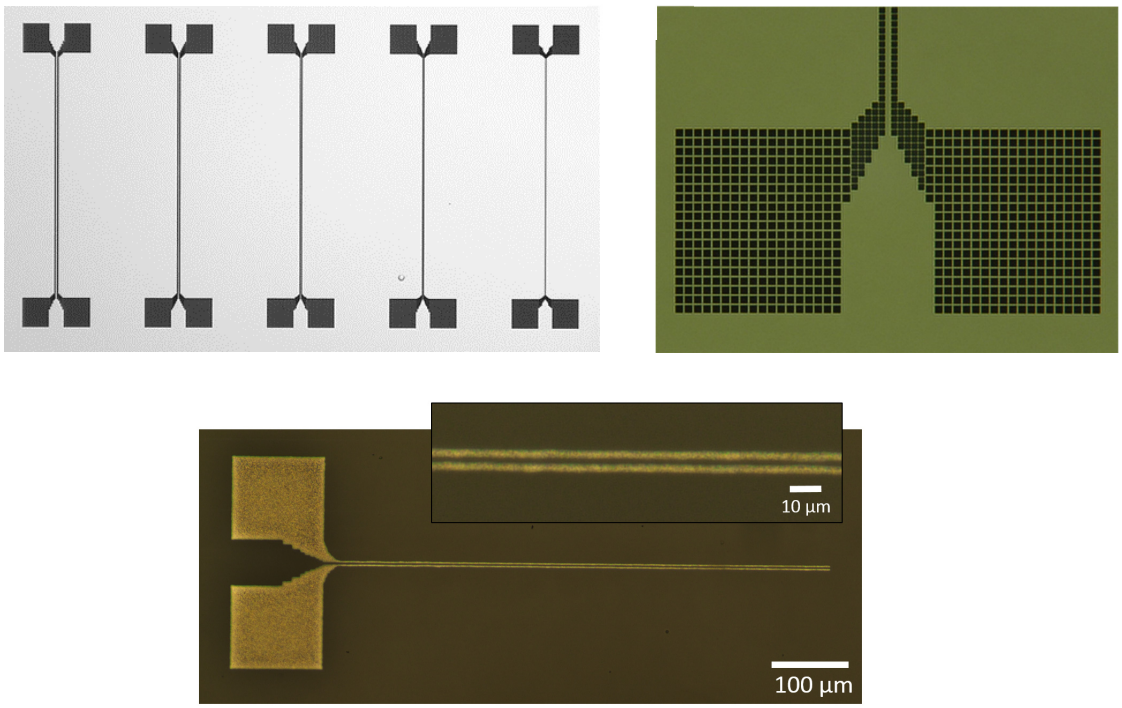

Figure 6.4 (a) S/D patterns on a printing plate. Cell widths in lines are 6 to 2 µm from the left to right. (b) a close-up image highlighting cell arrangement of lines, contacts and taper joints. Cell widths in lines and contacts are 5 and 4 µm, respectively. (c) A representative S/D electrode pair after sintering of the smallest line width (2.38 µm) and channel length (1.7 µm).

Line metrology including critical dimension, line width roughness and line edge roughness are important parameters for characterization of electronic patterns. The critical dimension is defined by the smallest feature that can be patterned. The line width roughness is a measurement of line width variation from the average, which is the critical dimension here. And the line edge roughness indicates a variation of a line edge from an ideal line edge. The smaller line width and edge roughnesses are, the better a pattern technique is. Figure 6.5a shows that the LWR is slightly larger than 1.4 times LER, which indicates that the roughness of edges is mostly uncorrelated to cell gaps [20]. This confirmed that the selected cell gap is optimized. Figure 6.5b displays the channel length. The channel length is scaled proportionally to the designed length for large α. However, when α is smaller than 1.5 the two electrodes merge. Figure 6.5c shows that LWR is scaled with cell size. Therefore, smaller cells are perferred for defining short channel lengths.

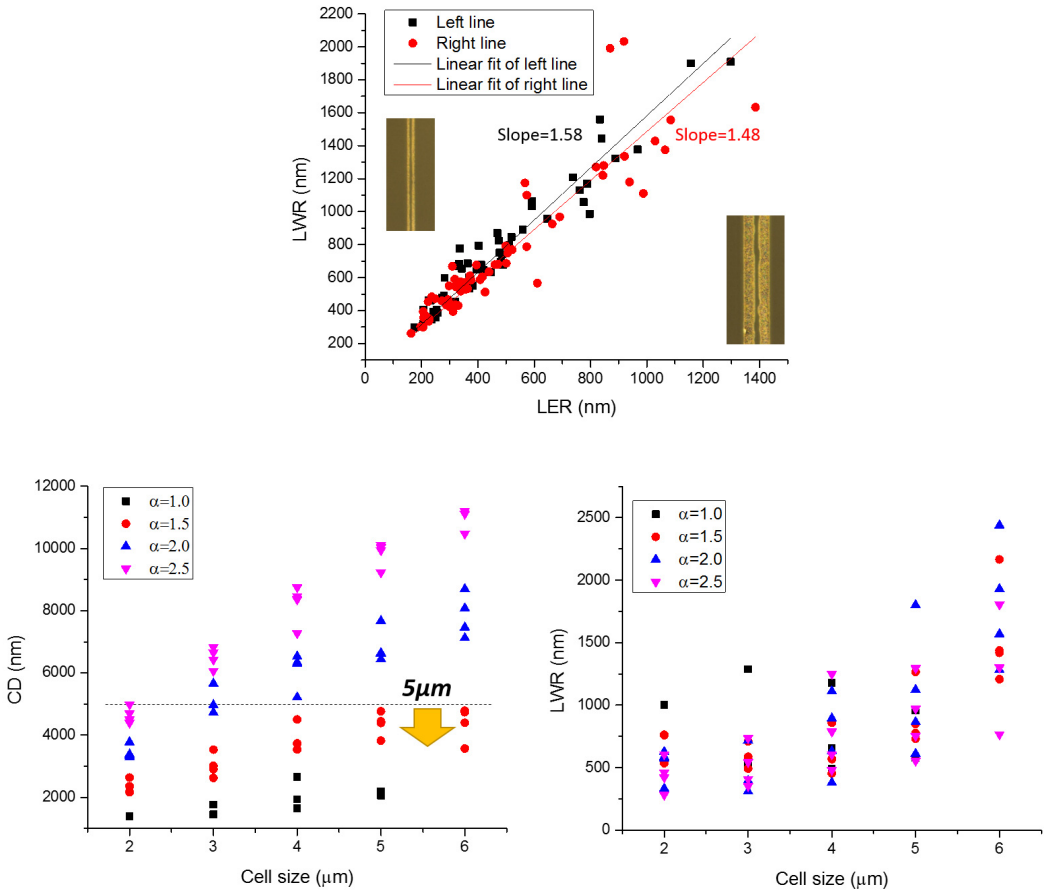

Figure 6.5 (a) Correlation of LER and LWR. (b) and (c) Channel length and LWR as a function of cell size, respectively.

6.4 Process integration

First of all, we integrated the high resolution S/D electrodes printed by gravure into a p-type top-gate/bottom-contact TFT structure. We used a fully overlapped structure in order to relax alignment requirements, as discussed above. Since high resolution gravure printing can delivery both small line widths and gaps, we can simultaneously minimize overlap capacitance and channel length using this approach. This thus provides a manufacturable path for low-cost high performance TFTs. The S/D electrodes were first treated with a forming gas plasma and contact treatment solution to form good contacts with the semiconductor. A dual dielectric layer was used to ensure good printability and good device preformance. The first layer is a fluoropolymer that form a good interface with the semiconductor. However, it is difficult to directly printed on this fluoropolymer due to its lower surface energy. The second dielectric solution is engineered to be able to uniformly wet on the fluoropolymer, simplifing the fabrication. To maximize total gate capacitance and breakdown field, we tested dielectric performance using gravure and inkjet-printed electrodes and spin-coated dielectric layers as shown in Figure 6.6. The results in Figure 6.6b and c show that the first layer provides high breakdown field and the second layer has slightly higher dielectric constant.

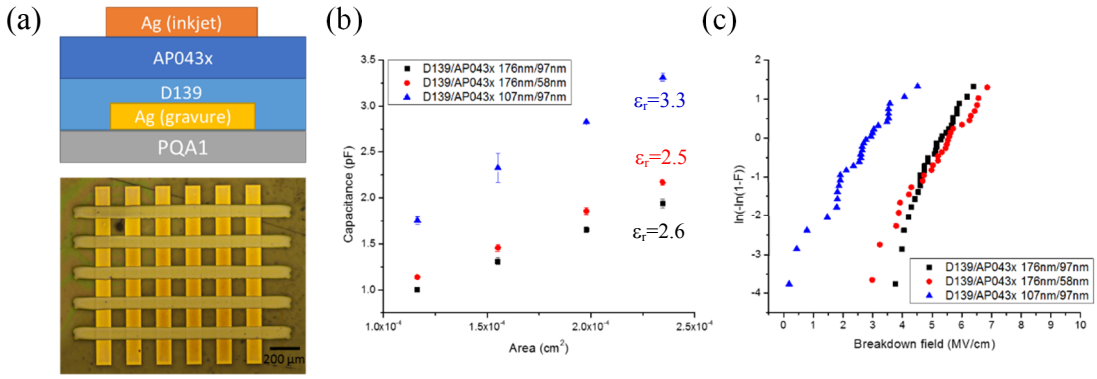

Figure 6.6 (a) A cross section of a test structure of dual dielectric layers (top) and top view optical image of fabricated capacitors (bottom). Bottom and top electrodes were printed by gravure and inkjet printer. (b) Capacitance as a function of capacitance area and corresponding extracted dielectric constants of dual dielectric layers. Dielectric constant decreases as a fraction of AP043x layer is smaller. (c) Weibull plots of dual dielectric layers. The D139 layer provides higher electrical breakdown field.

Next, a silver nanoparticle ink was printed as the gate electrode. The detailed fabrication process is provided in the experimental section. The device characteristics are shown in Figure 6.7. The saturation and linear mobilities were 0.46 and 0.27 $cm^2/V \cdot s$ and the ratio of Imax/Imin was 10^3. The mobilities are lower that previous work using the same semiconductor, as reported by Fujisaki [21]. This could be explained by the use of nanoparticle-based printed S/D electrodes instead of evaporated Au electrodes, which may impact apparent extracted mobility using a square-law formalism due to degraded carrier injection. We also used these devices to optimize the thickness of the semiconductor and dielectric layers. The semiconductor optimized thickness was found to about ~27 nm and thinest dual dielectric thickness with acceptable leakage and breakdown characteristics was ~200 nm.

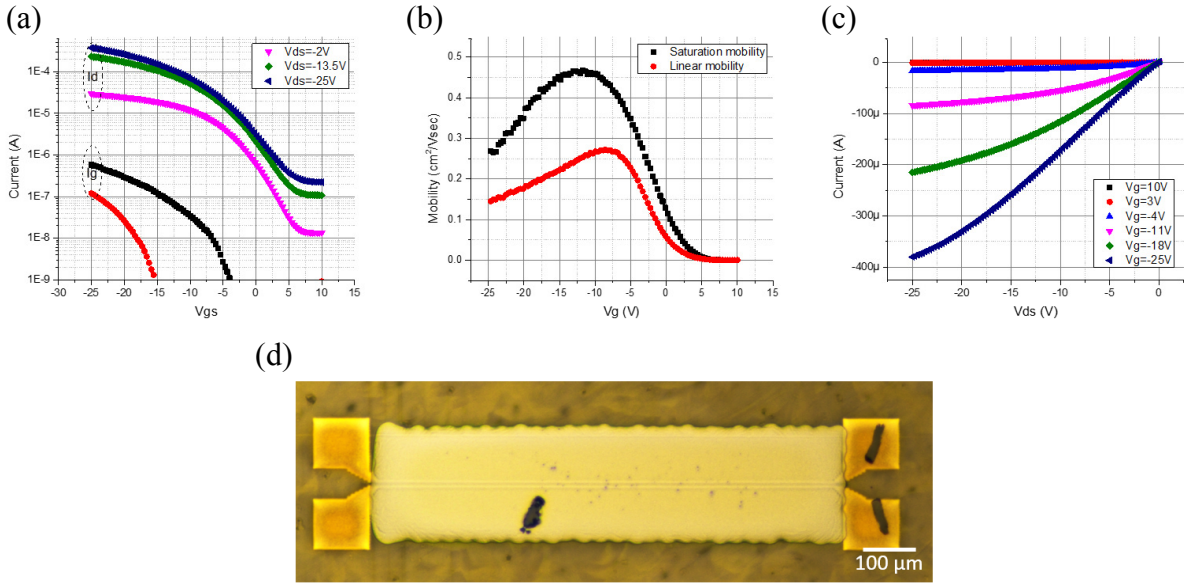

Figure 6.7 DC characteristics of a spin-coated TFT using high resolution gravure printed S/D electrodes and inkjet printed gate electrodes (a) transfer characteristic, and (b) associated mobilities, and (c) output characteristic curves. (d) optical image of the fabricated device. L=3.6 μm, W=963 μm, μ_{sat}=0.46 $cm^2/V \cdot s$ and μ_{lin}= 0.27 $cm^2/V \cdot s$, Vt=0.61 V, swing=5.15 V/dec and Imax/Imin=10^3.

Finally, to fabricate fully printed devices the semiconductor and dielectric layers were printed by gravure printing, instead of spin coating, using conventional mechanically engraved gravure patterns shown in Figure 6.8. The line density and screen angle of the patterns are 70 line/cm and 53°. These parameters specify the position of the center of each engraved cell. To control printed volume per unit area, the engraved cell depth is varied as shown in Figure 6.8 from left to right where the cell depths are 40, 35 and 30 μm. As the cell depth is made shallower, the cell gap increases. After printing, the individual dots on the substrate spread to develop a uniform film. This is normally called "leveling" in the coating industrial. This process involves flows induced by evaporation, gravity, surface tension, and surface gradient [22]. In thin film coating, the effect of the surface tension gradient is more important than other effects.

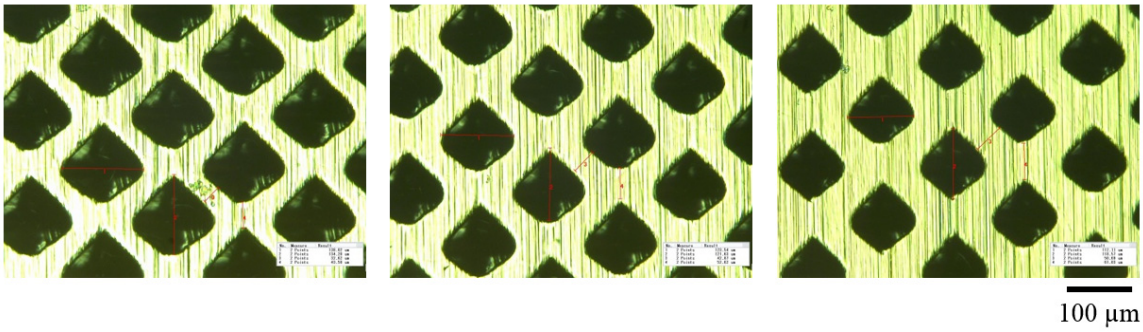

Figure 6.8 Optical images for conventional gravure patterns engraved by electromechanical engraving with cell depths of 40, 35 and 30 μm from the left to right.

In a top-gate device, the printing of the semiconductor is a critical process. Since the dielectric is printed over the semiconductor, too rough a semiconductor layer can result in pinholes in the dielectric, leading to gate-to-S/D shorts. Therefore, we studied the impact of the semiconductor printing and drying conditions. The semiconductor ink spreads during printing, thanks to use of appropriate co-solvents to promote spreading. A thick semiconductor film printed from cells with a 45-μm cell depth as shown in Figure 6.9a results in rough films and short circuit between the S/D and gate electrodes. The films printed using cells with 30-μm cell depth give smooth films, suitable for device integration. The effects of drying rate is shown in Figure 6.9b. Slow drying rate causes the semiconductor film to de-wet from the substrate and high drying rate results in small grains. Therefore, the semiconductor layers was printed using a 30-μm cell depth and dried using ramp rate of 4 °C/s.

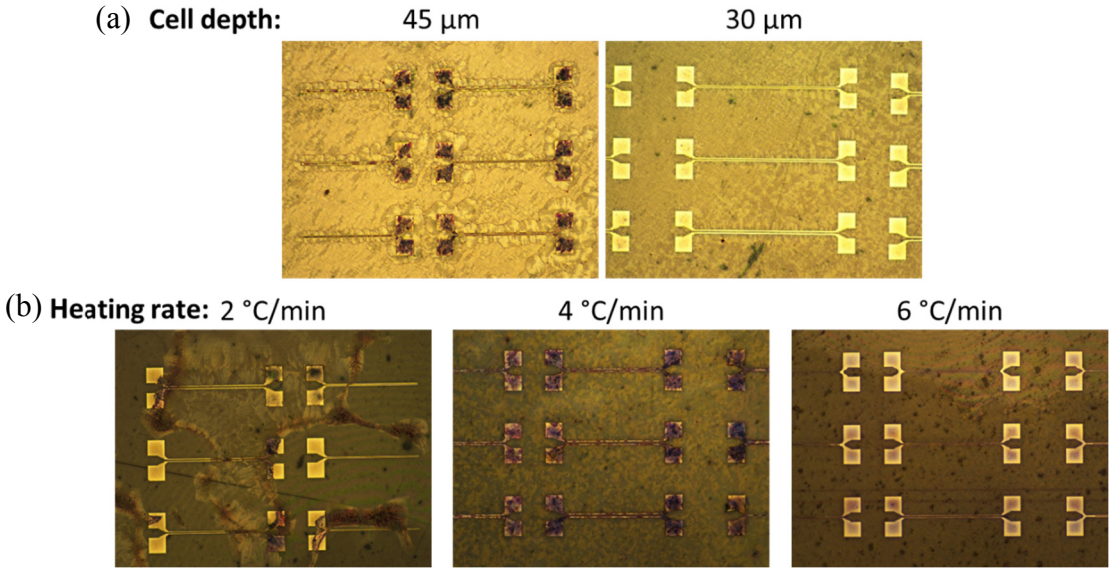

Figure 6.9 (a) The effects of film thickness as printed by a conventional gravure pattern with 45- and 30-µm cell depths. The 45-µm cell depth results in film thickness of 60-70 nm and roughn semiconductor surface morphology, causing a short circuit between gate and S/D electrodes. The 30-µm cell depth gives thinner and smooth films with film thickness of 20-30 nm. Samples were heated at 4 °C/s. (b) the effects of drying rate on semiconductor films printed by 30-µm cell depth. The heating rates were 2, 4, and 6 °C/s and the peak temperature was held at 80 °C for 30 s. Slow drying rate causes semiconductor films to dewet from samples and high heating rate reduces semiconductor grain size.

Scaling of the dielectric layer is necessary along with channel length scaling to ensure good electrostatic integrity of the device. To this end, dilution of the as-supplied D139 dielectric was necessary, since the as-supplied D139 is too viscous and offers insufficient spreading to print thin uniform dielectric films. The physical properties of the as-received D139 ink and selected solvents are available in Table 6.1. Table 6.2 shows ink compositions and their viscosity used in this work. The results of dilution studies are shown in Figure 6.10. Adding only FC-770 leads to pinholes because of limited spreading due to its high evaporation rate. Adding only FC-70 causes wavy films, because of its high viscosity and small surface-tension gradient, leading to small leveling forces. When FC-770 and FC-70 were used simultaneously, the best uniformity was obtained, as shown in Figure 6.10a center. This is because of suitable evaporation, viscosity and surface-tension gradient. The effect of cell depth are shown in Figure 6.10b. The cell depth changes both cell volumes and cell gaps as explained earlier. In the case of 30-µm cell depth, a continuous film is never formed even using the best ink composition due to the small cell volume and large cell gap. For 40 and 35-µm cell depths, continuous films form, but the 40-µm cell depth results in a more uniform film. This signifies the important of altering ink compositions. With the right composition smooth films with surface roughness as small as 2 nm can be printed at high speed on large area plastic substrates by gravure printing. It is worth noticing that the regions of highest thickness in the 40 and 35-µm cell films are the area of cell gap. This is due to

an effect similar to the coffee ring effect commonly seen in inkjet printing, caused here by the strong spreading of the optimized ink and the resulting formation of crests at the edges of the cells. Figure 6.10d shows the film roughness as a function of ink composition and cell depth. Once the ink composition is optimized, the film thickness can be easily controlled by cell depth to achieve a dielectric film thickness of 200 nm for fully printed TFTs as shown in Figure 6.10d. Next, a thin AP043x layer was printed by using an ink composition of AP043x:EEP 1:2 by volume. AP043x was printed directly on D139 (fluoropolymer layer) without any treatment.

Table 6.1 Physical properties of solvents for optimizing D139 film uniformity

	D139	**FC-770**	**FC-43**	**FC-70**
MW		399	670	820
Boiling point (°C)		95	174	215
Vapor Pressure (Pascal)		6570	192	15
Viscosity (mPa·s)	337	1.4	4.7	24.0
Surface tension (mN/m)		15	16	18
Density (g/cm^3)	2.03	1.80	1.86	1.94

Table 6.2 Ink compositions for optimizing film uniformity of gate dielectric and ink viscosities

Ink	**D139 (ml)**	**Total diluting solvent (ml)**	**FC770 (ml)**	**FC70 (ml)**	**FC70 volume fraction**	**Ink viscosity (mPa·s)**
1	3	2	2	0	0	36.8
2	3	2	1	1	0.2	71.7
3	3	2	0	2	0.4	140.3

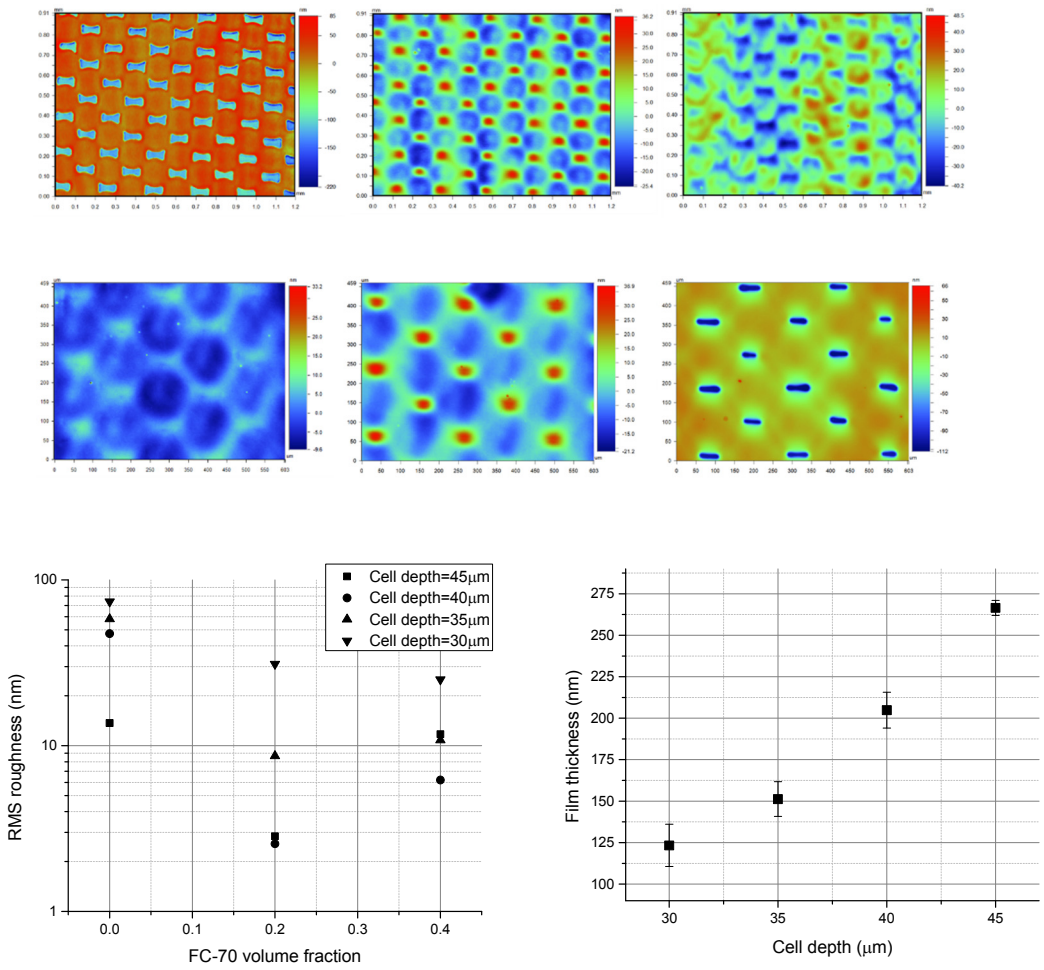

Figure 6.10 (a) Optical interferometric images of dielectric films showing film roughness caused by different ink compositions printed from the same 35-μm cell depth. The FC-70 volume fractions are 0, 0.2, and 0.4 from left to the right. (b) Optical interferometric images showing the effects of cell depth on film uniformity using ink with FC-70 fraction of 0.2. The cell depths were 40, 35 and 30 μm from the left to right. (c) surface roughness as a function of FC-70 volume fraction and cell depth. (d) film thickness controlled by varying cell depth.

Then, gate electrodes are printed and coarsely aligned by using ink jet printing. Because the required pattern resolution and alignment accuracy is low, this step is non-critical, and any fast, relatively low-resolution printing technique can be used. The device characteristics are showed in Figure 6.11 with channel lengths of 5.4, 4.5 and 2.7 μm; these represent record in device scaling of fully printed devices. Saturation and linear mobilities are smaller than spin-coated devices, which can be caused by aggressive channel scaling and lower semiconductor quality due to the use of printing processes. This also results in degraded subthreshold swing. The statistically extracted device parameters are showed in Figure 6.12. Mobility increases with smaller channel length similar to work reported by Fukuda [23]. Finally, we characterized AC performance in a common-source configuration using an external resistor. By measuring the

output signal as function of frequency, we extracted the transition frequency of fully printed transistors as shown in Table 6.3. The transition frequency is above 1 MHz in case of the shortest channel length, which is an excellent result for organic transistors in general and for printed organic transistors in particular.

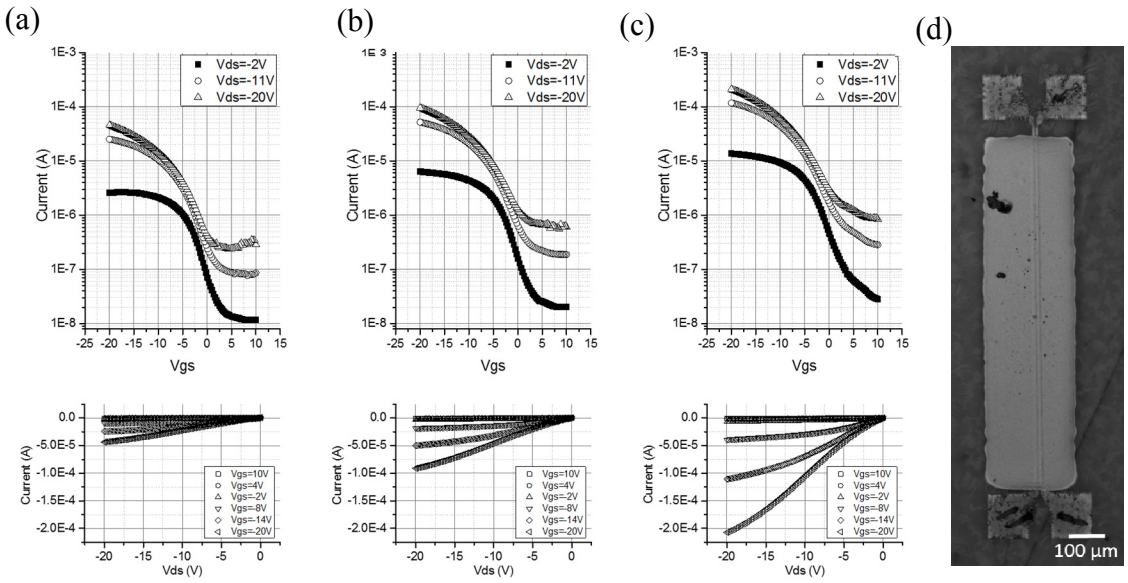

Figure 6.11 (a-c) Transfer and output characteristics of fully printed TFTs. The channel lengths are 5.4, 4.5, and 2.7 µm, printed from 6, 5, 3-µm cells, and W=963 µm. (d) optical image of a fully printed TFT.

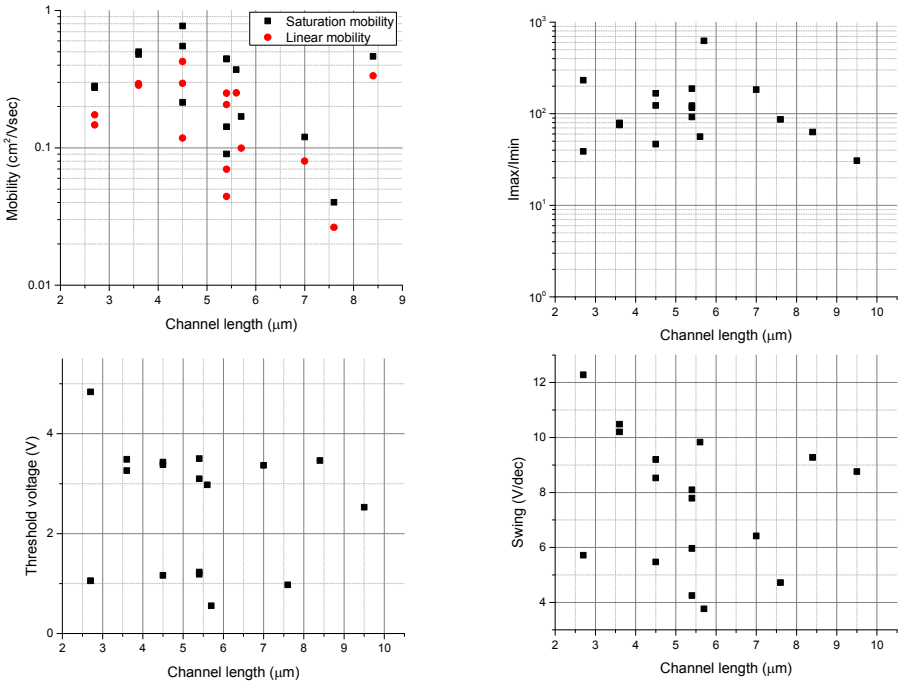

Figure 6.12 Extracted devices parameters, mobilities, a ratio of maximum to minimum currents, threshold voltages and subthreshold swing, of fully printed TFTs as a function of printed channel length.

Table 6.3 Extracted parameters for transition frequency

Cell width (μm)	Printed line width (μm)	Channel length (μm)	Saturation mobility ($cm^2/V \cdot s$)	fT (MHz)	g_{m_max} (μS)	C_{gd} (pF)	C_{in} (pF) $=C_{gs}+0.67\times C_{ch}$
3	3.9	2.7	0.197	1.920	11.21	0.38	0.56
4	5.2	3.6	0.165	0.950	7.52	0.51	0.75
5	6.5	4.5	0.170	0.678	6.13	0.64	0.82

6.5 Conclusions

We are able to substantially push the limits of printed organic transistors by using a fully overlapped top-gate architecture, in which the critical feature size is the source/drain spacing. By using fine-line source and drain electrodes and fully overlapped gates, we make the structure entirely tolerant of misalignment without significantly impacting overlap capacitance and switching performance. Source/drain electrodes were printed by an inverse direct gravure using fine silver nanoparticle ink, delivering highly conductive lines as fine as 2.38 μm at a high printing speed of 0.6 m/s. The printed lines delivered a sheet resistance as low as 3.35 Ω/□. This aggressive scaling was achieved by exploiting the substantial understanding of the underlying physics of gravue printing that we have achieved in recent years [14], [15]. Then, semiconductor and dielectric layers were printed by a sheet-fed direct gravure printer. We formulate a new ink composition to gain ultra uniform dielectric films using gravure printing at a speed of 0.5 m/s. Finally, gate electrodes were printed in a fully-overlapped manner using a low-resolution inkjet printer; despite the use of low-resolution gates, high-performance is still achievable, since both the channel length and overlap capacitance are determined solely by the high-resolution gravure printed source/ drain layer. The devices showed good DC characteristics and delivered transition frequencies as high as 1.92 MHz. This is among the highest performance fully printed devices reported in the literature, and attest to the promise of the technology herein.

6.6 References

[1] H. Sirringhaus, T. Kawase, R. H. Friend, T. Shimoda, M. Inbasekaran, W. Wu, and E. P. Woo, "High-Resolution Inkjet Printing of All-Polymer Transistor Circuits," *Science (80-.).*, vol. 290, no. 5499, pp. 2123–2126, Dec. 2000.

[2] Y.-Y. Noh, N. Zhao, M. Caironi, and H. Sirringhaus, "Downscaling of self-aligned, all-printed polymer thin-film transistors," *Nat Nano*, vol. 2, no. 12, pp. 784–789, Dec. 2007.

[3] P. F. Moonen, B. Vratzov, W. T. T. Smaal, G. H. Gelinck, M. Péter, E. R. Meinders, and J. Huskens, "A common gate thin film transistor on poly(ethylene naphthalate) foil using step-and-flash imprint lithography," *Org. Electron.*, vol. 12, no. 12, pp. 2207–2214, Dec. 2011.

[4] J.-M. Verilhac, M. Benwadih, A.-L. Seiler, S. Jacob, C. Bory, J. Bablet, M. Heitzman, J. Tallal, L. Barbut, P. Frère, G. Sicard, R. Gwoziecki, I. Chartier, R. Coppard, and C. Serbutoviez, "Step toward robust and reliable amorphous polymer field-effect transistors and logic functions made by the use of roll to roll compatible printing processes," *Org. Electron.*, vol. 11, no. 3, pp. 456–462, Mar. 2010.

[5] A. de la Fuente Vornbrock, D. Sung, H. Kang, R. Kitsomboonloha, and V. Subramanian, "Fully gravure and ink-jet printed high speed pBTTT organic thin film transistors," *Org. Electron.*, vol. 11, no. 12, pp. 2037–2044, Dec. 2010.

[6] H. Kang, R. Kitsomboonloha, J. Jang, and V. Subramanian, "High-performance printed transistors realized using femtoliter gravure-printed sub-10 μm metallic nanoparticle patterns and highly uniform polymer dielectric and semiconductor layers.," *Adv. Mater.*, vol. 24, no. 22, pp. 3065–9, Jun. 2012.

[7] D. Khim, H. Han, K.-J. Baeg, J. Kim, S.-W. Kwak, D.-Y. Kim, and Y.-Y. Noh, "Simple Bar-Coating Process for Large-Area, High-Performance Organic Field-Effect Transistors and Ambipolar Complementary Integrated Circuits.," *Adv. Mater.*, pp. 1–7, Apr. 2013.

[8] M. M. Voigt, A. Guite, D. Chung, R. U. A. Khan, A. J. Campbell, D. D. C. Bradley, F. Meng, J. H. G. Steinke, S. Tierney, I. McCulloch, H. Penxten, L. Lutsen, O. Douheret, J. Manca, U. Brokmann, K. Sönnichsen, D. Hülsenberg, W. Bock, C. Barron, N. Blanckaert, S. Springer, J. Grupp, and A. Mosley, "Polymer Field Effect Transistors Fabricated by the Sequential Gravure Printing of Polythiophene, Two Insulator Layers, and a Metal Ink Gate," *Adv. Funct. Mater.*, vol. 20, no. 2, pp. 239–246, Jan. 2010.

[9] T. Sekitani, Y. Noguchi, U. Zschieschang, H. Klauk, and T. Someya, "Organic transistors manufactured using inkjet technology with subfemtoliter accuracy.," *Proc. Natl. Acad. Sci. U. S. A.*, vol. 105, no. 13, pp. 4976–80, Apr. 2008.

[10] M. T. Demko, J. C. Cheng, and A. P. Pisano, "High-resolution direct patterning of gold nanoparticles by the microfluidic molding process.," *Langmuir*, vol. 26, no. 22, pp. 16710–4, Nov. 2010.

[11] H.-Y. Tseng, B. Purushothaman, J. Anthony, and V. Subramanian, "High-speed organic transistors fabricated using a novel hybrid-printing technique," *Org. Electron.*, vol. 12, no. 7, pp. 1120–1125, Jul. 2011.

[12] J. Rogers and R. Nuzzo, "Recent progress in soft lithography," *Mater. today*, no. February, pp. 50–56, 2005.

[13] Y. Xia and G. M. Whitesides, “SOFT LITHOGRAPHY,” *Annu. Rev. Mater. Sci.*, vol. 28, no. 1, pp. 153–184, Aug. 1998.

[14] R. Kitsomboonloha, S. J. S. Morris, X. Rong, and V. Subramanian, “Femtoliter-scale patterning by high-speed, highly scaled inverse gravure printing.,” *Langmuir*, vol. 28, no. 48, pp. 16711–23, Dec. 2012.

[15] R. Kitsomboonloha and V. Subramanian, “Lubrication-related residue as a fundamental process scaling limit to gravure printed electronics.,” *Langmuir*, vol. 30, no. 12, pp. 3612–24, Apr. 2014.

[16] N. J. Wagner and J. F. Brady, “Shear thickening in colloidal dispersions,” *Phys. Today*, vol. 62, no. 10, p. 27, 2009.

[17] T. Sekine, H. Ikeda, A. Kosakai, K. Fukuda, D. Kumaki, and S. Tokito, “Improvement of mechanical durability on organic TFT with printed electrodes prepared from nanoparticle ink,” *Appl. Surf. Sci.*, vol. 294, pp. 20–23, Mar. 2014.

[18] D. Soltman and V. Subramanian, “Inkjet-printed line morphologies and temperature control of the coffee ring effect.,” *Langmuir*, vol. 24, no. 5, pp. 2224–31, Mar. 2008.

[19] A. Darhuber, S. Troian, and S. Miller, “Morphology of liquid microstructures on chemically patterned surfaces,” *J. Appl.*, vol. 87, no. 11, p. 7768, 2000.

[20] V. Constantoudis, E. Gogolides, J. Roberts, and J. K. Stowers, “Characterization and Modeling of Line Width Roughness (LWR),” 2005, vol. 5752, pp. 1227–1236.

[21] Y. Fujisaki, H. Ito, Y. Nakajima, M. Nakata, H. Tsuji, T. Yamamoto, H. Furue, T. Kurita, and N. Shimidzu, “Direct patterning of solution-processed organic thin-film transistor by selective control of solution wettability of polymer gate dielectric,” *Appl. Phys. Lett.*, vol. 102, no. 15, p. 153305, 2013.

[22] M. H. Eres, D. E. Weidner, and L. W. Schwartz, “Three-Dimensional Direct Numerical Simulation of Surface-Tension-Gradient Effects on the Leveling of an Evaporating Multicomponent Fluid,” vol. 35, no. 24, pp. 1859–1871, 1999.

[23] K. Fukuda, Y. Takeda, M. Mizukami, D. Kumaki, and S. Tokito, “Fully solution-processed flexible organic thin film transistor arrays with high mobility and exceptional uniformity.,” *Sci. Rep.*, vol. 4, no. 20 V, p. 3947, Jan. 2014.

Chapter 7 Conclusions and Future Work

7.1 Conclusions

This thesis contributes to the modeling and technological development of high-resolution, high-speed gravure printing. The simple model proposed herein states that the physics of gravure printing can be understood by separately studying each stage of gravure printing and then linking results with respect to the capillary number to create a comprehensive model. These stages are filling, wiping, transferring and spreading. The first intriguing mechanism revealed was the drag-out effect that is related to the wettability of ink on the printer components and substrate, to the geometry of the printer components, and the capillary number. The drag-out process causes a residue behind defined patterns, which broadens and merges patterns along the printing direction. To achieve the best printing resolution, this residue must be eliminated.

The second fundamental process is the lubrication between the doctor blade and the roll surface, which causes uniform residues on non-patterned areas. We offer insight into the physical mechanisms underlying this lubrication by quantifying the lubrication film and providing dimensional analysis to postulate the lubrication regime in gravure printing. These nanometric lubrication films were statistically measured using spatially calibrated reflectometry. The results reveal that, at high viscosity and high speed, gravure wiping operates in a manner consistent with the elastohydrodynamic lubrication regime. By reducing the product of viscosity and printing speed, the EHD lubrication transitions to micro-EHD and finally into the mixed lubrication regime. The thickness of the lubrication film in mixed lubrication is governed by the boundary film, setting a fundamental limit on residue reduction in gravure printing. By understanding both drag-out and lubrication processes, guidelines for operating a gravure printer are suggested to minimize overall residues.

Third, the filling process was studied via novel experiments and simulations. The results suggest that the filling process strongly depends on the capillary number and the filling process of different cell sizes are similar when compared at the same dimensionless time. Complete filling can be expected when the capillary number is below 0.1; higher capillary numbers produce successively worse filling, with complete air entrapment ultimately occurring at high capillary numbers. The filling failures are caused by contact line pinning at the cell edges and interface deformation over the cell opening. This limits the maximum speed of gravure printing.

Building from this understanding, the realization of optimized line width and spacing as small as 2 μm was demonstrated by using a high-resolution, high-speed inverse direct gravure printer. The fine printed features attest to the advantages of high-resolution, high-speed gravure printing as follow; 1) compatibility with high viscosity inks, 2) high throughput, and 3) high resolution and pattern fidelity. These truly satisfy the goals of this thesis to advance pattern printing technologies toward high-resolution, high-speed patterning on flexible substrates, which is a critical milestone for printed electronics.

Furthermore, an engraving technology based on modern microfabrication is proposed to overcome limitations of current technologies in terms of the smallest features, surface finishing,

and cell arrangements. Various cell opening shapes and profiles were investigated to find a suitable cell geometry for high-resolution, high-speed gravure printing. The results suggest that a cell geometry of square opening with inverse-pyramid profile is the best, because it has a symmetric shape, maintains printing performance as cell size is scaled down and is suitable for composing electronic patterns, confirming physical understanding built from earlier chapters. In addition, this best cell geometry can be fabricated by simple lithography and anisotropic wet etching, which gives a further advantage of this fabrication process. Then, a high-resolution roll, a magnetic roll with a thin metal sheet carrying the patterns, was fabricated as follows. The metal sheet was a replicate of optimized silicon printing plates produced by polymer molding and electroplating processes. By using this roll, features below 10 μm can be printed.

Finally, we demonstrate a process to realize high-performance, high-resolution, high-speed gravure printed organic thin film transistors. The process exploits high resolution S/D electrodes printed using highly-scaled gravure printing to realize a device architecture that offers high switching speeds due to low overlap capacitance and aggressive channel length scaling while simultaneously offering good misalignment tolerance. Using this process, we demonstrated fully-printed TFTs, printed at speeds of ~0.5 m/s, with channel lengths as small as 2.7 μm, leading to a transition frequency above 1 MHz. The fabrication process is suitable for mass production, since it requires low alignment accuracy and can produce high-performance thin-film transistors at very high throughput.

7.2 Future work

Although the mechanisms of gravure printing are now fairly well-understood, high-resolution, high-speed gravure printing is still an interesting research topic, of which further studies are needed to completely understand and exploit the potential of this printing technique. Several directions should take place as the next steps.

First of all, printed volume must be increased, which in turn increases printed film thicknesses and allows further line width scaling down below submicron regimes. Because the printed volume depends on filling, wiping and transferring, the effectiveness of each process must be increased. For the filling process, the main concern is how to improve filling at high capillary number, i.e. high speed, because of weak dependency on the cell size. There are several possible solutions as proposed in Chapter 4, which need experimental validation. Mainly, a shallow cell geometry with fillet edges should be used and/or an appropriate shear rate should be introduced to completely remove entrapped air. The shear rate can be imposed easily by bring a solid surface close to roll surface near the contact line where the filling process happens. These exemplify important strategies to enhance the filling process for high speed printing. Wiping of submicron cells is a real challenge. Coating robust non-wetting films such as grafted polymer, ceramic coating, etc. on both blade and roll surfaces could alleviate these problems, because these non-wetting coatings can suppress both capillary flows of the drag-out process and boundary films of the lubrication process. Therefore, exploring such coatings for gravure printing will be important topics to further reduce overall residues. The non-wetting roll surface may also favor the transfer process, allowing ink to easily flow out of the cells. However, a non-

wetting roll surface is not preferred for the filling process, in which the wettability of cell wall is required for capillary filling. Therefore, a heterogeneous roll surface that has wetting cell walls and non-wetting areas on non-patterned area is a promising solution. In addition to static wetting, an incorporation of dynamic wetting, like electrowetting, could overcome these optimization challenges. An electrostatic force is already used in modern gravure printing in transferring process, but never used in other phases of gravure printing. By incorporating dynamic wetting in the filling and wiping processes, each process can be individually, electrically enhanced. This gives added flexibility in terms of process control and can decouple printing parameters such as printing speed, from the optimization of ink properties. For instance, instead of using a non-wetting coating on the doctor blade, an electrostatic force could repel ink at the outlet during wiping, leading to a perfect ink retention. Moreover, experimental studies on the transfer process are necessary to build a more comprehensive model of gravure printing. These studies include transferring ink to variable topography in which film thickness and wettability are non-uniform, since this process is essential for fabricating electronic devices and circuits. Finally, sperading must be precisely controlled to produce fine lines with small line-edge-roughness. Spreading control can be done by developing a substrate with a large contact hysteresis, but a smooth surface. This suggests that chemically heterogeneous surfaces with nanodomains like block-copolymers would be an interesting substrate for high-resolution printing.

Second, the development of diverse functional inks for gravure printing should be pursued. Currently available inks for gravure are very limited to organic and nanoparticle inks. Inorganic inks, including sol-gel and nanoparticles can open up more applications of gravure printing. By using a simple model developed here, one can specify requirements for gravure inks, such as viscosity, surface tension, mass loading, and so on. For example, submicron printing will require extremely high mass loading (>75wt%) in order to deposit useful materials, if the printed volume cannot be increased. In addition, the effects of ink rheology like shear thinning and yield stress on printing quality and pattern formation should be studied as well.

Third, an extension of single-cell modeling to pattern formation should be developed. This is another step toward using gravure printing in real applications for which complex geometries are indispensable. To simplify the modeling, hierarchical modeling and library approaches are promising. These methods would allow models to include relevant effects of cell geometry and cell density, ink properties, printing conditions and substrate wettability in each hierarchical level and to quickly predict printed shapes without exhaustive computation. These models are very useful for gravure printing, because master patterns cannot be altered and it is time consuming and expensive to experimentally test designed patterns. Standardized cell libraries for circuits are also important for a rapid circuit design as well.

Lastly, high-resolution, high-speed gravure printers and rolls should be implemented. The design of printers should be guided by the physical understanding achieved in this thesis. For example, a closed-loop blade pressure system can be implemented by using friction force between blade and roll surface as a feedback signal. By doing so, minimized lubrication residue can be automatically obtained. Alignment accuracy must also be improved to make printers valuable for fabricating electronic system. A high-resolution roll fabrication based on modern

microfabrication was demonstrated, but it does not include a hard layer. This limits the roll usage to a short printing run, which is suitable for research purposes only. In order to make this printing technique industrially viable, the roll robustness must be improved by adding a hard layer and/or reducing wearing through lubrication.

In summary, these future research directions could further improve all aspects of high-resolution, high-speed gravure printing for printed electronics, such as improving overall understanding of printing mechanisms, developing advanced electronic inks and substrates, and implementing high-resolution printers. These in turn open up the full potential of gravure printing for printed electronics, which can benefit our societies as media printing did in the past.